POLITECNICO DI TORINO

**Corso di Laurea Magistrale**
**in Ingegneria Meccatronica**

Tesi di Laurea Magistrale

# Attitude control strategies for small satellite observation of a collaborative target


**Relatore**
prof. Fabrizio Stesina

**Candidato**
Filippo Grimaldi


Anno Accademico 2021-2022

# Abstract

In recent years in-space devices are rapidly increasing in number and variety because of technological advancements. Nowadays CubeSats are the foundation of this new concept where tiny dimensions are necessary to produce more effective structures, leading to cheaper prices and simpler designs. This small system's attitude and orbit are affected by several unknown factors (external environmental disturbances, modeling mistakes, and design flaws) where the smaller the satellites, the more influence they are, making space an unfriendly environment for a small satellite. Since this thesis devises a method to carry out the close-range observation of a collaborative target with a CubeSat flying a helix trajectory, attitude control is essential for orienting the Cubesat during the operation. Since the satellite must follow strict angular orientation and actuation restrictions, it is vital to provide strong control performance while using minimal inputs. The aim of this work is first to formulate a tracking control problem enabling the observer CubeSat to perform the observation, choose a proper control solution, and build a model to test the solution and evaluate the performance.

To determine whether the design meets the requirements and then evaluate the solution performance, numerical simulations are carried out using MATLAB and Simulink. This study stresses the quality of the control solution in terms of performance and efficiency during simulations of realistic scenarios, with an emphasis on the robustness of the controllers.

The first part of this work is dedicated to the development of a proper method to enable the observer CubeSat to conduct the close observation, focusing on the design of a suited time-variant reference attitude for the tracking control problem, the design of the multibody dynamics model of the satellite and the choice of the satellite attitude control law.

In the second part, the performance of the attitude control solution is tested to show that it can accomplish the task while rejecting the environmental disturbances and the model uncertainties.

# Ringraziamenti

Lorem ipsum dolor sit amet, consectetur adipiscing elit, sed do eiusmod tempor incididunt ut labore et dolore magna aliqua. Ut enim ad minim veniam, quis nostrud exercitation ullamco laboris nisi ut aliquip ex ea commodo consequat. Duis aute irure dolor in reprehenderit in voluptate velit esse cillum dolore eu fugiat nulla pariatur. Excepteur sint occaecat cupidatat non proident, sunt in culpa qui officia deserunt mollit anim id est laborum.

Index

# 1. Introduction

The challenge of establishing an active satellite's relative attitude concerning a target space object is known as spacecraft attitude determination. Various mission scenarios, like on-orbit operation, debris clearance, and autonomous asteroid reconnaissance, need the ability to assess the attitude of the active spacecraft. The need for autonomy in this kind of operation results from the impracticality of ground control-based navigation therefore attitude determination is a procedure that necessitates algorithm customization based on the operating conditions and the cooperative target.

A quick summary of small satellite technology advancement is done before entering deeper details on the application since the observer satellite proposed in this work is a CubeSat.

Going back to the 1960s, when satellites were all very small spacecraft, can help to understand where this branch of technology came from. These early satellites generally had masses of only a few kilos and modest volumes. This was because these satellites had low expectations, were mostly experimental, and were restricted by launch vehicle capacity. However, in the years that followed, the design changed rather quickly. Satellites grew in size and complexity with each new generation. This trend was driven by the main use of satellites at the time: communication. Since the 1960s, communication has been the main practical application for satellites. Larger and heavier satellites were developed as a result of the requirement for global long-distance communication and the growing cost-effectiveness of every new generation of satellites. During these first decades of evolution, artificial satellites became one of the most valuable pieces of advanced technology in the world. Satellite advancement has changed many aspects of day-to-day life, as can be seen in the fields of communication, navigation, observation, weather forecasting, and space exploration. This evolution is a continuous process that, in the last decades, has undertaken a different path in the way satellites are operated and manufactured. The development of the CubeSat standard has accelerated this new trend, resulting in a rapid proliferation of tiny spacecraft weighing only a few kilos. Initially intended mainly for educational purposes, these satellites potential value in technological demonstrations and operational missions was recognized over the years, and the CubeSat market rapidly increased. The goal of the CubeSat standard was to reduce the weight, cost, and time associated with its digital components by utilizing smaller digital equipment [24].

If one looks at the total number of satellites operating in the last decade, their amount is rapidly increasing over time. There were less than 50 satellites below 600 kg deployed in 2011, while in 2020 they were more than 1200 [1]. This industry is growing since the miniaturization of satellites and launchers has encouraged many commercial projects, characterized by high technological added value,

to use this class of satellites. The low cost of operation and flexibility make CubeSats a highly viable technology for validation, observation, and space exploration. As a result, small satellites can now be used to solve tasks that were previously thought to demand expensive large satellites that take months or even years to design, manufacture, and test. So, small satellites must be seen as a possible option for many different situations.

The restriction resulting from the necessity of occupying a limited space on the launch vehicle is the most evident effect of the CubeSat Standard. This limitation is always considered when establishing if a mission can be realized with a CubeSat [26]. In general, small satellites are used in any space application where their features are convenient for the mission aim and the mission requirements do not conflict with the small satellites' physical constraints. But CubeSats are not just an alternative solution for already existing satellite applications, they also find applications in a broad array of novel implementations which exploit the properties of this class of satellite. Some relevant implementations that had shown this technology's potential over the last twenty years are:

- The first operational satellite for Malaysia TiungSat-1 debuted in the year 2000, including both operational components and features for technological demonstration. This satellite made it possible for a group of Malaysian space engineers to handle the satellite for Earth observation and space research missions [28].
- The ALSAT-2 mission was planned with data collection and Earth observation as goals. High-quality images were collected thanks to the ALSAT-2 for several tasks, such as land organization, mapping, managing precious natural resources, agriculture, and controlling natural disasters. In addition, this satellite was among the first to enter the Disaster Monitoring Constellation [28].
- The Nigeria Space Research & Development Agency developed NigeriaSat-1, a 100 kg experimental minisat. It supplied photos with broad coverage across a 600-kilometer route, enabling a regular worldwide update. It has the unique capacity to provide an indicator called a Normalized Differential Vegetative Index (NDVI). This function made it feasible to quickly inform people of potential environmental problems. The Katrina hurricane devastation in New Orleans was captured in the first Earth observation satellite photos using this satellite's capability [28].
- Beijing-1 was an earth observation satellite with two cameras, one has a much higher resolution imaging capability while the other camera had a lower resolution to track a wider path. Beijing-1 was able to deliver quick updates on problems affecting China, such as water supplies, agricultural output, patterns of urban expansion, environmental pollution, and disaster

monitoring across the country. Additionally, new digital maps of China as a whole and accurate maps of cities and metropolitan regions were produced using this new tool [28].

- KazEOSat-2 was born from the collaboration of the Kazakhstan government with Surrey Space Technology limited. Resource management, monitoring of agriculture, and mapping are all accomplished with KazEOSAT-2 medium-resolution images [28].
- Formosat-7 is a cooperative program with Taiwan and SSTL where six satellite platforms are used to monitor the ionosphere and weather, as well as to collect data for climate change studies [28].
- The Artemis I mission's secondary payload, NEA Scout, will become the first CubeSat to investigate an asteroid in late 2022. As part of the Artemis program, NEA Scout will carry out a variety of research activities and technological demonstrations in deep space [2].

This study aims to demonstrate CubeSat's capability to perform novel applications enabled by these small spacecraft features. The goal is to design an attitude control system for a small satellite in an innovative implementation: the inspection of a collaborative target spacecraft carried out by a CubeSat while performing a circular helix trajectory with the target at its center. The goal is to constantly frame the target with the optical sensors placed on the CubeSat, which is flying around the target spacecraft. The method to perform the observation is also defined in the research as a requirement for the activity. This kind of application has some comparable automated proximity operations with CubeSat, as the one launched from the International Space Station or as [31], but since there are relevant dissimilarities in the settings, this work outlines a generalized procedure where the observer satellite is able to successfully complete the task by generating a suitable attitude trajectory to use as a reference in a tracking control problem.

Concerning the application treated in this study, attitude control is an essential component in many space applications, inaccurate attitude control or kinematic model can lead to excessive fuel consumption, a higher risk of components failure, and the inability to carry out complex maneuvers, factors that may entail failing the mission. Hence, the procedure to find the attitude control solution must consider the main difficulties of the application, to best meet the requirements imposed by the problem. The tracking control difficulties of this implementation are:

- Complex time-variant attitude maneuver.
- External and internal disturbances.
- Small satellite size, which entails:
    - Larger error sensibility.

- Smaller control input and capacity.

It may go unnoticed, but since the reference to fallow is fast changing over time, the control solution may present unwanted behaviors, as highlighted in [18]. Moreover, the observer satellite's small size entails both a small sub-optimal actuator system and higher sensibility to disturbances, in a setting characterized by uncertainties and environmental disturbances.

If the list above is not enough, the system to control is also nonlinear, which means stability does not guarantee the capability to withstand bounded disturbances, this capability must be specifically dealt with using a suited control strategy. To address the capability of a nonlinear system to withstand persistent bounded disturbances the notion of robustness is used, but before proceeding it is important to delineate properties taken into consideration when selecting a control strategy for a nonlinear system.

The performance that a control system must achieve may be generally described quantitatively in linear control problems. On the other hand, specifications for nonlinear systems are considerably more challenging since a nonlinear system's reaction to one command does not always foretell its response to another. As a result, in the case of nonlinear systems, qualitative definitions of the expected behavior in the operational region of interest are usually pursued.

The following characteristics, which can be found in [15], are considered when deciding the behavior of nonlinear control systems:

- The *stability* of the nominal model must be assured. Additionally, also the area of stability and convergence are also of concern.
- *Accuracy* and speed of response may be considered. For some systems, a proper controller design may provide consistent tracking accuracy regardless of the desired trajectory.
- *Robustness* is the susceptibility to the effects ignored in the design of the nominal model, such as disturbances, noise, unmodeled dynamics, etc. When carrying out the desired tasks, the system needs to be able to endure these neglected effects.

The attributes listed above conflict with one another, and a successful control system can only be acquired through an effective trade-off. In the proposed application both stability and robustness are essential requirements since the CubeSat is constantly under disturbances, while it is not vital to have the best possible accuracy. On this basis, a robust control strategy is well suited for this application's features.

When designing a robust nonlinear controller, the theoretical model and some characterizations of the model uncertainties are considered. Robust nonlinear control techniques successfully solve various

practical control problems as [16] and [17]. These methods often require state measurements and work best with nonlinear systems.

The robust strategy used for this attitude control problem is the so-called sliding mode control methodology, a popular robust approach that has gained recognition in recent years due to its ease of use and broad application in various engineering systems. It is based on the observation that first-order systems, whether nonlinear or uncertain, are significantly simpler to regulate than a conventional higher-order system. Sliding controller design offers a methodical solution to preserve stability and good performance in the face of modeling errors. The drawback that this class of controller may present is the chattering phenomenon, which was one of the main obstacles to its first implementations. Nowadays there are several efficient techniques devised for chattering suppression, allowing the implementation of sliding mode controllers for a wide set of systems.

Literature is full of studies exploiting the SMC features. As treated in the applications of [3] and [4] a first-order SMC achieves a finite time convergence, guaranteeing good transient performance and globally uniformly bounded stability under significant disturbances. Sliding mode controllers also guarantee finite convergence when the reference is rapidly changing over time, as shown in [18] with a first-order sliding mode and in the work of Farbod Fahimi [5], with a high-order sliding mode controller applied to a Vision-Based CubeSat. If the sliding mode order is higher than the system's relative degree, it can guarantee good performances, better than the first-order implementation, while considerably decreasing the chattering phenomena as explicated in [6]. u

The main benefit of sliding mode control is the insensitivity of the closed-loop response to bounded uncertainties [7] as model parameter uncertainties, disturbances, and non-linearities. In essence, SMC simplifies the control of nonlinear systems under uncertainty-based scenery guaranteeing good overall performance and stability. This satisfying performance is achieved in the presence of arbitrary parameter uncertainty at the cost of higher control activities. This is usually in conflict with the model's sources of uncertainty, such as neglected dynamics, which the intense control action may excite. Consequently, the control law is tuned with the objective to attain an effective trade-off between tracking performance and parametric uncertainty robustness while guarantying stability.

The control system is assessed after being designed. There is no standard technique for analyzing nonlinear control systems in the same way as linear control systems because the direct solution of nonlinear differential equations is often unachievable and frequency domain transformations cannot be used. In this context, computer simulation is a crucial analytical technique to analyze the qualitative nature of the requirements. The simulations' objective is to investigate the behavior of the controlled system to check if the solution complies with the problem's specifications. Nevertheless, the simulation of nonlinear systems without any theoretical consideration, is likely to produce deceiving

results since nonlinear systems can display different behaviors with nearly the same initial conditions. In this work, the purpose of simulations is first to tune the chosen control law to meet the requirements through a trial-and-error procedure, while optimizing the performance. Once the control solution is ready a first worst-case set of simulations is performed to evaluate the control solution's robustness to the expected uncertainties. Then an analysis of the system's performance and robustness based on the Monte Carlo method is implemented by stochastic simulation and statistical test of uncertain variables. The Monte Carlo analysis is frequently used to study a given system's robustness in the presence of disturbance, as it was done in the following examples: in [19] a Monte Carlo analysis was used to investigate the robustness of a nonlinear control system for UAVs formations, in [20] the analysis was done to determine the sensitivity to uncertainty in the aerodynamic parameters of a missile's autopilot. In [21] a Monte Carlo simulation is used to examine the robustness of drag-modulation flight-control systems to expected flight uncertainty while in [22] is used to show the better performance of a sliding mode controller, also in terms of robustness, with the already existing integrated control of a missile. As suggested by these examples, the Monte Carlo approach can be adopted to evaluate the performance of nonlinear systems, making it easier to evaluate the impact of risk under uncertain initial conditions. The drawback of this method is the need for many simulations to properly investigate the parameter space of the problem.

The work is divided into 5 parts:

- Chapter 2 gives an overview of the problem settings before going to define a generalized method to accomplish the inspection of the collaborative target, imposing a suitable reference attitude trajectory to the observer satellite.
- In Chapter 3 the kinematics is investigated using quaternions to avoid the singularity problem that might arise with Euler angles, but the satellite dynamics is addressed using Euler's equation of motion. Additionally, a more realistic model is devised by adding external disturbances and taking into account the restrictions imposed by a commonly used actuation system.
- In Chapter 4 the designed sliding mode controller is tuned through a trial-and-error procedure using the models devised in the previous chapter while checking if the solution respects the performance requirements.
- In Chapter 5 the control solution performance is thoroughly examined in several scenarios. The outcomes are displayed and explained.
- In Chapter 6 conclusion and future work are discussed.

# 2. Problem description

This chapter outlines the procedure employed to establish the problem's setting and a generalized method to carry out the collaborative observation.

The inspection of a collaborative target is carried out by a CubeSat flying a circular helix trajectory with a constant pitch and radius. A 12U CubeSat platform is the observer, meanwhile, the collaborative target is a bigger spacecraft. The collaborative spacecraft has its center of mass located on the mid-point of the helix trajectory centerline as illustrated in *Figure 4*.

Assuming that the optical sensors used for the observation are aligned with the satellite's z-axis, it is necessary to derive a suitable attitude trajectory to keep the z-axis pointing toward the spacecraft (ideally the spacecraft center of mass) while performing the helix trajectory. This trajectory is used as a reference in this control problem enabling the observer satellite to adequately conduct the operation. When designing this attitude maneuver the satellite position in the helix trajectory, the reference frame and the collaborative target position must be considered to correctly describe the sequence of attitudes that the satellite must pass through to execute the observation. All the theoretical steps used to derive the reference attitude are illustrated in this chapter after a theoretical introduction to the problem settings.

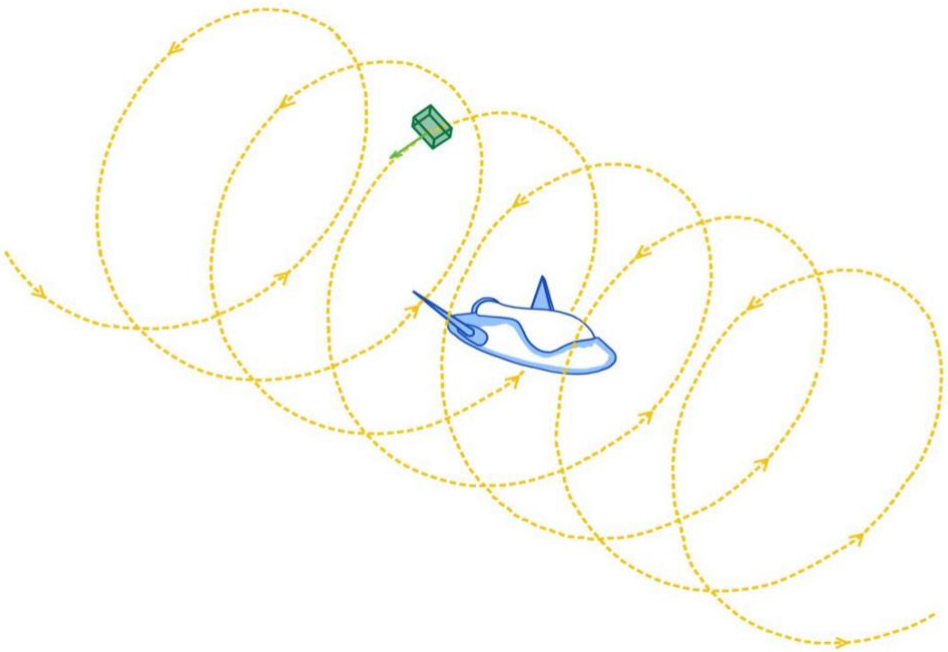

*Figure 1: Not in scale representation of the helix trajectory, the Target Spacecraft (in blue) and the Satellite (in green). The green vector states the satellite's linear velocity.*

## 2.1 Satellite classification

As anticipated in the introduction, the advance in the field of micro-controllers, micro-propulsions, and communication systems have pushed the development of the "Small Satellite". SmallSats are satellites with modest mass and dimensions, commonly weighing under 1200 kg. Inside the SmallSat category, there are several subcategories. The CubeSat 12U used in this study falls in the microsatellite subcategory since its weight is around 20 kg, as exemplified in *Figure 2*. Also considering the shape, our satellite falls in the CubeSat family; "The original CubeSat Design was developed at California Polytechnic State University in San Luis Obispo starting in 1999" [23]. To make it simpler for institutions to access space, the CubeSat standard was created. Today, the standard is recognized by many organizations all around the world. It defines the outer dimensions of the satellite with multiple cubic units of 10x10x10 cm, a CubeSat can be used alone (1 unit) or in groups of multiple units

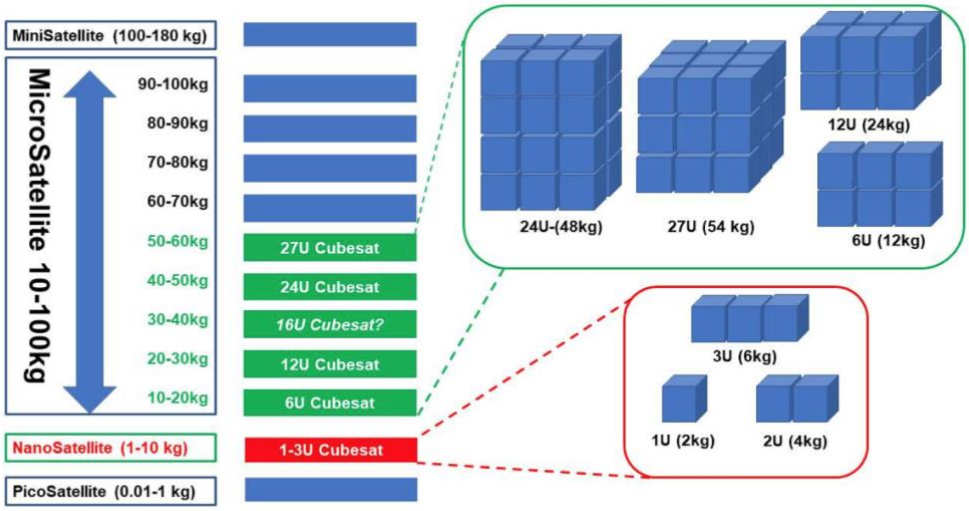


*Figure 2: Microsatellite and nanosatellite size comparison to CubeSat containerized sizes [30]*

## 2.2 Reference frames

Mobile objects are normally tracked from an external frame used to evaluate rigid body dynamics and kinematics. The external reference frame is necessary to obtain the equations of a spacecraft's motion, and the equations of motion are essential in spacecraft attitude control. The attitude reference frame is at the heart of attitude representation, which is defined as a set of coordinates that describe the orientation of a rigid body reference with respect to a second external fixed reference frame.

Converting between the body frame and the fixed reference frame is how the spacecraft's attitude is manipulated. For different purposes, distinct reference frames are employed.

In this work, the *LVLH frame* of the almost inertial *collaborative target spacecraft* is used to describe the *observer satellite*'s *Body Frame* orientation. The target reference frame is almost inertial since the spacecraft has negligible accelerations. For simplicity, this frame is considered inertial and is used as the fixed frame.

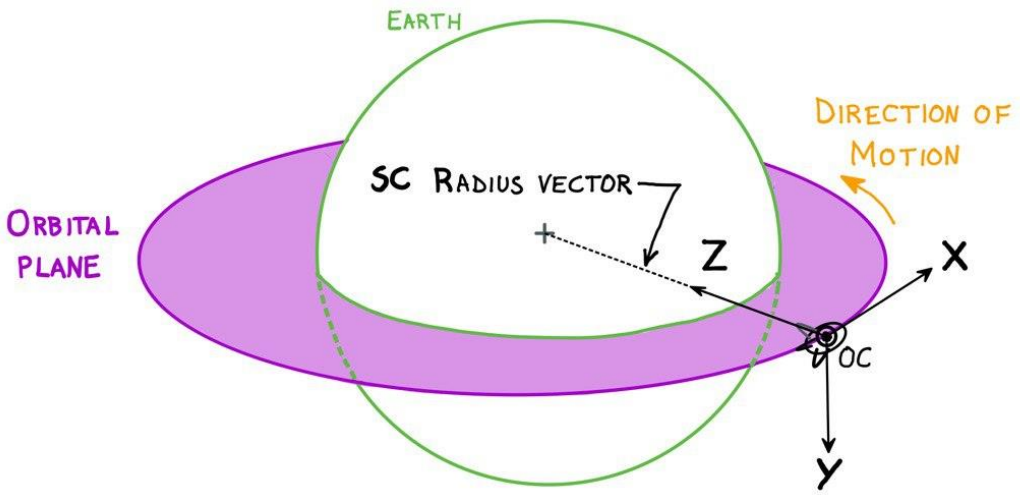


*Figure 3: LVLH Reference frame*

The LVLH is an orbital Earth-pointing reference frame with the origin coinciding with the spacecraft's center of mass. The reference frame is a right-handed coordinate system with the z-axis pointing toward the center of the Earth (Local Vertical), the x-axis pointing in the direction of orbital motion, and the y-axis perpendicular to the orbital plane. [13]. The CubeSat body frame has the origin coinciding with the observer satellite's center of mass, while the axes' orientation is related to the spacecraft shape and the use of a right-handed system. Attitude representations explain the orientation of the body frame; some of the most frequent representations are direction cosine matrices, Euler angles, and quaternions. In this work different representations are employed depending on the objective to be achieved:

- *Euler angles* are three angles that define rotations about the axis of a reference frame to represent the attitude of a rigid body in relation to the fixed coordinate system. As proven in [10] any proper attitude can be depicted by three Euler angles, in which two consecutive rotations must turn about different axes. In this essay, Euler angles are used to craft the reference attitude from the problem's geometric and kinematic parameters since they are more intuitive to work with. More precisely an intrinsic Tait-Bryan 123 rotation sequence is exploited since it allows one to reach any final orientation with only two of the three elemental

rotations, although it entails more complex calculations. The intrinsic convention is used since the reference attitude is defined by rotations about the axes of the rigid body reference frame. Euler angles are subject to the Gimbal lock phenomenon [14] which precludes their use for effective and robust numerical computations.

- *Quaternions* represent the modern alternative to Euler angles due to their low computational cost and their lack of singularity (Gimbal lock phenomenon). Consequently, they are exploited in the plant model and in the control system, as is better pictured in *chapter 3*.

Since the reference attitudes that successfully carry out the observation are devised using Euler angles, while the system model and controller utilize the quaternion to compute the control response, it is necessary to convert the three Euler angles representation into the corresponding unit quaternions. Given that for the *Euler rotation theorem [14]* each movement of a rigid body with at least one fixed point corresponds to a rotation about an axis that passes through the fixed point. The theorem suggests then that any rotation can be described with 2 quantities with a total of 4 variables, called the Euler parameters:

- A rotational angle $\beta$ (1 parameter)
- A rotational axis $\boldsymbol{u} = u_1\boldsymbol{i} + u_2\boldsymbol{j} + u_3\boldsymbol{k}$ (3 parameters)

The 4 Euler parameters can be viewed as the coefficients of a quaternion, which use the following parametrization:

$$q_0 = cos\frac{\beta}{2} \tag{2.1}$$

$$q_1 = u_1 sin\frac{\beta}{2} \tag{2.2}$$

$$q_2 = u_2 sin\frac{\beta}{2} \tag{2.3}$$

$$q_3 = u_3 sin\frac{\beta}{2} \tag{2.4}$$

with

$$\sqrt{\sum_{i=1}^{3} q_i^2} = 1 \qquad 2.5$$

With this notation, the four quaternion elements can describe the mathematical representation of the four Euler parameters with just 3 independent parameters. From the Euler rotation theorem, it is also proven [9] that any Euler representation can be provided in the quaternion form.

## 2.3 Helix trajectory and initial position

In the design of the reference attitudes, it is fundamental to know the satellite's initial position and relationship with the helix trajectory since the initial position set up all the subsequent values of the reference attitudes trajectory.

The satellite's initial position is given in cartesian coordinates while the helix trajectory can be easily described with the parameters of the problem ($V_x$, $P_t$, $r_h$) used as cylindrical coordinates. A relation is obtained by stating the circular helix trajectory in cartesian coordinates using the following equation.

$$x = V_x\, t - x0 \qquad 2.6$$

$$y = r_h\, cos\left(\left(-\frac{2\pi}{P_t} t\right) + \gamma_0\right) \qquad 2.7$$

$$z = r_h\, sin\left(\left(-\frac{2\pi}{P_t}\, t\right) + \gamma_0\right) \qquad 2.8$$

*with*

$$r_h = \sqrt{{z_{NC}}^2 + {y_{NC}}^2} \qquad 2.9$$

The initial position angle $\gamma_0$ of the cylindrical coordinates is obtained by imposing t = 0 in equation 2.7 or 2.8, the obtained equations are used in equation 2.10 to define the initial reference attitude.

Moreover, the trajectory equations are used to verify the reference attitude effectiveness once designed the satellite position with respect to the collaborative target but are not exploited to derive the reference attitude.

## 2.4 Reference acquisition procedure

At the start of the helix trajectory, the satellite begins the attitude control maneuver. The maneuver has the objective to keep the positive direction of the observer Satellite z-axis pointing toward the target Spacecraft barycenter which coincide with the center of the trajectory.

Given the direction for the z-axis, the observer satellite's y-axis is set in the same direction as the satellite's linear velocity, since the trajectory is circular, and the x-axis closes the set so that the Body Frame is right-handed.

By making use of the parameters which describe the helix trajectory, a suitable time variant reference direction for the z-axis must be derived. The vector which fulfills the task is the relative position vector $r_{sat/sc}$ defining the satellite position with respect to the origin of the spacecraft reference frame since the negative direction points from the satellite to the Spacecraft's origin. However, $r_{sat/sc}$ is not a constant vector, it changes with the satellite position which in turn changes with time, so the reference must describe how the position vector direction changes with respect to time.

As is already anticipated, with the Euler angles representation, a vector direction is defined using three parameters, which are angles between the rotating frame and the fixed frame. Since the reference is time-variant the Euler angles are used just to describe the initial reference attitude, while Euler angles velocities are employed to express the time evolution of that given initial orientation.

So, the reference attitude is composed of two parts:

1. First the *initial reference attitude* is defined from the satellite's initial position in the helix trajectory, specifying the angles of a intrinsic Tait–Bryan 123 rotation sequence.
2. Once the z-axis of the Observer Satellite is pointing toward the target spacecraft, the *Euler angles velocity* keeps the z-axis pointed while the satellite performs the helix trajectory. The satellite's kinematics must be exploited to evaluate the Euler angles velocities of the Tait–Bryan sequence.

## 2.5 Initial reference attitude definition

The Euler angles describing the initial orientation are defined using *a, r, z0,* and *y0*. The Intrinsic Tait–Bryan 123 rotation is composed of the following elementary rotations in the given order:

1. A rotation by $\phi$ about the Body Frame x-axis.
2. A rotation by $\theta$ about the Body Frame y'-axis.
3. A rotation by $\psi$ about the Body Frame z"-axis.

The target spacecraft LVLH frame is used as the initial reference frame of the observer satellite on which the rotations are applied. In this application, just two rotations are required to reach the initial reference attitude, one about the x-axis and one about the y'-axis.

The first Tait–Bryan's rotation about the x-axis is defined by the satellite's initial position. The initial position can be any point on the cycle defined by the circular helix trajectory radius *r* with the centerline coincident with the fixed frame $X_{FF}$-axis, the one highlighted in blue in *Figure 4*.

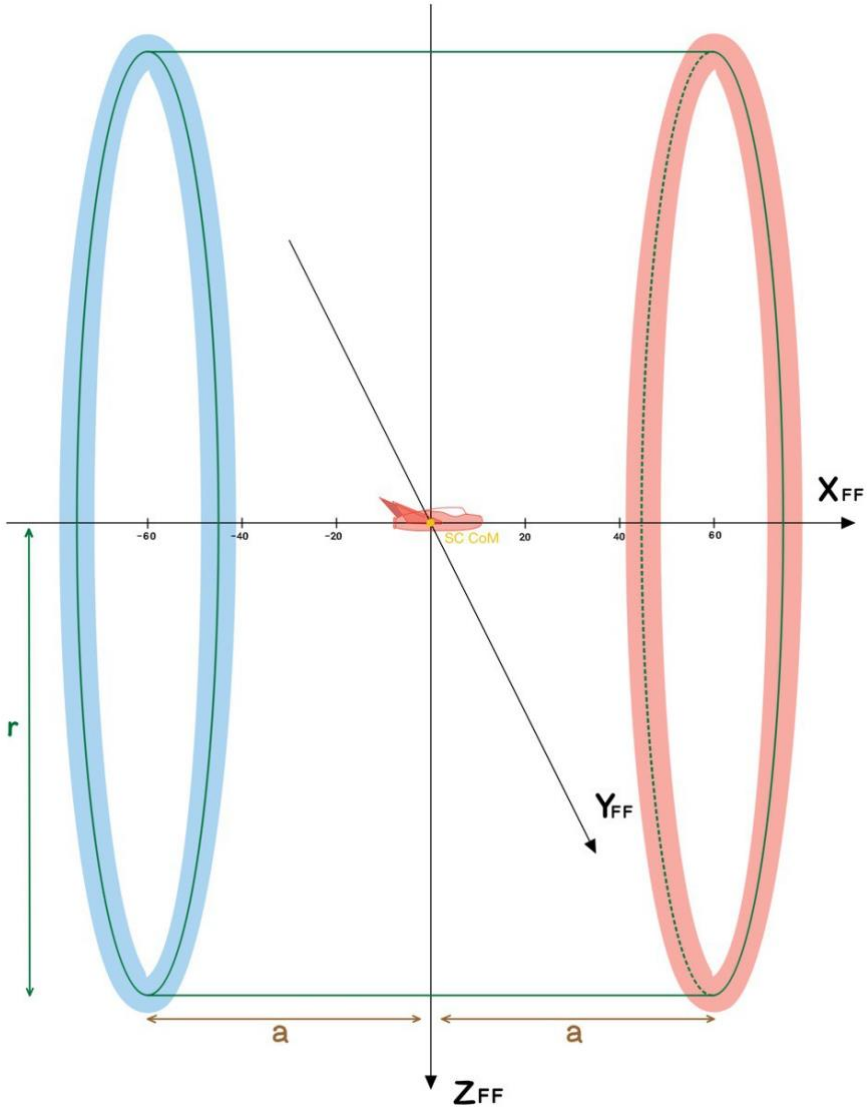


*Figure 4: In scale representation of the possible satellite's initial positions (highlight in blue) and final positions (highlighted in red).*

The angle of rotation $\phi_{r0}$ is defined by the MATLAB function *atan2* exploiting the *equations* 2.7 and 2.8 to find the initial orientation of the observer satellite with respect to the target spacecraft reference frame:

$$\phi_{r0} = atan2\,(-z0\,, y0\,) \qquad 2.10$$

The angle $\phi_{r0}$ can be easily visualized using the Y-Z plane of the coordinate system.

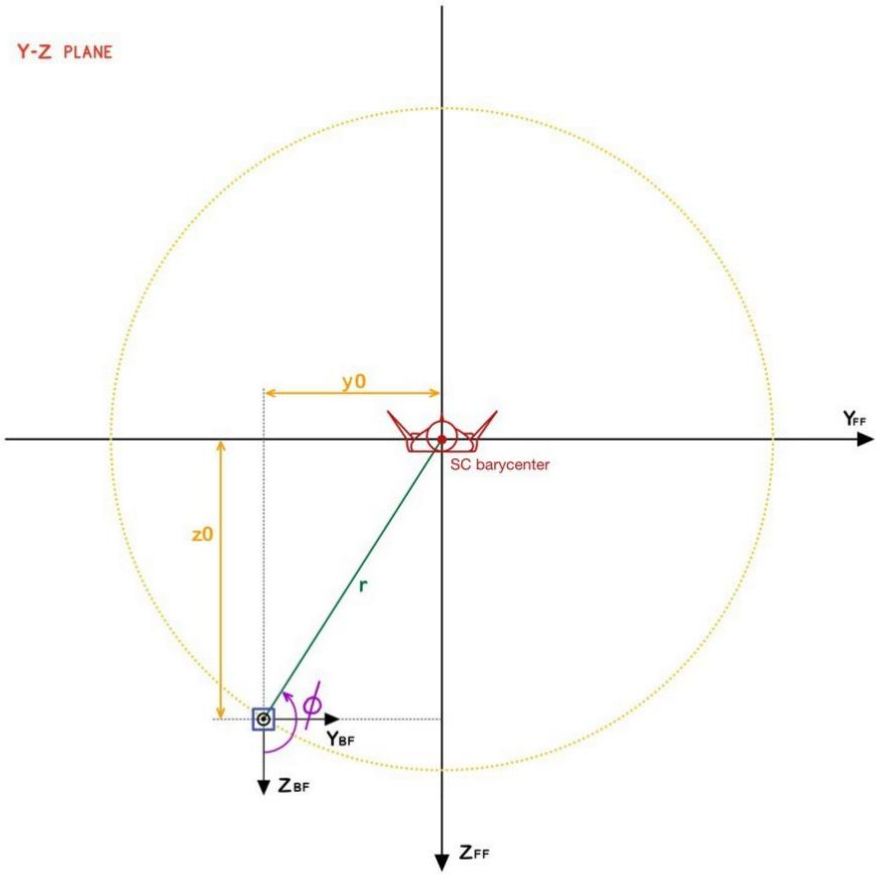


*Figure 5: representation of z0 and y0 in the Y-Z plane and the Euler angle $\phi_{r0}$. **r** is the projection on the plane Y-Z of $r_{sat/sc}$.*

It is represented in *Figure 5* as the angle between the satellite $Z_{BF}$-axis and *r,* where *r* is the projection of the satellite position vector on the Y-X plane. So, 2.10 returns $\phi_{r0}$ taking *z0* and *y0* as input.
When the satellite's initial position has negative *y0,* as in the case in *Figure 5,* the angle $\phi_{r0}$ spans from -0° to -180°. On the contrary, if *y0* is larger than zero, $\phi_{r0}$ will spam from 0° to 180°. So, when $\phi_{r0}$ is positive it defines a clockwise rotation while when it is negative a counterclockwise rotation. In this way 2.10 minimizes the satellite's first rotation about the x-axis for any initial position.
This first rotation sets the z-axis of the rotating frame on the same plane of the Spacecraft barycenter and there is a different $\phi_{r0}$ for each initial position.

The second rotation about the rotating frame's y-axis must center the satellite z-axis on target. The second angle $\theta_{r0}$ is shaped by the parameters *r* and *a*, the first parameter defines a length on the x-axis and the other the radius of a cycle: they can be seen as defining a cone with the tip in the center of the coordinate system and its axis coincides to the fixed frame x-axis ($X_{FF}$-axis in *Figure 6*).

The equation below returns the angle $\theta_{r0}$ represented in purple in *Figure 6*:

$$\theta_{r0} = atan2(r, a) \qquad 2.11$$

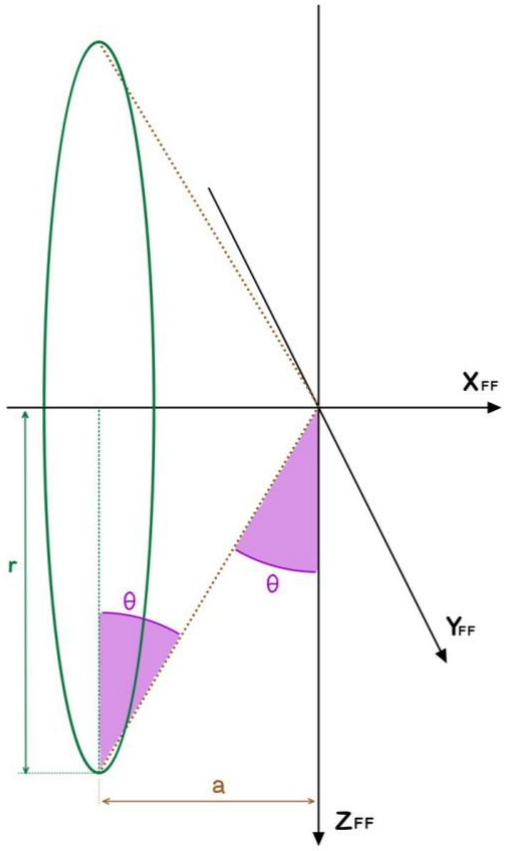


*Figure 6: Representation of the cone defined by r and a to derive the initial positions angle θ.*

As can be seen from *equation* 2.11, $\theta_{r0}$ is define by *r* and *a,* which are the same for any possible initial position. It means that the second rotation about the Body Frame y'-axis has the same span for any initial position. So, the second rotation amplitude is set by the trajectory geometry whereas the first rotation is defined by the satellite's initial position. The initial reference attitude is therefore described by an intrinsic Tait–Bryan 123 rotation as:

$$E_{r,0} = \begin{bmatrix} \phi_{0,r} = atan(y_0/z_0) \\ \omega_{0,r} = atan(a/r) \\ \psi_{0,r} = 0 \end{bmatrix} \qquad 2.12$$

## 2.6 Reference angular velocities definition

It is necessary to integrate the proper Euler angles velocities to derive the angles that describe the satellite's attitude in the subsequent time instants of the initial orientation.

The goal, in this case, is to find a relationship by means of angular velocity between the satellite motion, described with respect to the fixed frame, and the initial reference attitude. The Euler angles angular velocity is employed to establish the relationship between kinematic quantities of different reference frames. The angular velocity is expressed via Euler angles using the following convention:

1. Angular velocity $\dot{\phi}$ about x-axis.
2. Angular velocity $\dot{\theta}$ about y'-axis.
3. Angular velocity $\dot{\psi}$ about the satellite z"-axis.

The parameters representation in *Figure 7* shows how the rate of change of the angle $\theta$ is related to the satellite's linear velocity $V_x$. A mathematical relation between the two quantities can be derived:

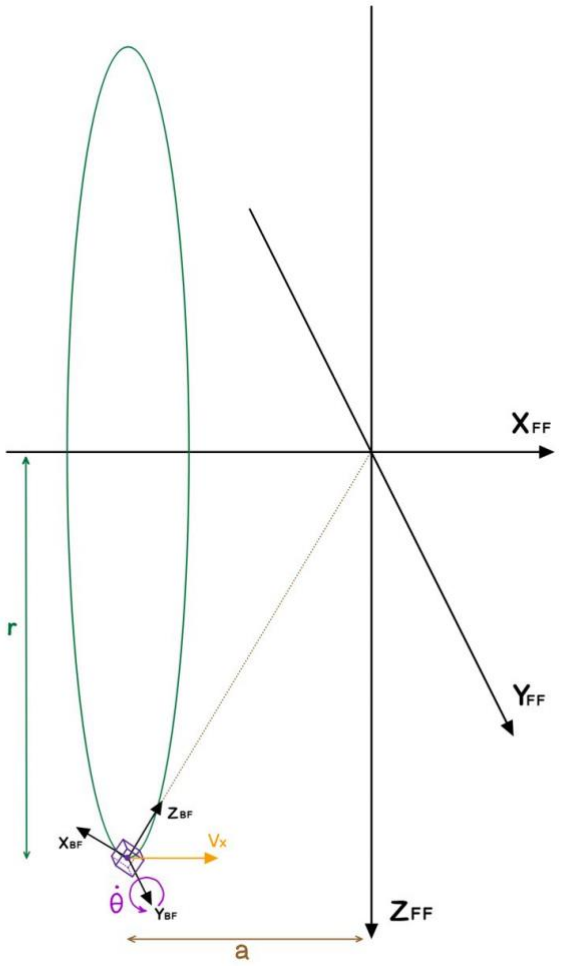


*Figure 7: Representation of the geometrical relation between $\dot{\theta}$, Vx vector, the radius of the helix trajectory r, and the distance a.*

$$\theta(t) = artan\left(\frac{r}{a - Vx \cdot t}\right) \qquad 2.13$$

Equation 2.13 returns the value of $\theta$ as a function of time, the equation output over the mission's time is plotted in *Figure 8*:

Instead of deriving 2.13 to find the behavior of $\dot{\theta}$, it is advantageous to approximate the function to a line, since the time evolution of $\theta$ has an almost linear behavior, as shown in the plot. This way its

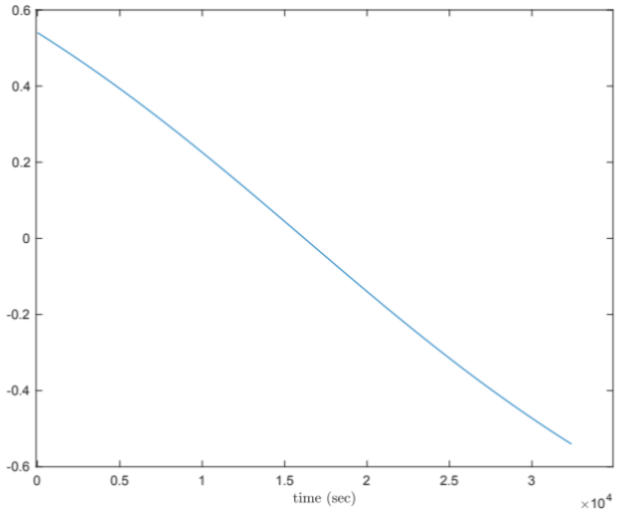


*Figure 8: Plot over time of θ, the unit on the y-axis unit is radiant.*

derivative would become far easier and have a time-invariant behavior. Exploiting the MATLAB function '*fit*' with the values of $\theta$ returns the polynomial function of the best-fitted line approximating the values of $\theta$.

$$\theta(t) = artan\left(\frac{r}{a - Vx \cdot t}\right) \cong p_1 t + p_2 \qquad 2.14$$

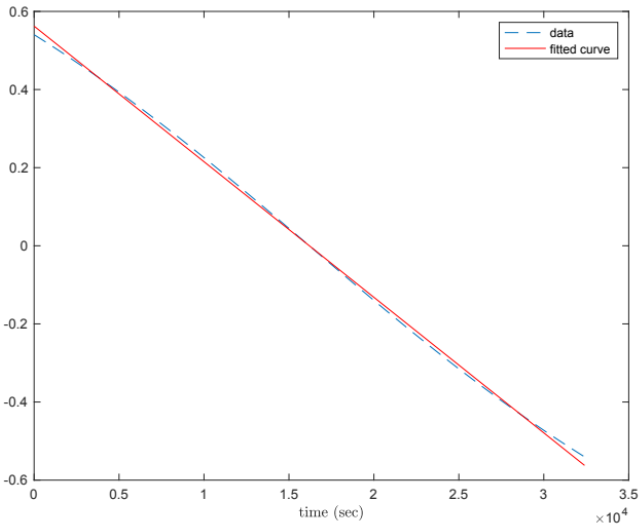


*Figure 9: Representation of the interpolating polynomial line (in red) and the values over time of θ (in blue).*

The angular coefficient $p_1$ of the linear polynomial curve (the red line in *Figure 9*) is the approximated value of $\dot{\theta}_r$.

$$\dot{\theta}_r = \frac{d}{dx}\left(artan\left(\frac{r}{a - Vx \cdot t}\right)\right) \cong p_1 \qquad 2.15$$

At last, the angular velocity $\dot{\phi}_r$ about the satellite x-axis must be defined. This velocity is easy to determine since it is derived by just one parameter, the complete turn period of the helix trajectory $P$

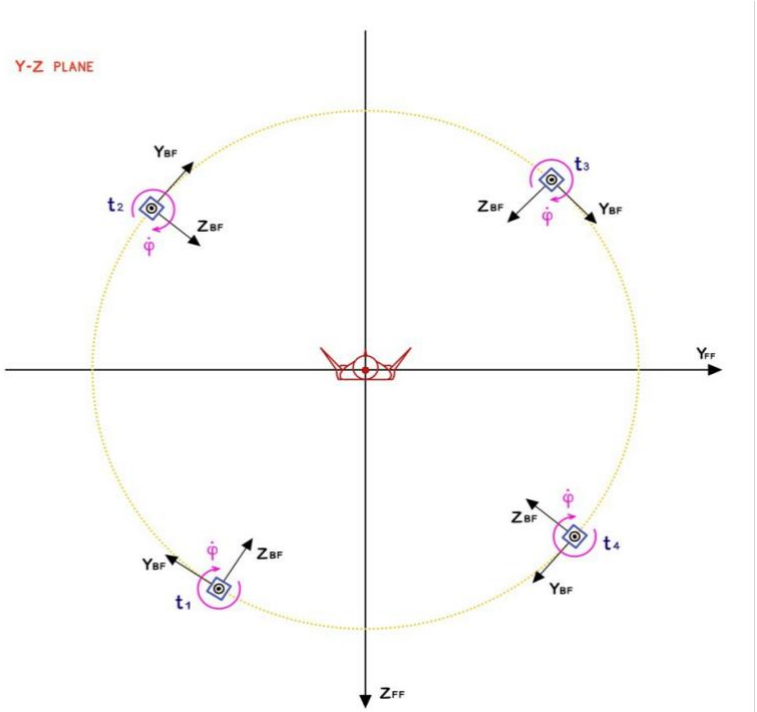


*Figure 10: Desired satellite motion on the Y-Z plane represented in four consecutive time-instant (t1 < t2 < t3 < t4).*

As *Figure 10* shows, the observer satellite rotates about its x-axis with the same period that the satellite uses to execute a complete turn period of the helix trajectory $P_t$ to keep the z-axis pointed on the target. From this relation a formula to find out $\dot{\phi}_r$ can be easily derived:

$$\dot{\phi}_r = \left(\frac{2\pi}{P_t}\right) \qquad 2.16$$

The body angular velocities vector is then

$$\dot{E}_r = \begin{bmatrix} \dot{\phi}_r = \left(\frac{2\pi}{P_t}\right) \\ \dot{\omega}_r \cong p_1 \\ \dot{\psi}_r = 0 \end{bmatrix} \qquad 2.17$$

# 3. Modelling and control design

This chapter is dedicated to the development of the simulators wherewith simulate the chosen control solution. Modeling is fundamentally the process of producing a mathematical representation, typically through a set of differential equations, of the physical system to be controlled. It is true that a good comprehension of the plant dynamics and the control tasks is needed to acquire a flexible but precise model for control design. A very precise model is rarely the best choice, because it may demand unreasonably complex control design, evaluations, and tougher computation. All this to say that the model needs to be designed taking into account the crucial properties while neglecting insignificant effects in the system dynamics.

The chapter starts focusing on the design of an ideal satellite model of the kinematic and dynamic to build a state space representation. Once the system mathematical model is known a suitable sliding mode control law is devised and adjusted to the task at hand. Then, to be more realistic, some of the most relevant external disturbances are modeled and included in the plant along with the limits of the actuation system. The simulator devised in this chapter is then exploited in Chapter 4 to choose and tune the control law.

## 3.1 Problem initial parameters

The problem's initial parameters are from the helix circular trajectory and the observer satellite,

| Parameters | Symbol | Value |
|---|---|---|
| mass | $m_c$ | 20 kg |
| base | b | 0.2 m |
| height | h | 0.2 m |
| depth | d | 0.3 m |
| x-axis inertia moment | $J_x$ | 0.2167 kg*m^2 |
| y-axis inertia moment | $J_y$ | 0.2167 kg*m^2 |
| z-axis inertia moment | $J_z$ | 0.0133 kg*m^2 |

Table 1: Satellite's parameters

| Parameters | Symbol | Value |
|---|---|---|
| Radius of the circular motion | r | 100 m |
| Distance from target SC | a | 60 m |
| Helix Pitch | $H_{pt}$ | 20 m |
| Helix complete turn period | $P_t$ | 5400 s |
| Initial position Y-axis | y0 | 25 m |
| Initial position Z-axis | z0 | 96.82 m |

Table 2: trajectory's parameters

## 3.2 Requirements definition

To evaluate whether the control solution can successfully carry out the observation is necessary to find a relationship between the attitude error and the observation quality. The target spacecraft's volume is approximated to a sphere in order to define the error for which the satellite's z-axis always intersects the sphere. The sphere is centered on the target center of mass, as illustrated in *Figure 11*.

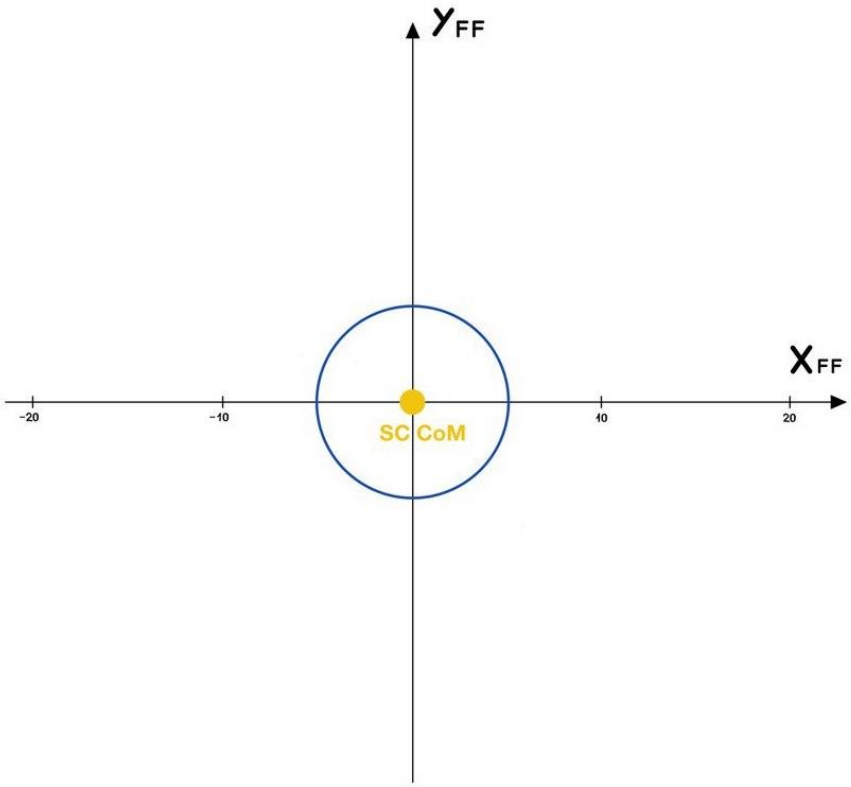


*Figure 11: Acceptance cone base representation on the X-Y plane of the fixed reference frame.*

As depicted in *Figure 12,* the trigonometric relation between the sphere radius and the distance *d* defines the angle α. Since the cycle radius is fixed, the only parameter that changes the values α along

the trajectory is the distance *d*, which is the distance between the observer and the target given by the trigonometric relation between the initial parameters *r* and *a*.

The absolute error imposed on the attitude is chosen considering the most onerous condition, which are the ones with the larger *d* along the satellite trajectory.

$$\alpha = 2\,artan\frac{r_{sp}}{d_{MAX}} \tag{3.1}$$

Considering the angle α the max absolute error is defined as

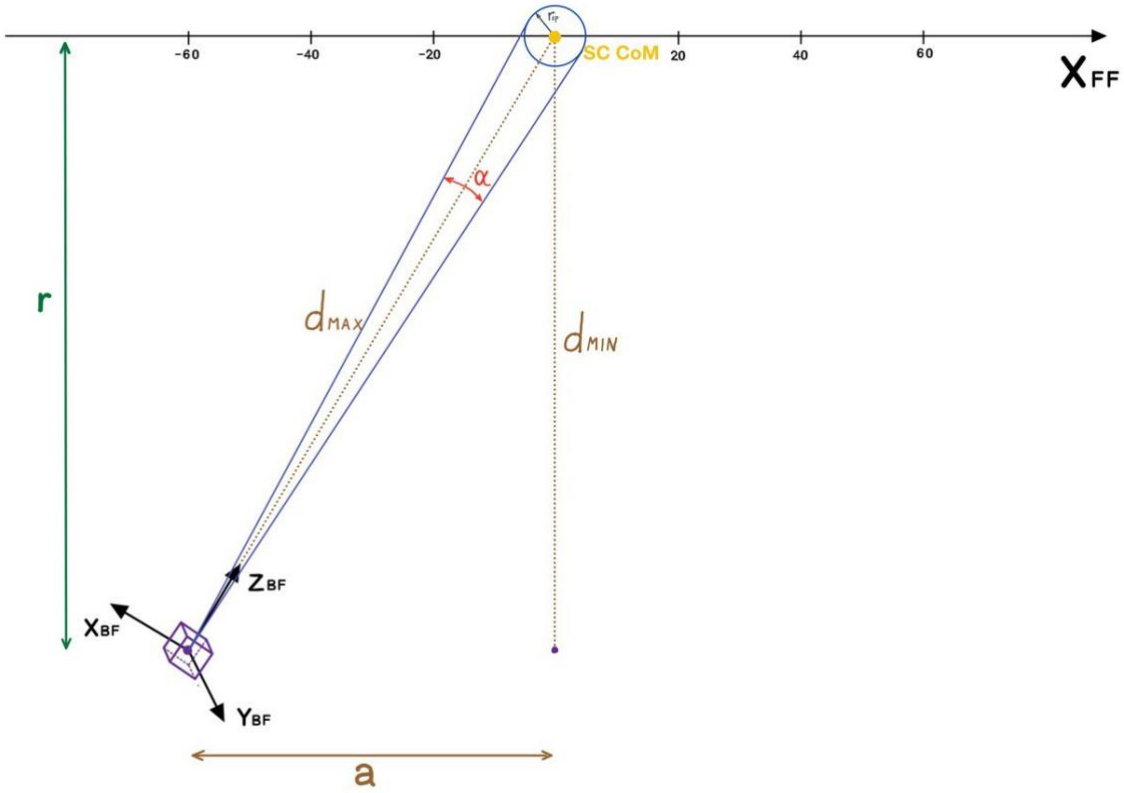


*Figure 12: Representation of the satellite at max distance (a) and min distance (b). The distance $h_a$ is chosen to consider the scenario with the lower angle α.*

$$\varepsilon_{max} = \left|\frac{\alpha}{2}\right| = 1.2° \tag{3.2}$$

From the derived maximum error and the implementation features, a suitable condition is obtained using as reference the requirements given as an example by ECSS paper ECSS-E-ST-60-10 [8]:

The absolute error shall be less than 1.2° on each axis, with APE < 10% and MPE < 12% for 98% of the problem's time.

## 3.3 Mathematical models

A simulation model created using a model-based design approach must be sufficiently precise to simulate the system dynamics in order to undertake the validation and performance testing of the attitude controller.

The state-space representation is a type of mathematical model of a physical system, differential equations or difference equations must be used to connect the input, output, and state variables in a state-space representation. The observer satellite attitude kinematic and dynamic equations are derived in order to put in relation the torque $M$ with the orientation $q$, the system's input and output. The satellite's model can be seen as a combination of two non-linear subsystems connected in series.

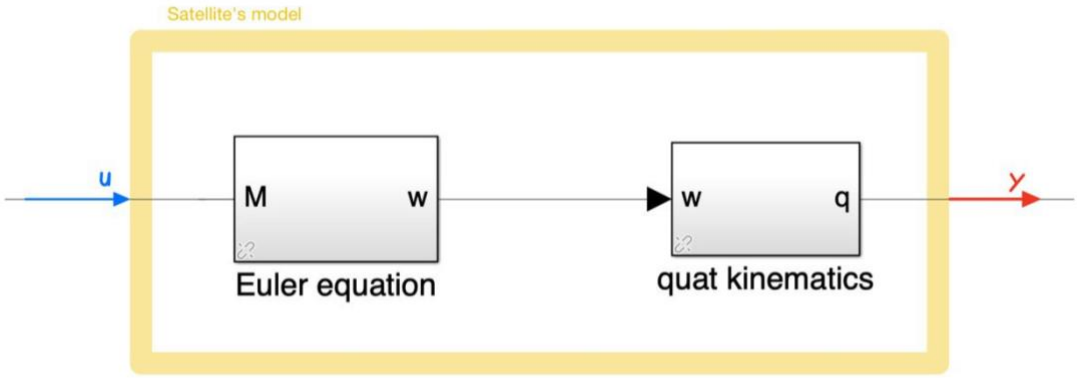


*Figure 13: Block scheme of the satellite's model. The input u corresponds to M and the output y to q.*

The state variables' values depend on the values of the input variables and the previous values of the state variables while the output values are derived from the values of the state variables.

### 3.3.1 Kinematic Model

The kinematic model is used to relate the time evolution of the quaternion $q$ with the satellite angular velocity components to exploit the quaternion kinematics [27]. The time derivative of the quaternion q(t) components and the components of the vector of angular velocity $\omega$(t) are correlated by the quaternion differentiation formula.

To introduce the principle, let's take the quaternion expression at the time instant t + Δt

$$q(t + \Delta t) = q(t) \otimes \Delta q(t) \qquad 3.3$$

Given the angular velocity magnitude $\omega$ and the vector $\boldsymbol{\omega}$, the rotation angle is defined as $\omega\Delta t$ for small $\Delta t$. If the rotation axis $\boldsymbol{u}$ has magnitude $|u| = 1$ then $\boldsymbol{\omega} = \omega\boldsymbol{u}$

Then, when $\Delta t$ is small

$$\Delta \boldsymbol{q} \cong \begin{bmatrix} cos\dfrac{\omega \Delta t}{2} \\ \boldsymbol{u}\, sin\dfrac{\omega \Delta t}{2} \end{bmatrix} \cong \begin{bmatrix} 1 \\ \boldsymbol{u}\dfrac{\omega \Delta t}{2} \end{bmatrix} = \begin{bmatrix} 1 \\ \dfrac{\boldsymbol{\omega} \Delta t}{2} \end{bmatrix} \quad 3.4$$

Applying the derivative definition

$$\dot{\boldsymbol{q}} = log_{\Delta t \to 0} \frac{\boldsymbol{q}(t + \Delta t) - \boldsymbol{q}(t)}{\Delta t} = log_{\Delta t \to 0} \frac{\boldsymbol{q} \otimes \Delta \boldsymbol{q} - \boldsymbol{q}}{\Delta t} \quad 3.5$$

$$= log_{\Delta t \to 0} \frac{\boldsymbol{q} \otimes (\Delta \boldsymbol{q} - (1, \boldsymbol{0}))}{\Delta t} = log_{\Delta t \to 0} \frac{\boldsymbol{q} \otimes \left( \left(1, \dfrac{\boldsymbol{\omega} \Delta t}{2}\right) - (1, \boldsymbol{0}) \right)}{\Delta t} \quad 3.6$$

$$= log_{\Delta t \to 0} \frac{\boldsymbol{q} \otimes \left(0, \dfrac{\boldsymbol{\omega} \Delta t}{2}\right)}{\Delta t} = \frac{1}{2} \boldsymbol{q} \otimes (0, \boldsymbol{\omega}) = \frac{1}{2} Q \boldsymbol{\omega} \quad 3.7$$

Therefore, the quaternions kinematic equation used in the kinematic model is

$$\dot{q} = \frac{1}{2} Q \boldsymbol{\omega} \quad 3.8$$

where

$$Q = \begin{bmatrix} q_0 & q_1 & q_2 & q_3 \\ q_1 & q_0 & -q_3 & q_2 \\ q_2 & q_3 & q_0 & -q_1 \\ q_3 & -q_2 & q_1 & q_0 \end{bmatrix}, \ \omega = \begin{bmatrix} \omega_1 \\ \omega_2 \\ \omega_3 \end{bmatrix} \text{ and } q = \begin{bmatrix} q_0 \\ q_1 \\ q_2 \\ q_3 \end{bmatrix} \quad 3.9$$

Integrating the quaternion kinematic equations allows us to compute $\dot{q}$ from $\omega_1$, $\omega_2$ and $\omega_3$. From the integration of $\dot{q}$ a quaternion representing the current satellite attitude is derived and fed to the other sub-systems.

### 3.3.2 Dynamic Model:

The model uses attitude dynamic equations for a rigid body in rotational motion.

To understand the relationship between *M* and *q,* the input and the output of the satellite's model illustrated in *Figure13,* it is necessary to define the angular momentum of the body inertial matrix first. Assuming that a *body frame BF* is rotating with angular velocity $\boldsymbol{\omega} = \omega_1 \mathbf{X_{BF}} + \omega_2 \mathbf{Y_{BF}} + \omega_3 \mathbf{Z_{BF}}$ in an *inertial reference frame IF*.

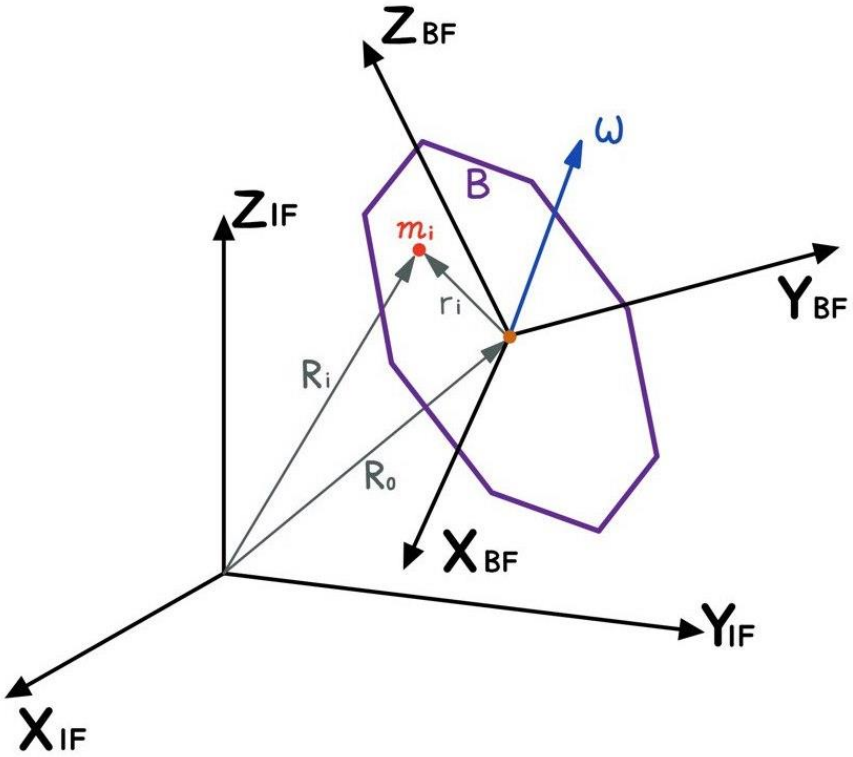


*Figure 14: The rigid body B rotating with respect to an inertial reference frame with angular velocity*

So, the derivative of $R_i$ can be written as

$$\dot{\boldsymbol{R}}_{\boldsymbol{i}} = \dot{\boldsymbol{R}}_{\boldsymbol{0}} + \dot{\boldsymbol{r}}_{\boldsymbol{i}} + \boldsymbol{\omega} \times \boldsymbol{r}_{\boldsymbol{i}} \qquad 3.10$$

Where $\boldsymbol{\omega}$ is the body frame angular velocity vector in the inertial frame. The angular momentum with respect to the IF of a particle $m_i$ is

$$\boldsymbol{H}_{\boldsymbol{i}} = \boldsymbol{r}_{\boldsymbol{i}} \times m_i \dot{\boldsymbol{R}}_{\boldsymbol{i}} = \boldsymbol{r}_{\boldsymbol{i}} \times m_i \left( \dot{\boldsymbol{R}}_{\boldsymbol{0}} + \dot{\boldsymbol{r}}_{\boldsymbol{i}} + \boldsymbol{\omega} \times \boldsymbol{r}_{\boldsymbol{i}} \right) \qquad 3.11$$

Moreover, since a rigid body is considered, the particle position with respect to the body reference frame $r_i$ is constant for any particle $m_i$ it can be written as

$$\boldsymbol{H}_{\boldsymbol{i}} = \boldsymbol{r}_{\boldsymbol{i}} \times m_i \left( \dot{\boldsymbol{R}}_{\boldsymbol{0}} + \boldsymbol{\omega} \times \boldsymbol{r}_{\boldsymbol{i}} \right) = -\dot{\boldsymbol{R}}_{\boldsymbol{0}} \times m_i \boldsymbol{r}_{\boldsymbol{i}} + m_i (\boldsymbol{\omega} \times \boldsymbol{r}_{\boldsymbol{i}}) \qquad 3.12$$

The entire body's angular momentum is computed by summing the momentum of all the particle

$$\boldsymbol{H} = -\sum_i \dot{\boldsymbol{R}}_{\boldsymbol{0}} \times m_i \boldsymbol{r}_{\boldsymbol{i}} + \sum_i \boldsymbol{r}_{\boldsymbol{i}} \times m_i (\boldsymbol{\omega} \times \boldsymbol{r}_{\boldsymbol{i}}) = \qquad 3.13$$

$$= -\dot{\boldsymbol{R}}_{\boldsymbol{0}} \times \sum_i m_i \boldsymbol{r}_{\boldsymbol{i}} + \sum_i \boldsymbol{r}_{\boldsymbol{i}} \times m_i (\boldsymbol{\omega} \times \boldsymbol{r}_{\boldsymbol{i}}) \qquad 3.14$$

Since the particles position with respect to the body frame origin is fixed, the angular momentum can be written as

$$\boldsymbol{H} = \boldsymbol{r_i} \times (\boldsymbol{\omega} \times \boldsymbol{r_i})\, m_i \tag{3.15}$$

Hence for $m_i \to dm$ become

$$\boldsymbol{H} = \int_B \boldsymbol{r_i} \times (\boldsymbol{\omega} \times \boldsymbol{r_i})\, dm \tag{3.16}$$

If the angular velocity is expressed as $[\omega_1\ \omega_2\ \omega_3]^T$ the integral above can be stated in matrix form

$$\boldsymbol{H} = \begin{bmatrix} J_{11} & J_{12} & J_{13} \\ J_{21} & J_{22} & J_{23} \\ J_{31} & J_{32} & J_{33} \end{bmatrix} \begin{bmatrix} \omega_1 \\ \omega_2 \\ \omega_3 \end{bmatrix} = \boldsymbol{J\omega} \tag{3.17}$$

Where J is the CubeSat tensor of inertia (written in matrix form) about the center of mass with respect to the BF reference axes $\mathbf{X_{BF}}$ $\mathbf{Y_{BF}}$ $\mathbf{Z_{BF}}$. The tensor of inertia provides insight into the mass distribution in a rigid body. For a general three-dimensional body, there is always the possibility to find a reference frame for which the products of inertia are zero. As a result, the inertia matrix gets a diagonal form [12]. From a practical point of view, the products of inertia are zero implying a diagonal inertial matrix when the inertia contribution of the body on the positive side of the axis is equal to the contribution on the negative ones.

Since the moment of inertia about the principal centroidal axis of a uniform solid cuboid have a precise formula, the J diagonal matrix of the observer satellite can be written as

$$J = \begin{bmatrix} \frac{1}{12}m(d^2 + b^2) & 0 & 0 \\ 0 & \frac{1}{12}m(d^2 + h^2) & 0 \\ 0 & 0 & \frac{1}{12}m(h^2 + b^2) \end{bmatrix} \tag{3.18}$$

Now, given a torque *M* exerted on the satellite

$$M = \begin{bmatrix} m_1 \\ m_2 \\ m_3 \end{bmatrix} \tag{3.19}$$

As shown in [14], by applying the II law of dynamic for rotation, the following relation between the angular momentum and the torque M, the Euler's equation of rotation [29] is derived:

$$\dot{\boldsymbol{H}} = \boldsymbol{M} \tag{3.20}$$

since

$$\dot{\boldsymbol{H}} = \dot{\boldsymbol{H}}_B + \boldsymbol{\omega} \times \boldsymbol{H} \tag{3.21}$$

and

$$\mathbf{H} = \mathbf{J\omega} \qquad \dot{\mathbf{H}}_B = \mathbf{J\dot{\omega}} \tag{3.22}$$

the Euler's equation of rotation is obtained

$$\boldsymbol{J\dot{\omega} = M - \omega \times J\omega} \qquad 3.23$$

with

$$\boldsymbol{\omega} \times = \begin{bmatrix} 0 & -\omega_3 & \omega_2 \\ \omega_3 & 0 & -\omega_1 \\ -\omega_2 & \omega_1 & 0 \end{bmatrix} \qquad 3.24$$

Equation 3.23 is the mathematical model implemented inside the dynamic block.

Together the kinematic and dynamic blocks describe the whole satellite behavior that needs to be known for attitude control applications.

## 3.4 Control design

Sliding mode control is a nonlinear control technique presenting well-known properties of stability, robustness, and easy tuning and application. This control strategy revolves around driving and keeping the system states on a predefined surface inside the state space. When within the surface the system behavior is identified as *ideal sliding motion*, in this state the system becomes unaffected by parameter variations. For this reason, this approach is fitted for a robust controller working with an uncertain system.

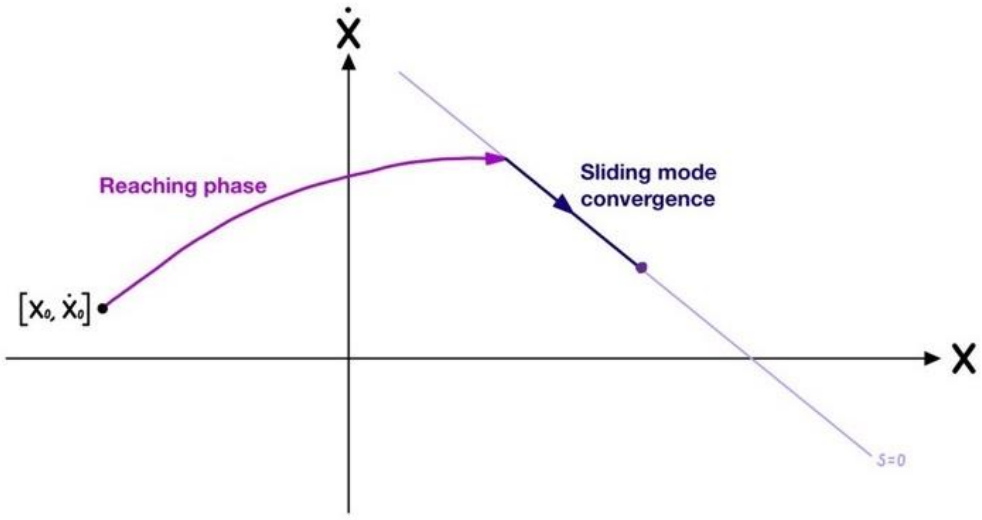


*Figure 15: Sliding mode controller graphical representation*

The sliding mode control is a two-part controller which is thus designed in two steps: a suited surface is defined in the state space to meet the conditions required by the problem. Then a control law is devised in such a way as to move the system states in the direction of the sliding surface with a discontinuity about the surface. The close loop behavior of this control method varies between two different types of motion based on the position of the state trajectory: when outside the sliding surface

the control law drives the states towards the surface, called the *reaching phase*. Once the system reaches the surface, the *siding motion* begins making the system not affected by uncertainty. Since the system is still sensitive to disturbances in the reaching phase, the phase should be designed as short as the problem allow [18]. The main drawback of this class of controller is the presence of chattering, an unwanted high-frequency motion that may excite unmodeled dynamics.

Let's introduce the sliding-mode control by considering a SISO nonlinear system affine in u, the same of the satellite's model, of the form

$$\dot{x} = f(x) + g(x)\, u \qquad 3.25$$

$$y = h(x) \qquad 3.26$$

where x ∈ $R^n$ is the state vector, u ∈ R is the command input, y ∈ R is the output, and f, g, and h are three smooth functions of $R^n$. Establishing the output y(t) is necessary to track a given reference r(t). If the controlled system is required to follow the reference signal r(t), the tracking error is $\tilde{y} = y - r$. The purpose of the control problem is to produce a tracking error as low as practicable, and where possible, convergent to zero. The sliding surface is identified as:

$$\mathrm{S(t)} = \{\mathrm{x} \in \mathrm{R^n} : \mathrm{s(t)} = 0\} \qquad 3.27$$

s(t) is a function in $\mathrm{R^{n+1}} \rightarrow \mathrm{R}$:

$$s(x,t) = \left\{\tilde{y}^{(\gamma-1)} + K_\gamma \tilde{y}^{(\gamma-2)} + \ldots + K_2 \tilde{y}\right\} \qquad 3.28$$

where $K_i$ are chosen so that every polynomial root has a negative real part

$$P\,(\gamma) = \left\{\lambda^{(\gamma-1)} + K_\gamma \lambda^{(\gamma-2)} + \ldots + K_2\right\} \qquad 3.29$$

This way, when the trajectory is inside the sliding surface, the tracking error $\tilde{y}$ rapidly gets to 0, as implied by the roots of P (λ). The control law u is designed to impose a sliding surface S both invariant and attractive:

- If S is an invariant set, once the trajectory is on the sliding surface S, it remains on it.
- If S is attractive, when the trajectory is outside the surface S, it is forced to move toward it.

The system motion on the sliding surface is called sliding mode.

Supposing that at time *t* the trajectory is on the sliding surface, it can be deduced that

$$s(x(t), t) = 0 \qquad 3.30$$

To guarantee that S is an invariant set, it is a requisite that:

$$\dot{s}(x(t), t) = 0 \qquad 3.31$$

From the definition of s in equation 3.28, the equation 3.30 can be formulate as:

$$\tilde{y}^{\gamma} + K_\gamma \tilde{y}^{(\gamma-1)} + \ldots + K_2 \dot{\tilde{y}} = 0 \qquad 3.32$$

where

$$\tilde{y}^{\gamma} = y^{\gamma} - r^{\gamma} = y^{\gamma} - a(x) - b(x)u \qquad 3.33$$

by solving for u the control law is obtained:

$$u_s = \frac{1}{b(x)}\left(r^{\gamma} - a(x) + K_{\gamma}\tilde{y}^{(\gamma-1)} + \ldots + K_2\dot{\tilde{y}}\right) \qquad 3.34$$

In order to make S an attractive surface a discontinuous term is added:

$$u = u_s + K_1 sign(s) \qquad 3.35$$

However, because of the discontinuity in the term sign(s), chattering may be induced. The sigmoid function $\tanh(\eta s)$ is used as an approximation of the sign(s) function to tackle the problem. η is a design parameter that represents the slope of the approximated sign.

$$sign(s) \cong tanh(\eta s) \qquad 3.36$$

$$u = u_s + K_1\, tanh(\eta s) \qquad 3.37$$

In the application under study the goal is to make the state vector track a time-varying reference vector. The states vector is taken from the state space representation of the system. The state equations of the system mathematical model are

$$\left\{ \begin{array}{c} \dot{q} = \frac{1}{2} Q \times \omega \\ \dot{\omega} = -J^{-1}\omega \times J\omega + J^{-1}u \end{array} \right\} \qquad 3.38$$

In this application given the body inertial matrix *J,* the problem variables are:

$$\boldsymbol{\omega} = \begin{bmatrix} \omega_1 \\ \omega_2 \\ \omega_3 \end{bmatrix},\ q = \begin{bmatrix} q_1 \\ q_2 \\ q_3 \\ q_4 \end{bmatrix}, \qquad 3.39$$

the state vector is

$$x = \begin{bmatrix} q \\ \omega \end{bmatrix} \qquad 3.40$$

the input u is

$$u = \begin{bmatrix} u_1 \\ u_2 \\ u_3 \end{bmatrix} \qquad 3.41$$

and the output to control is the satellite orientation

$$y = \boldsymbol{\omega} = \begin{bmatrix} \omega_1 \\ \omega_2 \\ \omega_3 \end{bmatrix} \qquad 3.42$$

The goal of the control application is to make the *state vector x* follow a time variant *reference vector* $x_r$.

$$x_r = \begin{bmatrix} q_r \\ \omega_r \end{bmatrix} \tag{3.43}$$

Since the objective is the satellite stabilization about a reference attitude under the influence of disturbances, the tracking error between the body states $x$ and the desired body states $x_r$ must be computed. Therefore, two new quantities are defined, the angular velocity tracking error

$$\tilde{\omega} = \omega_r - \omega; \tag{3.44}$$

and the quaternion tracking error

$$\tilde{q} = q^{-1} \otimes q_r = q^{-1} \otimes q_r \tag{3.45}$$

Both quantities are measures of the difference in actual performance between the states and their reference. The optimum outcome would be for both tracking errors to converge to 0 in a finite amount of time.:

$$\tilde{\omega} \to 0 \text{ and } \tilde{q}(t) \to \begin{bmatrix} 1 \\ 0 \\ 0 \\ 0 \end{bmatrix} \tag{3.46}$$

As mentioned, the Sliding Mode Controller design entails two design phases: *Sliding Surface design* and *Control Input design.*

Sliding Surface design

Since the system to be controlled, represented in 3.38, is a Generalized Normal form the Sliding Surface function is defined as

$$s(q, \omega, t) = \tilde{\omega} + k_2 \tilde{q} \tag{3.47}$$

To be an attractive invariant set the sliding surface needs a suited control law.

Control input design

In order to guarantee $s(q, \omega, t)$ is an invariant set, the input has to satisfy the equation below

$$u_s = J\left(\dot{\omega}_r + \frac{k_2}{2}\left(\tilde{q}_0\, \tilde{\omega} + \tilde{q} \times (\omega_r + \omega)\right)\right) + \omega \times J\omega \tag{3.48}$$

then another term is added to make the surface attractive

$$u = u_s + k_1\, J\, tanh(\eta s) \tag{3.49}$$

## 3.5 Referencesignals generator design:

The control law chosen in the previous paragraph needs to be fed with the reference quaternion $q_r$, the reference angular velocity $\omega_r$ and the reference angular velocity derivative $\dot{\omega}_r$.

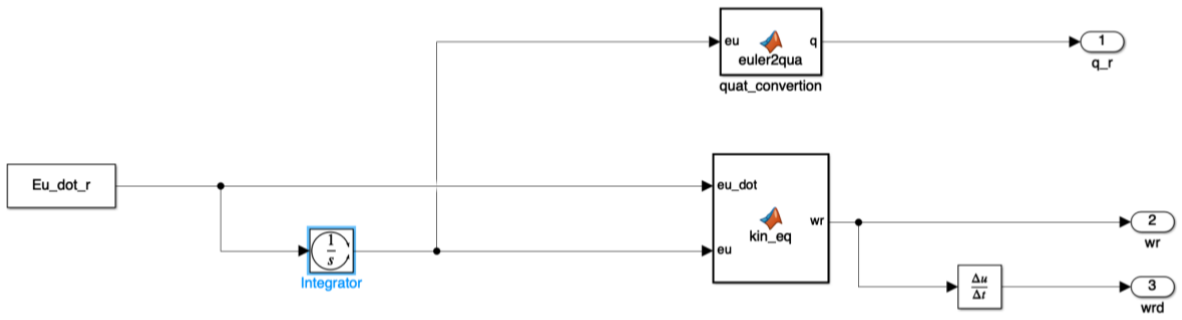


*Figure 16: Sub-system generating the references $q_r$, $\omega_r$ and $w_{rd}$.*

Starting from the reference angular velocities $\dot{E}_{r0}$ and the initial reference attitude $E_{r0}$ a reference signals generator is assembled using a Simulink model to produce the reference signals. As *Figure 16* shows, the reference signals required by the tracking problem are be derived through the $E_{r0}$, the satellite's initial reference attitude, and $\dot{E}_{r0}$, the reference Euler angles angular velocity, both defined in the previous chapter. The 'integrator' block initial condition value is the vector $E_{r0}$. The integrator is set in wrap mode, wrapping the state between -π and π.

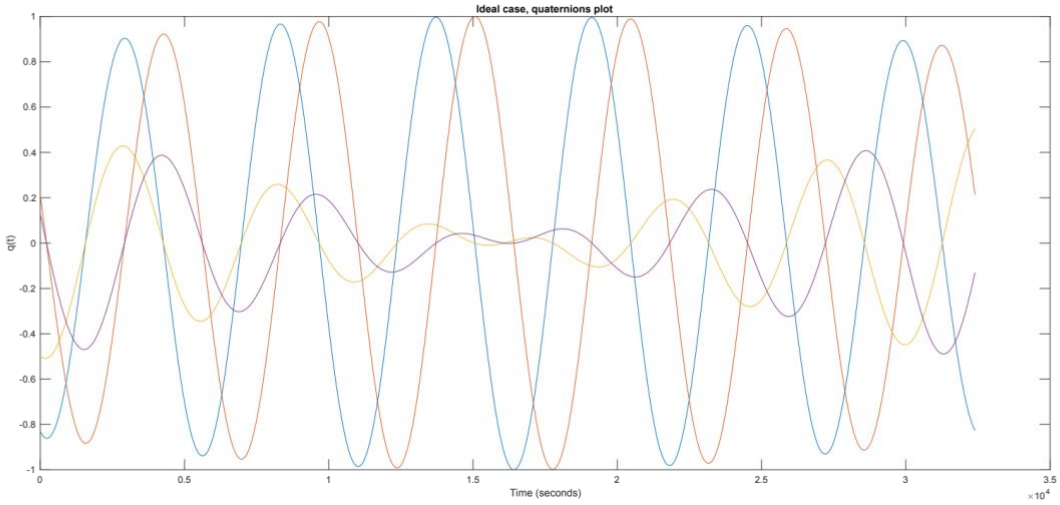


*Figure 17: Reference quaternions $q_r$ (t) plot over time.*

As F*igure 17* outlines, the satellite must accomplish six turns of the helix trajectory to carry out the mission. It can also be noticed from *Figure 18* and *19* that the angular velocity magnitude has its minimum at the end of the third turn.

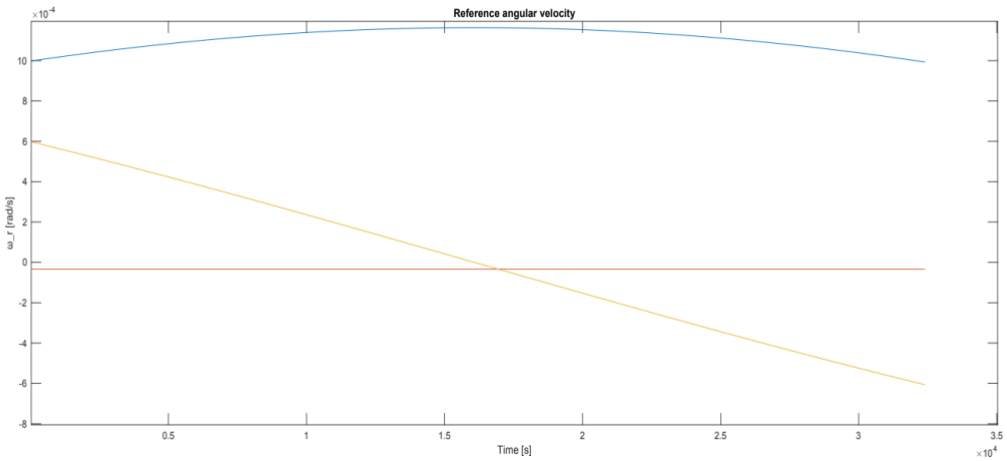


*Figure 18: Reference angular velocity $\omega_r$ plot over time.*

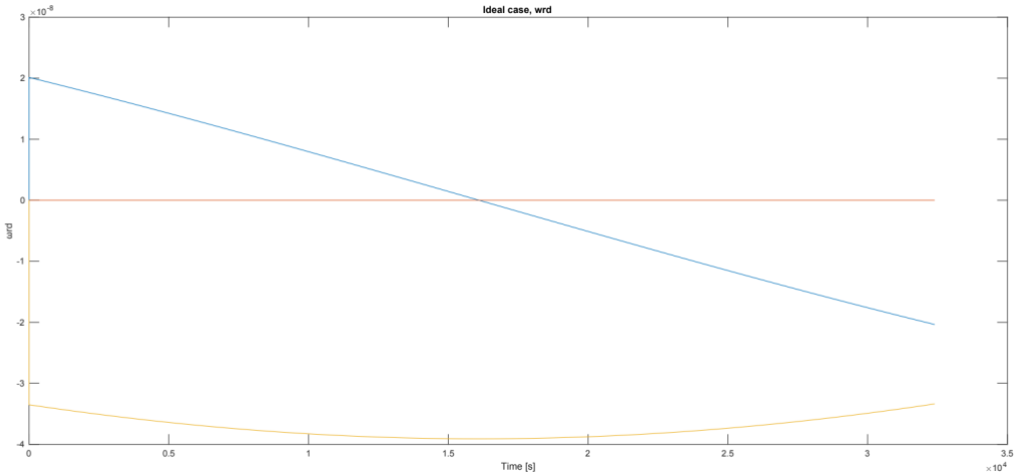


*Figure 19: Reference angular velocity derivative $\omega_r d$ plot over time.*

## 3.6 Disturbance and model uncertainty

The differences between the nominal model and the actual physical system are known as model uncertainty. Parametric uncertainties are those that relate to parameters, whereas non-parametric uncertainties are all other uncertainties. In this model, for example, the uncertainty in m, $m$, $\boldsymbol{q_0}$ and $\boldsymbol{\omega_0}$ are parametric uncertainties, whereas the neglected dynamics are non-parametric uncertainties. Both these uncertainties compose the system's internal disturbances. On the other hand, external disturbances need to be considered in the control design of the plant model, which means they must be known to be taken into account. The external moment of the body M, used in equation 3.23, can therefore be seen as a sum of multiple torques:

$$\boldsymbol{M = M_{external} + M_{internal} + M_{input}} \qquad 3.50$$

Where $\boldsymbol{M_{input}}$ is the torque defined by the control law while the other two terms are generated by the noises. The satellite attitude is continuously disturbed by several phenomena producing disturbance torques. $\boldsymbol{M_{external}}$ is the sum of the torques of the external disturbances while $\boldsymbol{M_{internal}}$ is the sum of the disturbances due to uncertainties. The external disturbances are shaped by the known space environment forces that affect the satellite dynamic. Instead, internal disturbances are produced inside the system, generally because of wrong measurements or manufacturing defects which leads to inserting an error into the torque computation. Both kinds of disturbances need to be attenuated by the control algorithm to guarantee stability.

Different external sources of environmental disturbance are modeled: *gravity gradient*, *residual magneto torque* and *aerodynamic drag*.

Gravity gradient disturbance

Gravity gradient effects are produced by differences in the attraction force intensity on the satellite's body when it enters a gravitational field. Inside a field, the parts of the satellite which are closer to the source are subject to greater gravitational force. This difference between the forces exercised on the satellite's body results in a disturbance torque. The expression below is defined considering the Earth's gravitational field:

$$\tilde{g} = -\left(\frac{GM}{r^2}\right)\hat{r} \qquad 3.51$$

where $G$ is the gravitational constant, $r$ the distance from the center of mass and M is the mass of the Earth.

$$\overline{T_g} = -3\omega^2 \hat{r} \times J \cdot \hat{r} \qquad 3.52$$

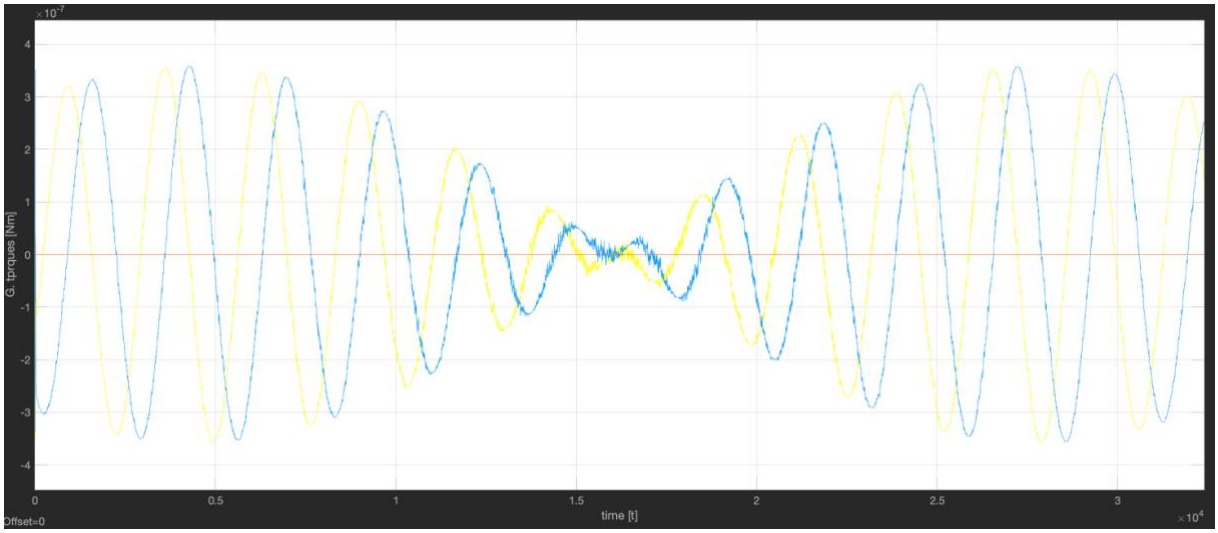


*Figure 20: Plot of the gravity gradient torque the satellite undergoes during the mission.*

Disturbance dipole torque

A magnetic disturbance torque is created as a result of interactions between the Earth's magnetic field and the spacecraft's residual magnetic dipole. So, the satellite's steady state magnetic dipole, which is generated by the electrical currents and ferromagnetic material, interacts with the Earth's magnetic field imparting a torque on the spacecraft.

$$\overline{T_{m_r}} = \overline{m_r} \times \bar{B} \qquad 3.53$$

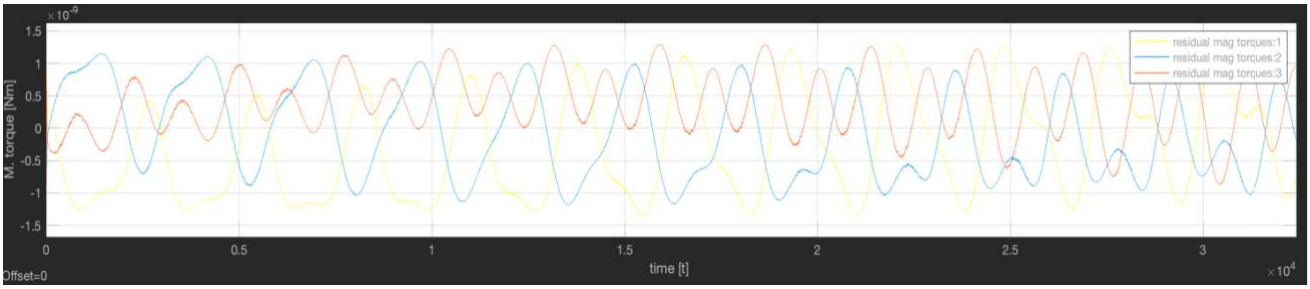


*Figure 21: Plot of the dipole torque the satellite undergoes during the mission.*

Drag torque

Drag is a force exerted on an object moving through a fluid and is oriented in the direction of relative fluid flow. Drag tends to slow down an item because it operates in the opposing direction of motion.

$$F_D = \frac{1}{2} C_D A \rho V^2 \qquad 3.54$$

Where:

- $C_D$ is the ballistic coefficient,
- $A$ the reference area
- $\rho$ is the atmosphere density
- $V$ the velocity of the fluid flow with respect to the CubeSat.

The air resistance in LEO orbit is still strong enough to produce drag force that can turn into a torque if the center of pressure of the satellite is far from the center of mass.

$$\overline{T_D} = \overline{r_{cp}} \times \overline{F_D} \qquad 3.55$$

where $r_{cp}$ is the distance between the center of mass and the center of pressure.

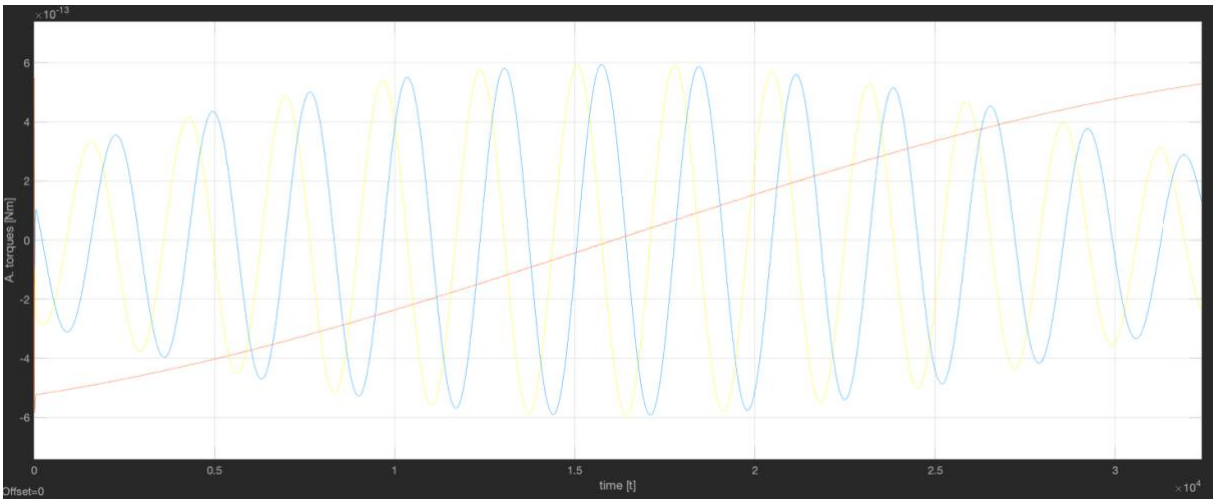


*Figure 22: Plot of the Drag torque the satellite undergoes during the mission.*

## 3.7 More realistic models

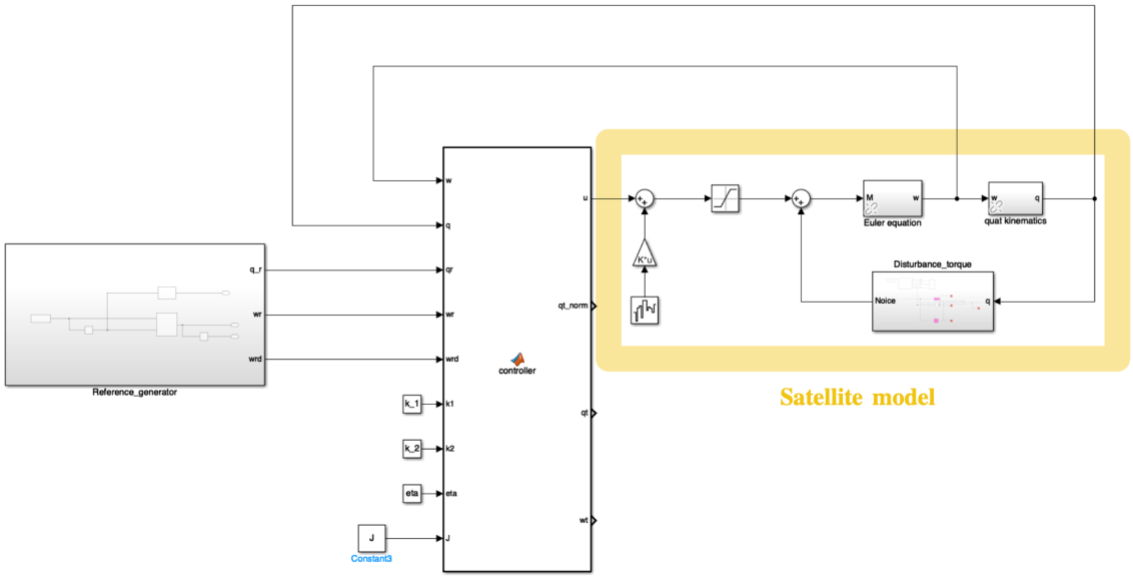


*Figure 23: The figure shows the full model structure with the Reference signal generator block, the controller block in the middle and the satellite's model defined by the blocks inside the yellow rectangle. The error torques are computed from the satellite orientation for every time instant and then sum together.*

To make the model more realistic several additions are made. The realistic error torques of the space environment defined in 3.50 are included in the mathematical model of the spacecraft by means of the block "Distrubance_torques". The block, as represented in *Figure 24*, takes the current attitude $q$ as input to delineate the satellite's relative position with respect to Earth, necessary to compute the external disturbances.

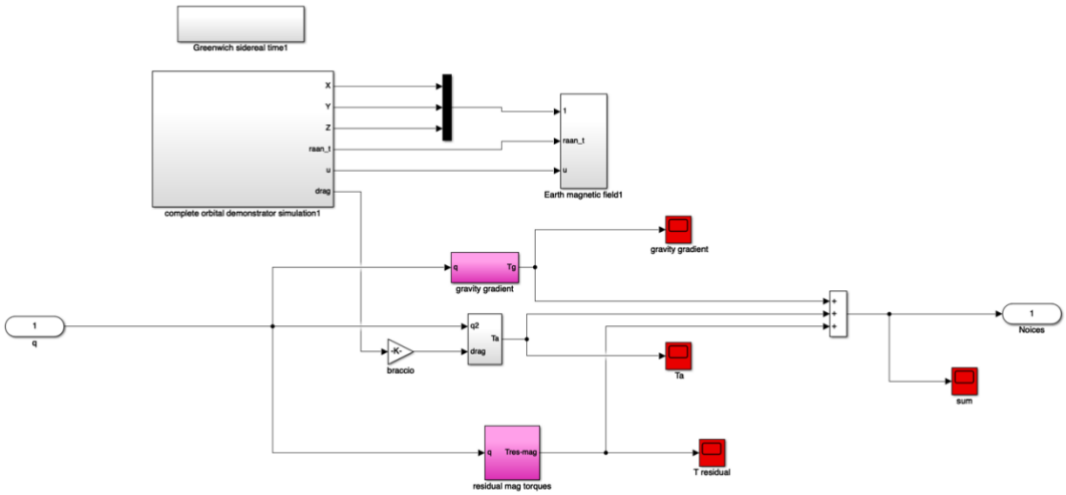


*Figure 24: Noices block content. The three upper gray blocks are used to compute the Earth magnetic field and the drag force used in the computation of the disturbances torque.*

Then, reaction wheels commonly for this class of satellites are exploited to establish the actuation system limits. The maximum torque is introduced by a saturation block imposing an upper and lower bound to the input torque of:

- $u_{max} = 0.05$ [Nm]
- $u_{min} = -0.05$ [Nm]

Moreover, the actuator's uncertainty (due to numerical approximation and measure uncertainty) is modeled through a *Band-Limited White Noise block* to generate a continuous normally distributed random signal with the third standard deviation equal to 3% of the input values.

# 4. Control tuning

Now that all the components of the solution are defined, simulations are carried out to find if the control solution can achieve the objective respecting the problem requirements.

To ensure the best control solution the chosen control law is tuned using an increasingly complex model, the controller tuning takes place in multiple steps:

1. First, the best-fitting solution is derived by tuning the controller in a trial-and-error procedure with the ideal model. If the solution is not able to fulfill the problem conditions another control law must be selected.
2. Then the performance is tested using the more realistic model, and if needed another trial-and-error procedure takes place to improve the controller performance. Again, if the solution is not able to fulfill the problem conditions another controller must be selected, and the procedure repeated from the first step.
3. Lastly, the control solution is deeper analyzed with simulation techniques in chapter 5. Although in this step the controller is no more subject to tuning, if the solution is not able to fulfill the problem conditions another controller must be selected, and the procedure repeated from the first step.

## 4.1 Ideal condition simulation

The aim of the control System tuning involves changing the controller parameters to best serve the remaining criteria as well as the must-have requirements (design constraints). In this work, the main requirement is to keep the steady-state tracking error at a reasonably low level while minimizing the input activities that have a strict limit in intensity.

As for most controller, the control tuning parameters manage the trade-off between the system input activities, the overshoot, and the tracking error performance. In this specific case, the SMC's parameters are $k_1$, $k_2$, and $\eta$; $k_1$ and $\eta$ (which tunes the slope of the attractive term) calibrate the input activities and the overshoots while $k_2$ regulates the tracking error magnitude. If the parameters are not properly tuned a chattering phenomenon is generally notable.

To find the best control law parameters, a trial-and-error procedure is employed in both the following simulations. In the first simulation, the parameters are tuned simulating without any source of error present in the plant, then a more realistic scenario is used. In this ideal scenario the tuning of the SMC's parameters is carried out considering the main control constraints related to the problem requirements:

- Extended time variance reference orientation.
- It is assumed that the satellite's actuators are reaction wheels with torque bounded between -0.05 Nm and 0.05 Nm. The actuators also impose a rate of change of the body frame angles under 0.04 rad/100ms.
- The absolute error shall be less than 1.2° on each axis for 98% of the problem's time.
- Optimize input activities.

Since the conditions above require opposite tuning setup it is evident that a trade-off between the two sets of constraints is the best choice to reach out all the requirements together. The values chosen after the trial-and-error procedure for the control parameters are $k_1$ =0.6, $k_2$ =0.28, and $\eta$ =0.08, even if there are more sets of parameters that could be used with good performance.

*Ideal simulation*

Simulations initial conditions:

- $\omega_0$ = [0.05; 0.05; 0.05]
- $q_0$ = [ 0.7985; -0.3899; 0.4287; 0.1626].

quaternions plot:

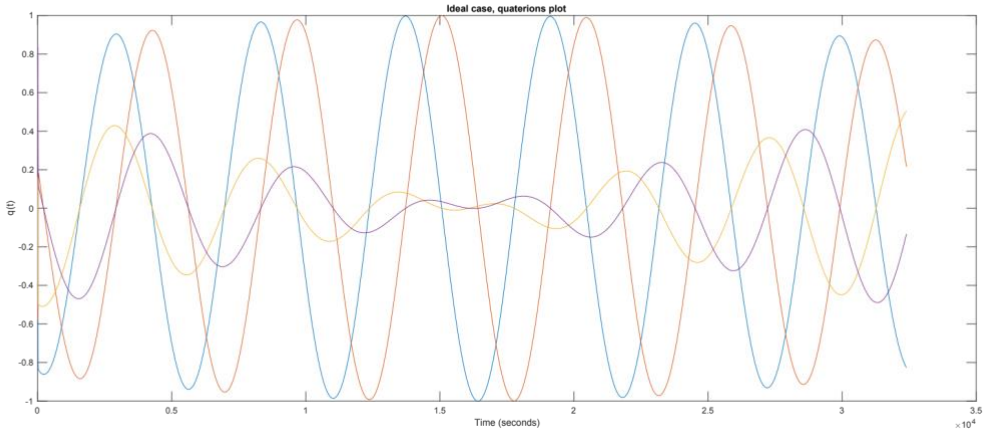


*Figure 25: Ideal Attitude quaternions plot over time.*

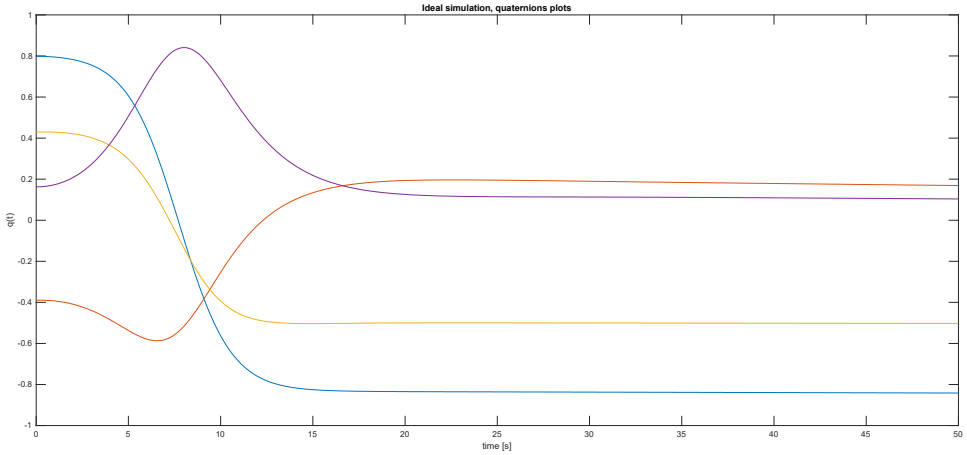


*Figure 26: Ideal Attitude quaternions plot over time (close-up view).*

q tilde plot:

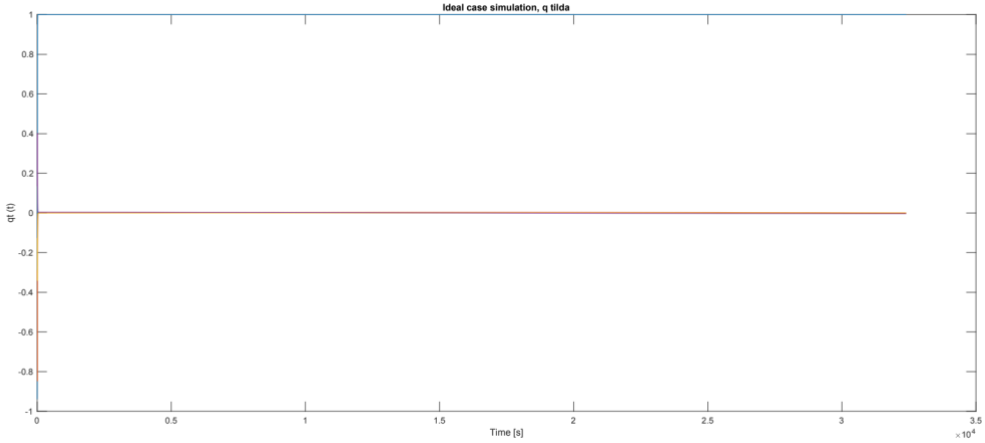


*Figure 27: Ideal q_t plot over time.*

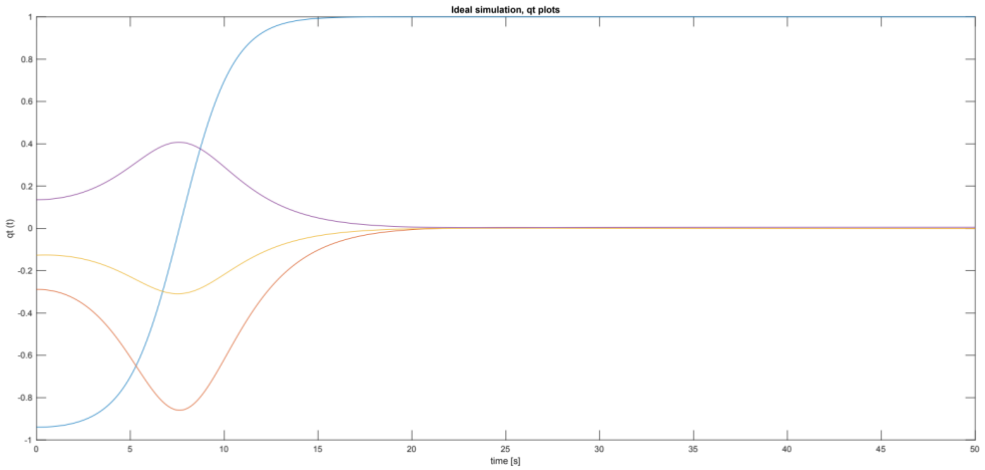


*Figure 28: Ideal q_t plot over time.*

Angular velocity plot:

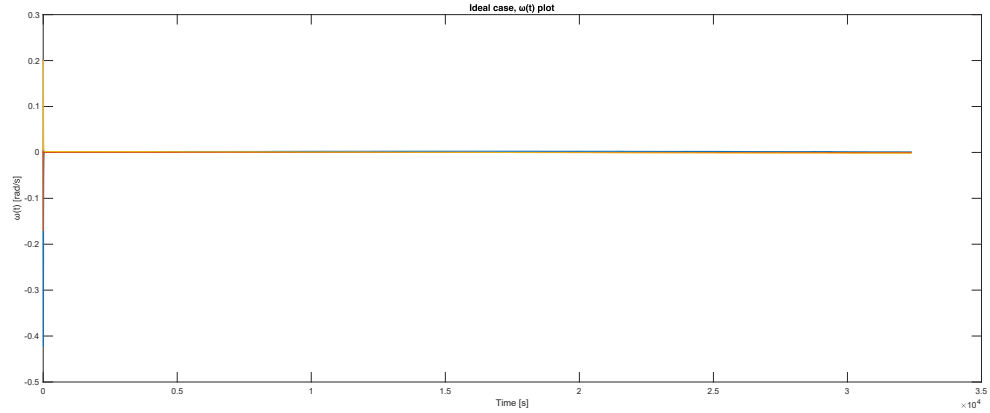


*Figure 29: Ideal angular velocity $\omega(t)$ plot over time*

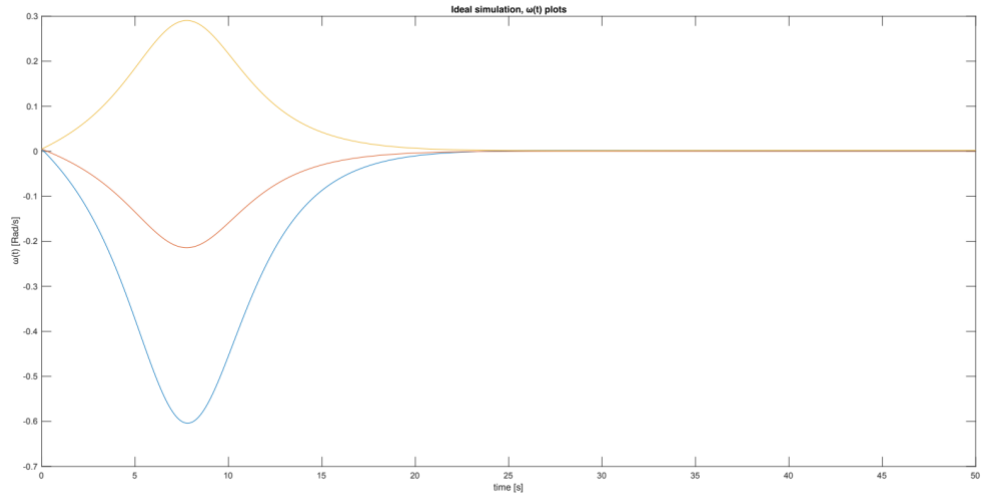


*Figure 30: Ideal angular velocity plot over time (close-up view).*

Input plot:

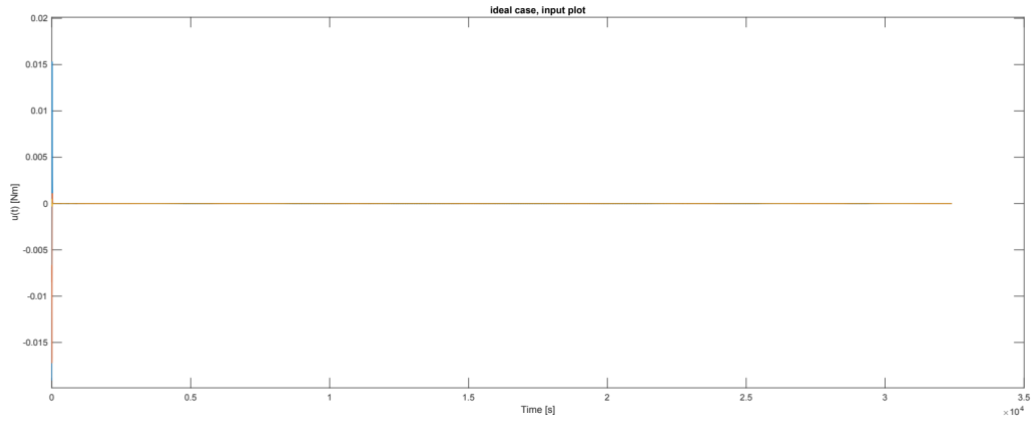


*Figure 31: Ideal input u over time.*

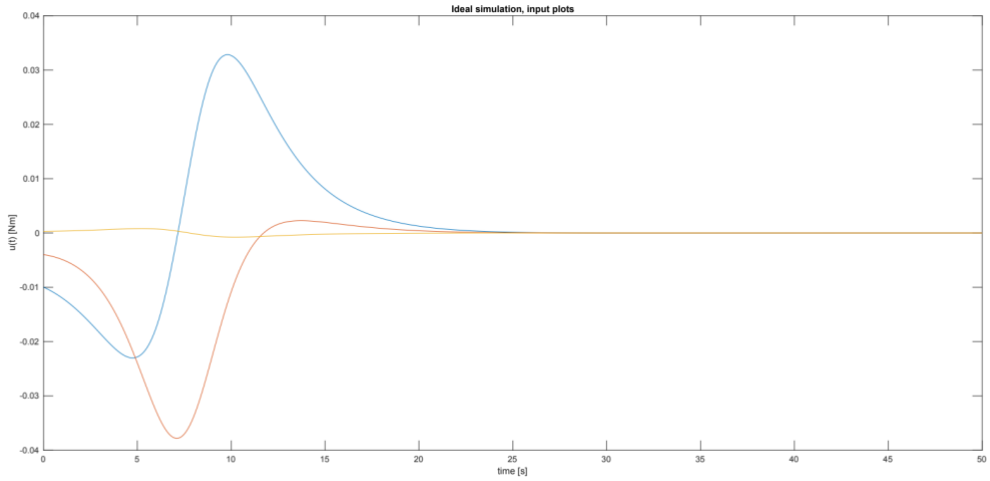


*Figure 32: Ideal input u plot over time (close-up view)*

In this first simulation, the plant performs well in both transient and steady state. The stress on the input activities to keep the error low is minimal. The controller parameters are tuned finding a trade-off between the required input activity and the accuracy during the maneuver.

## 4.2 Results from nominal scenario

This simulation is done using the more realistic model devised at the end of chapter 3. Again, a trial-and-error procedure is done to improve the velocity behavior and the error performance while avoiding the chattering phenomenon.

The adjusted parameters are $k_1 = 1.5$, $k_2 = 1$ and $\eta = 0.1$

Nominal simulations

Simulations initial conditions:

- $\omega_0 = [0.05; 0.05; 0.05]$
- $q_0 = [\ 0.7985; -0.3899; 0.4287; 0.1626]$.

q(t) plots:

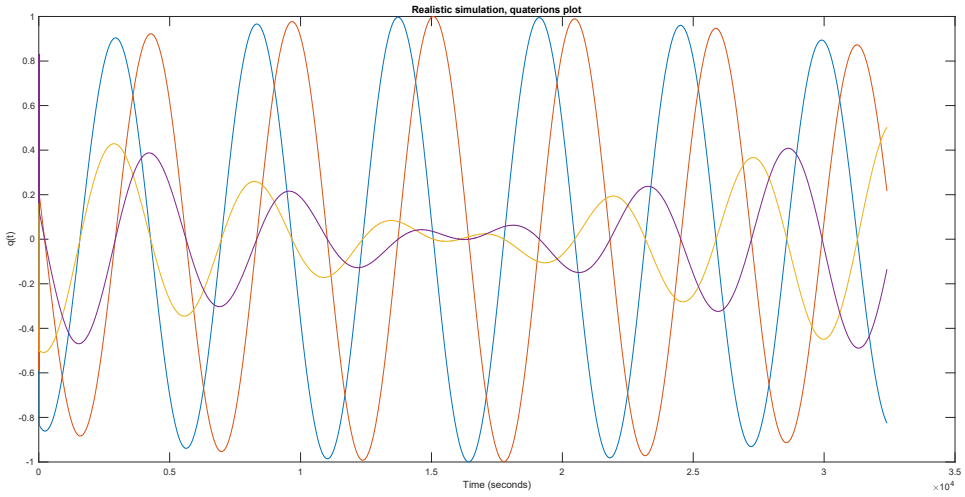


*Figure 33: Real case Attitude quaternions plot over time.*

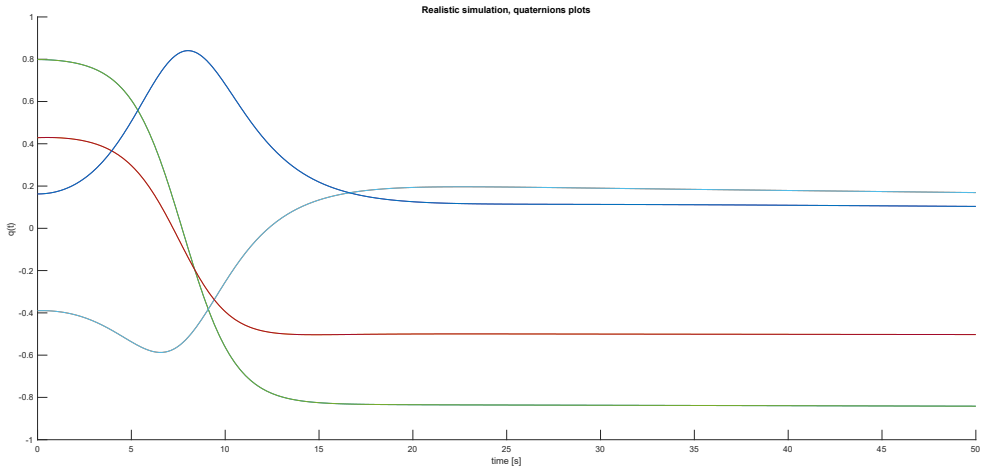


*Figure 34: Real case attitude quaternions plot over time (close-up view).*

q_tilde plots:

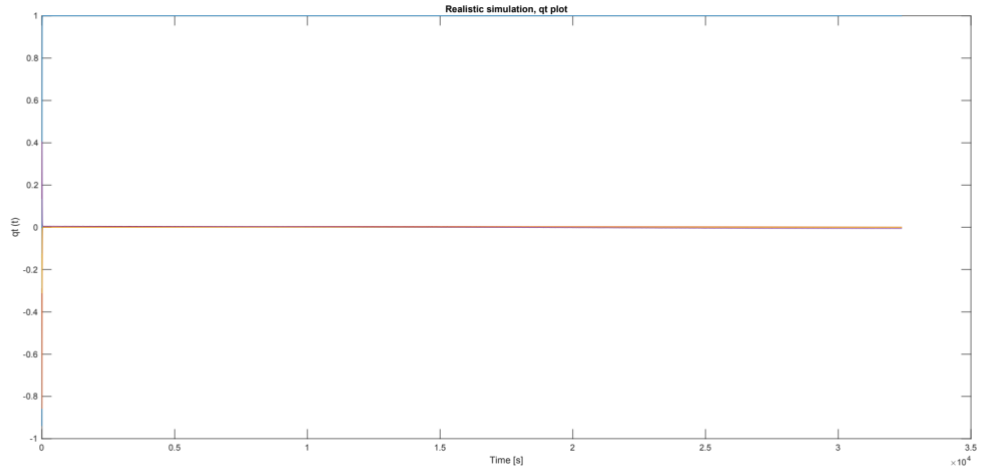


*Figure 35: Real case q_t plot over time.*

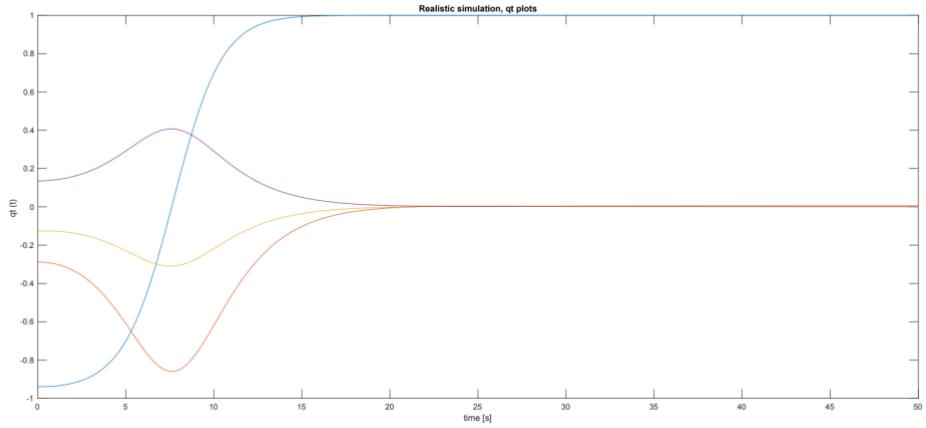


*Figure 36: Real case q_t plot over time (close-up view).*

## Angular velocity plots:

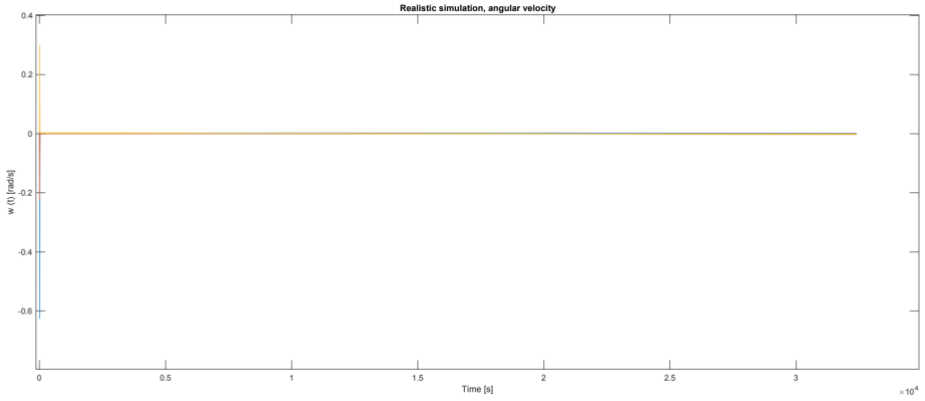


*Figure 37: Real case angular velocity plot over time.*

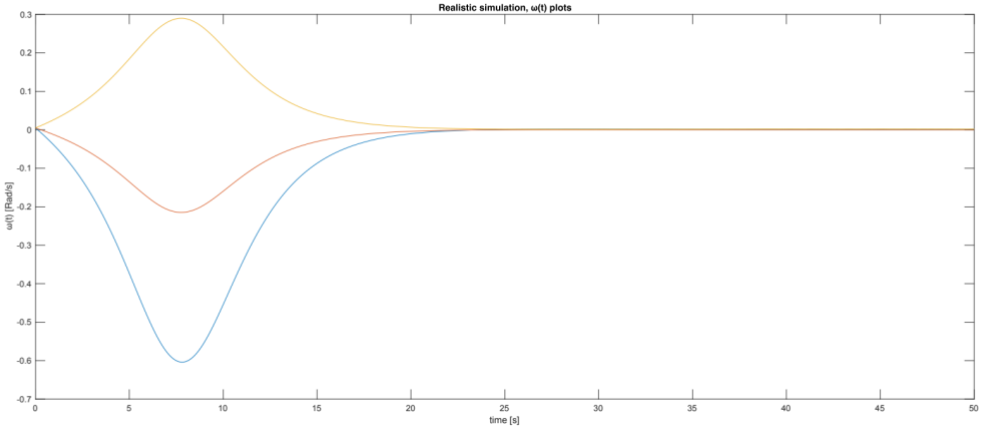


*Figure 38: Real case angular velocity plot over time (transient).*

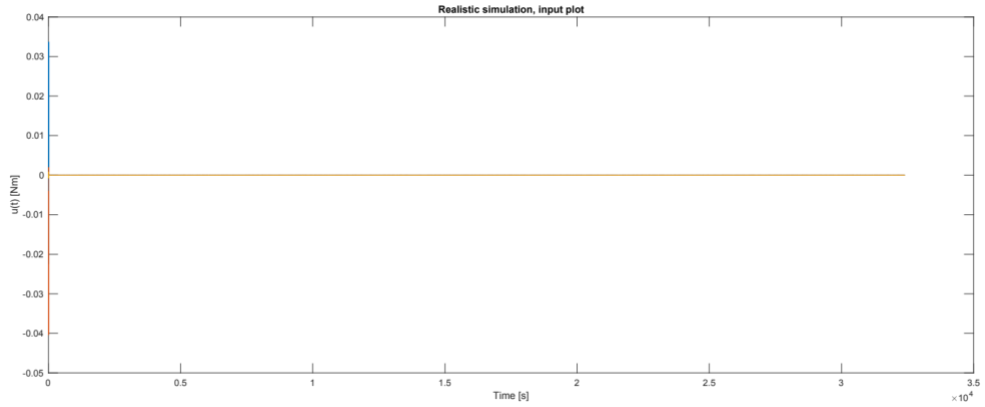


*Figure 39: Real case input u over time.*

Input u plot:

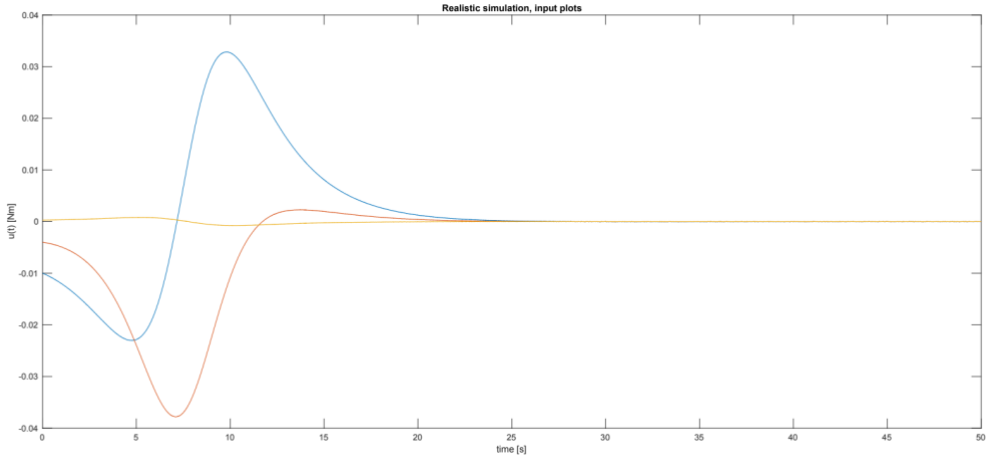


*Figure 40: Real case input u plot over time (transient)*

It is easy to see from *Figure 33* that the controls rapidly lead the quaternions to reference and keep them until the end of the simulation. The quaternions an undershoot on $q_2$ and an overshoot on $q_4$ without any post-transition oscillatory effect, as display in *Figure 34*. Stabilization is achieved within short time as shown in *Figure 34* and confirmed by the plot of $q_t$ in *Figure 35* and *Figure 36.*

In *Figure 38* the angular velocity starts with high values on the x-axis and y-axis, in order to set the satellite orientation on the initial reference attitude. Then the velocity decreases to match the reference values until the end of the simulation, as shown in *Figure 37.*

As for the angular velocity, the control inputs start with a strong initial response to rapidly set the initial system orientation, as shown in *Figure 40*. The SMC has an excellent time response to set the system on reference and keeps it stable until the end of the simulation as is noticeable in *Figure 39*. The input activities do not converge to zero but stay bounded between 9e-7 Nm and -9e-7 Nm over all the steady state.

| Nominal simulations | Input Activities | | Pointing Error | |
|---|---|---|---|---|
| | u max | u min | APE | MPE |
| 2 turn simulation | 0.0403 Nm | 4,29E-11 Nm | 4.5% | 6.8% |
| 4 turn simulation | 0.0403 Nm | 1,36E-12 Nm | 7.3% | 8% |
| 6 turn simulation | 0.0403 Nm | 1.82e-12 Nm | 6% | 7.4% |

N.B.
The performance values of the attitude error are computed over the simulation time excluded the transient, which is less than the 0.02% of the simulation time.

In these simulations, the constraints on the input activities are respected, while the performance at steady state follows the requirements with an absolute error below 1° on each axis and the APE and MPE below 10%, as shown in the table above.

# 5. Analysis

To test the performance of the designed control solution, two set of simulations campaign are done:

- A first *worst cases analysis* is performed to verify the system ability in handling uncertainties.
- A *Monte Carlo campaign* is carried out to evaluate the robustness of the control solution, evaluating the outcomes of a wide range of unknown initial condition, reflecting possible design errors.

## 5.1 Worst cases analysis

System uncertainties are introduced between the model and the controller parameters *m*, *w0* and *q0* to evaluate the control response to uncertainties. The performance of this analysis is used to evaluate if the control solution is suited to carry out a robustness campaign. The first analysis consists of 12 simulations split into 4 steps, each featuring given uncertainties with predefine magnitude. The chosen organization of the uncertainties in every step is described below:

Nominal initial conditions:

- $\omega_0$ = [0.05; 0.05; 0.05]
- $q_0$ = [ 0.7985; -0.3899; 0.4287; 0.1626].
- $m_c$ = 20 kg

Each *step* of the worst-case analysis consists of:

- A simulation over 2 turns of the helix trajectory (one-third of the mission time).
- A simulation over 4 turns of the helix trajectory (two-thirds of the mission time).
- A simulation over 6 turns of the helix trajectory (full mission time).

Uncertainties set up for every *step*:

**Step 1**, Mass uncertainty simulations:

- An uncertainty of amplitude **2 kg** is introduced on the mass.

**Step 2**, Initial position uncertainty simulations:

- An uncertainty of amplitude **10°** is introduced on the initial attitude angles, which is then converted into quaternion representation and applied to the attitude quaternion.

**Step 3**, Initial angular velocity uncertainty simulations:

- An uncertainty of amplitude **0.02 rad/s** is introduced on the angular velocity.

**Step 4**, All uncertainties simulations:

- An uncertainty of amplitude **2 kg** is introduced on the mass.
- An uncertainty of amplitude **10°** is introduced on the initial attitude angles, which is then converted into quaternion representation and applied to the attitude quaternion
- An uncertainty of amplitude **0.02 rad/s** is introduced on the angular velocity.

### 5.1.1 Mass uncertainty simulations

Step 1, *Mass uncertainties simulations*:

- A mass uncertainty of *2 kg* is introduced on the mass, which entails a change in J.

*Mass uncertainty simulation over 2 turns*

Quaternions plot:

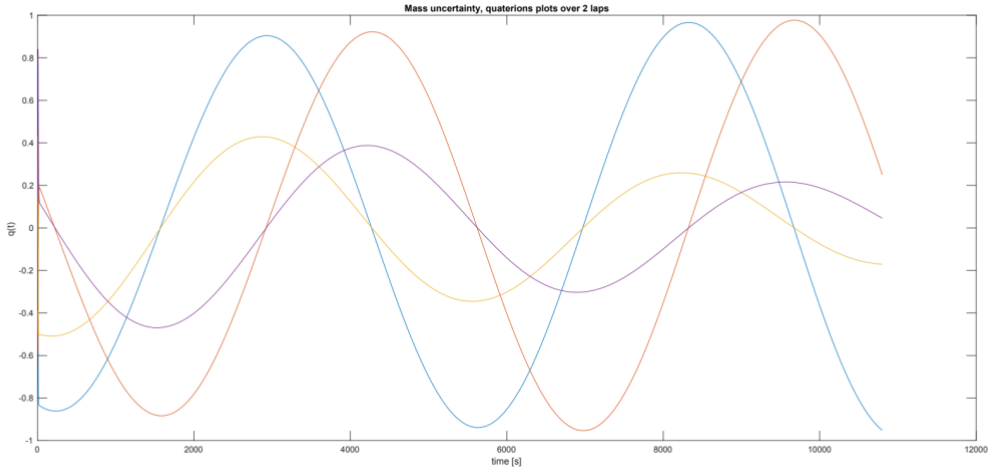


*Figure 41: Mass uncertainties simulation, attitude quaternions plot over 2 turns period.*

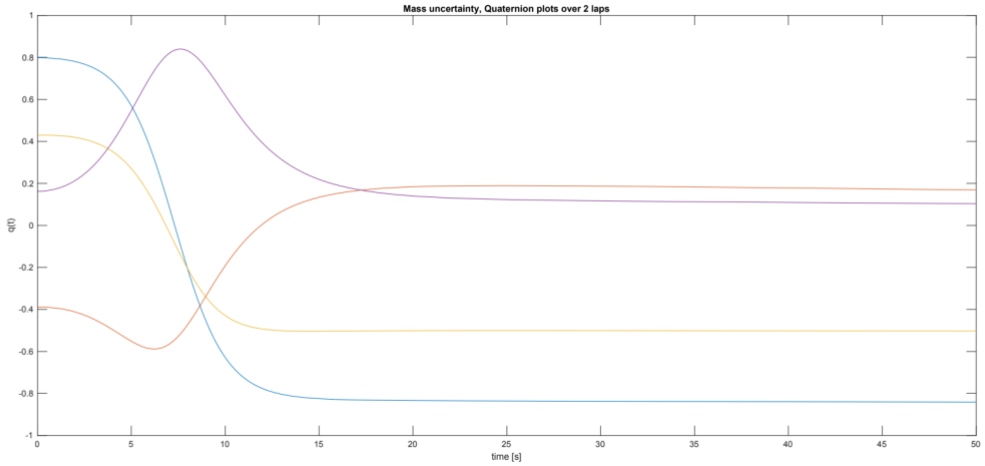


*Figure 42: Mass uncertainties simulation, attitude quaternions close view 2 turns plot*

Angular velocity ω(t) plot:

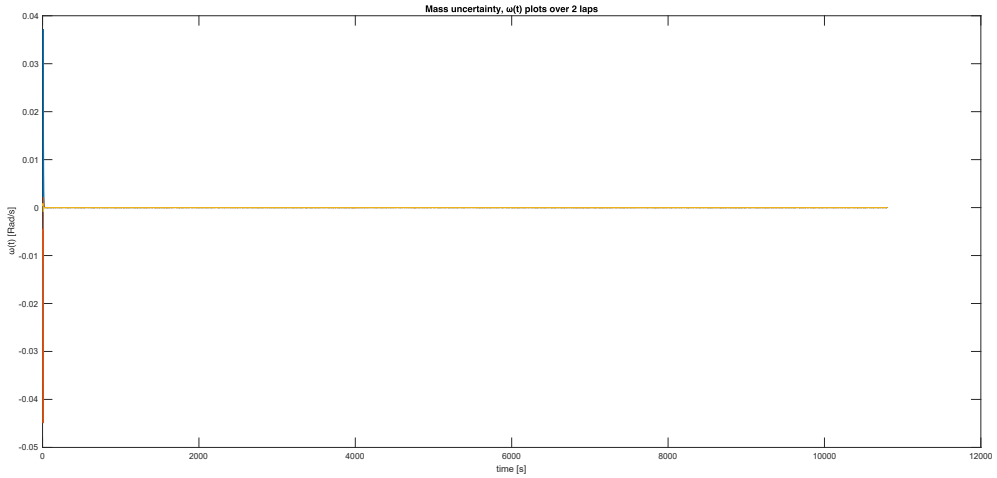


*Figure 43: Mass uncertainties simulation, angular velocity plot over 2 turns period.*

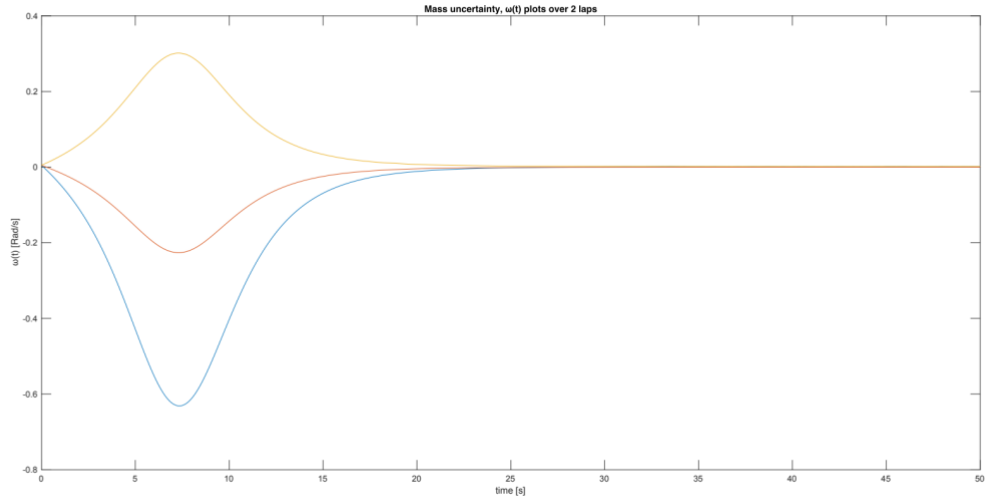


*Figure 44: Mass uncertainties simulation, angular velocity close view 2 turns plot*

Input u plot:

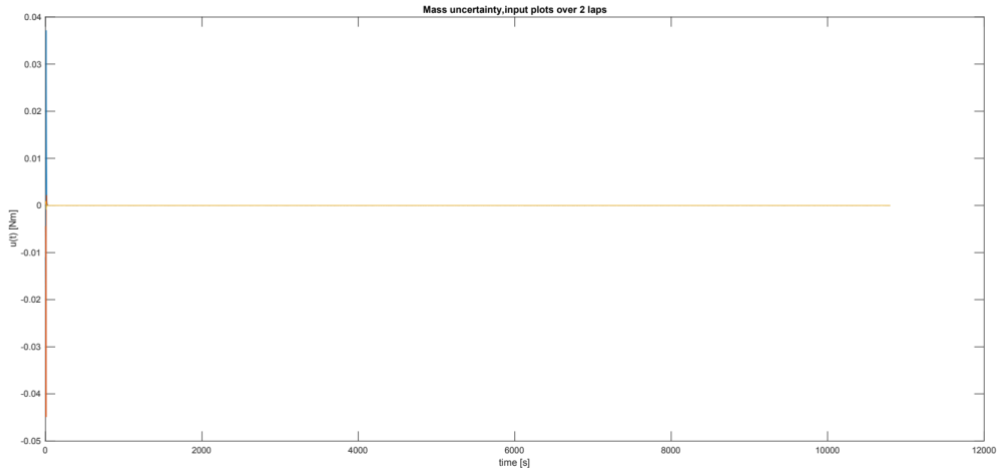


*Figure 45: Mass uncertainties simulation, input u(t) plot over 2 turns period.*

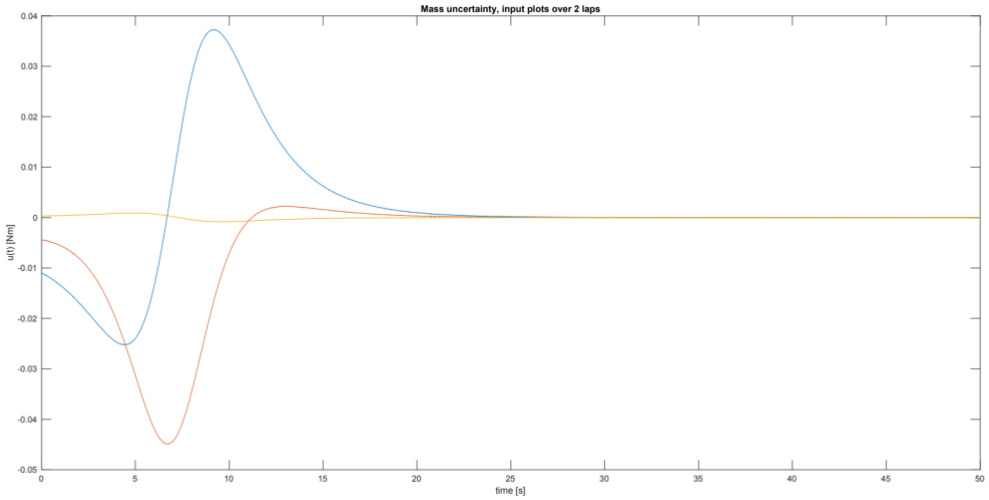


*Figure 46: Mass uncertainties simulation, input u(t) close view 2 turns plot*

In *Figure 41* the quaternions go to reference in less than 30 seconds and display an undershoot on $q_2$ and an overshoot on $q_4$. Then the quaternions follow the reference up to the end of the 2-turn simulation, as displayed in *Figure 42*.

From *Figure 45* it can be seen a strong input response within the transient, while *Figure 46* shows that the input activities stay bound between 9e-7 Nm and -3e-7 Nm in the steady state.

*Figure 44* shows high angular velocity during the transient, since the system orientation is on track of the reference attitude, then the values decrease to reference and stay bound until the end of the simulation, as shown in *Figure 43*. No chattering is visible.

The intense activity of both the angular velocity and the input is to reach the operational initial attitude in a short time. Once the operational orientation is reached the input must keep the quaternions and angular velocity bounded on reference for the whole simulation.

*Mass uncertainty simulation over 4 turns*

Quaternions plot:

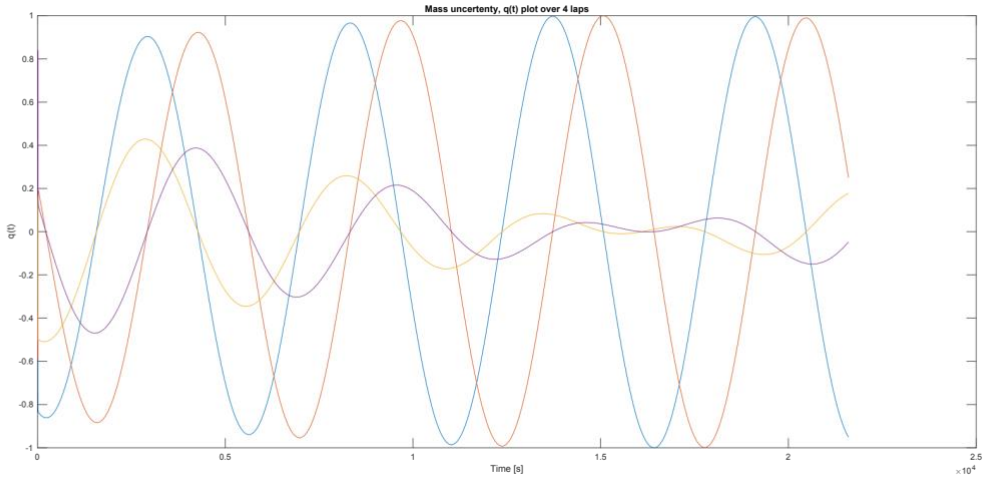


*Figure 47: Mass uncertainties simulation, attitude quaternions plot over 4 turns period.*

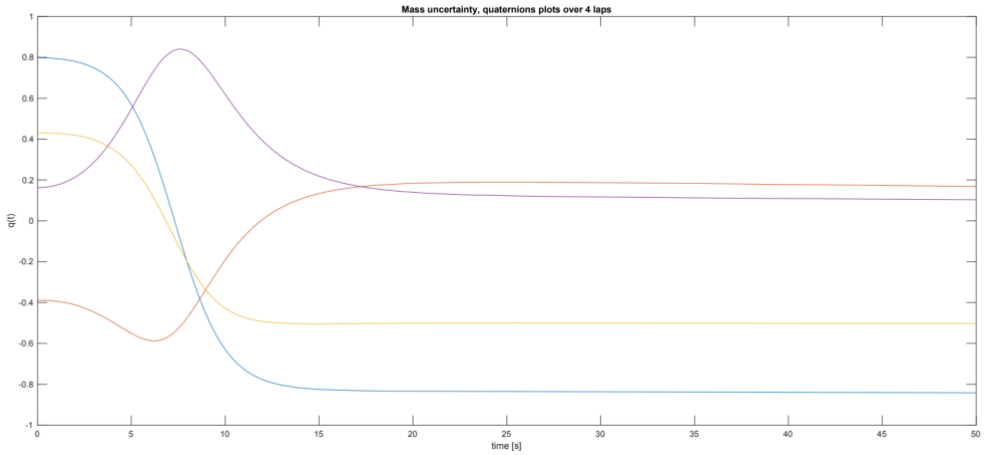


*Figure 48: Mass uncertainties simulation, attitude quaternions close view 4 turns plot*

Angular velocity plot:

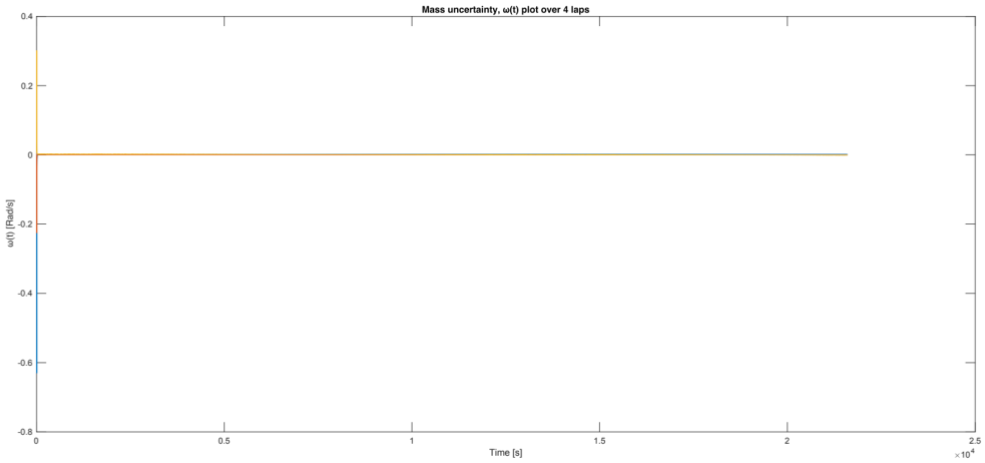


*Figure 49: Mass uncertainties simulation, angular velocity plot over 4 turns period.*

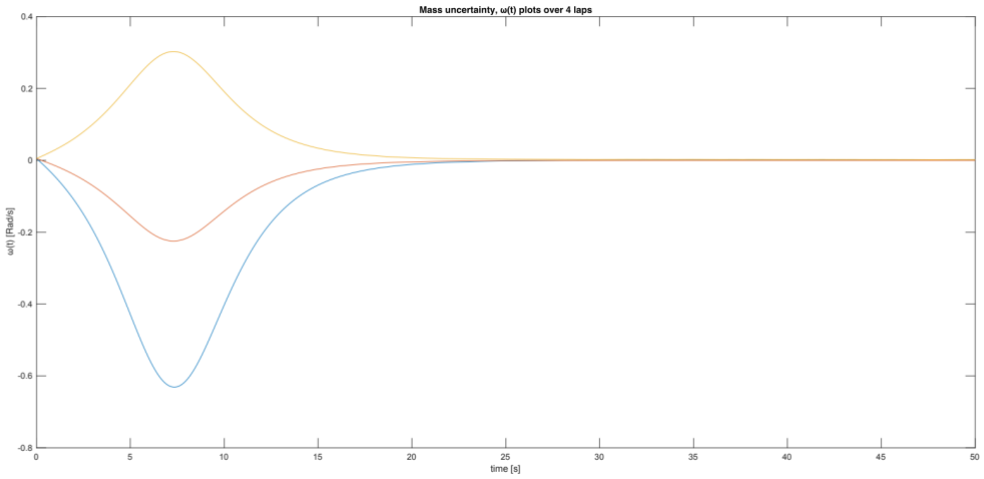


*Figure 50: Mass uncertainties simulation, angular velocity close view 4 turns plot*

Input u plots:

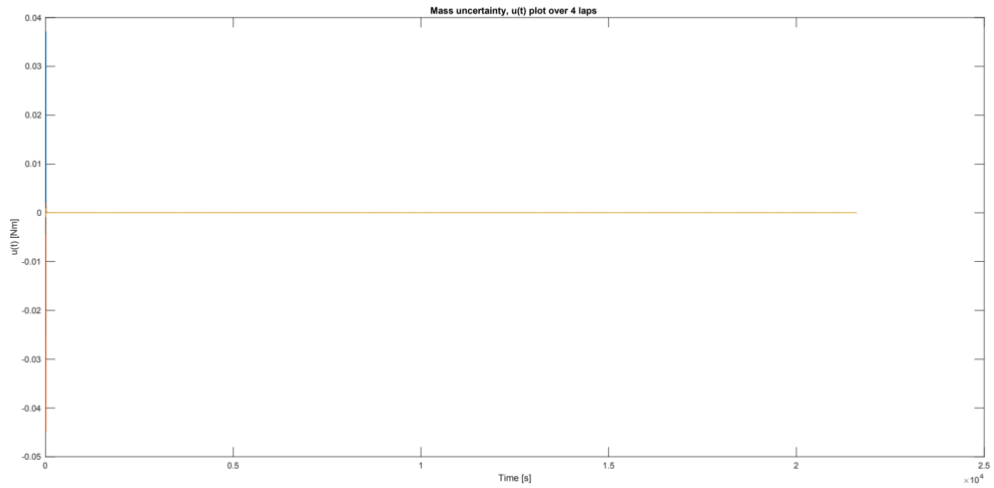


*Figure 51: Mass uncertainties simulation, input u(t) plot over 4 turns period.*

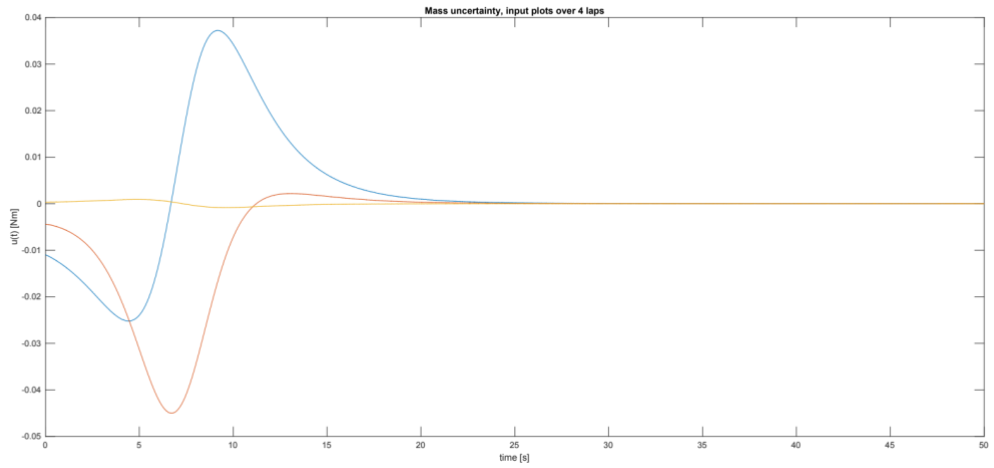


*Figure 52: Mass uncertainties simulation, input u(t) close view 4 turns plot*

In *Figure 47* the quaternions go to reference in less than 30 seconds and display an undershoot on $q_2$ and an overshoot on $q_4$. Then the quaternions follow the reference until the end of the 4-turn simulation, as displayed in *Figure 48*. In *Figure 50* the angular velocity starts strong, to set the system orientation on the initial operational attitude, then the values decrease to reference and stay bound until the end of the simulation, as shown in *Figure 49*. No chattering is visible.

As for the angular velocity, the control inputs start with a strong initial response to rapidly set the initial system orientation, as shown in *Figure 52*. The controller has an excellent time response to set the system on reference and keeps it stable until the end of the simulation as is evident in *Figure 51*. The input activities do not converge to zero but stay bounded between 9e-7 Nm and -7e-7 Nm over all the steady state.

*Mass uncertainty simulation over 6 turns*

Quaternions plot:

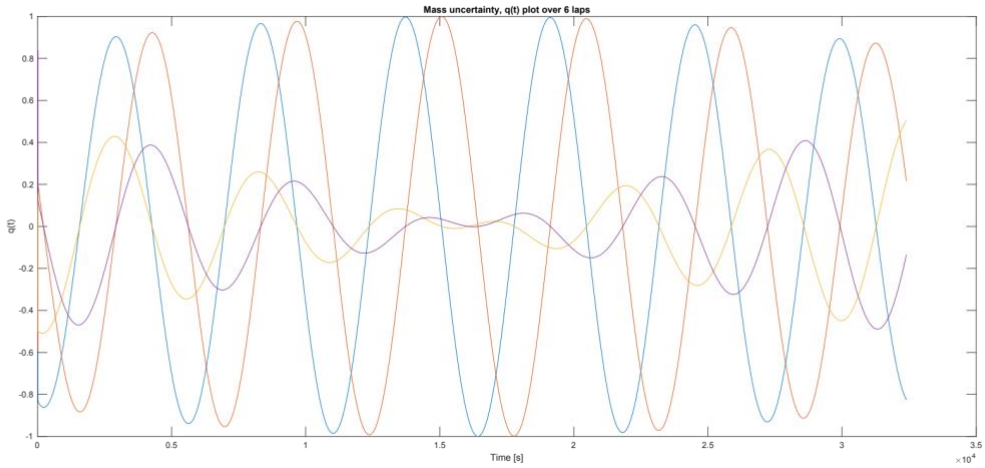


*Figure 53: Mass uncertainties simulation, attitude quaternions plot over 6 turns period.*

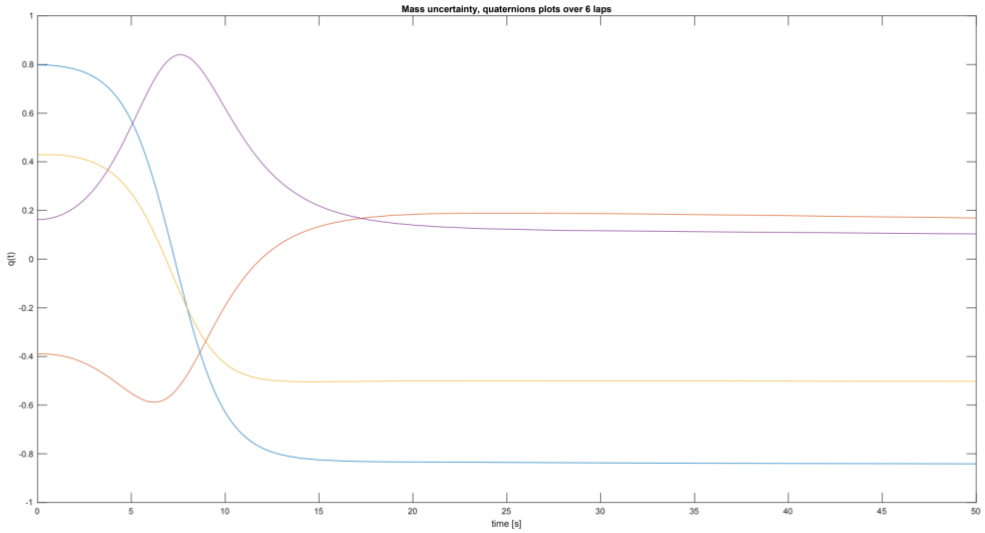


*Figure 54: Mass uncertainties simulation, attitude quaternions close view 6 turns plot*

Angular velocity ω(t) plot:

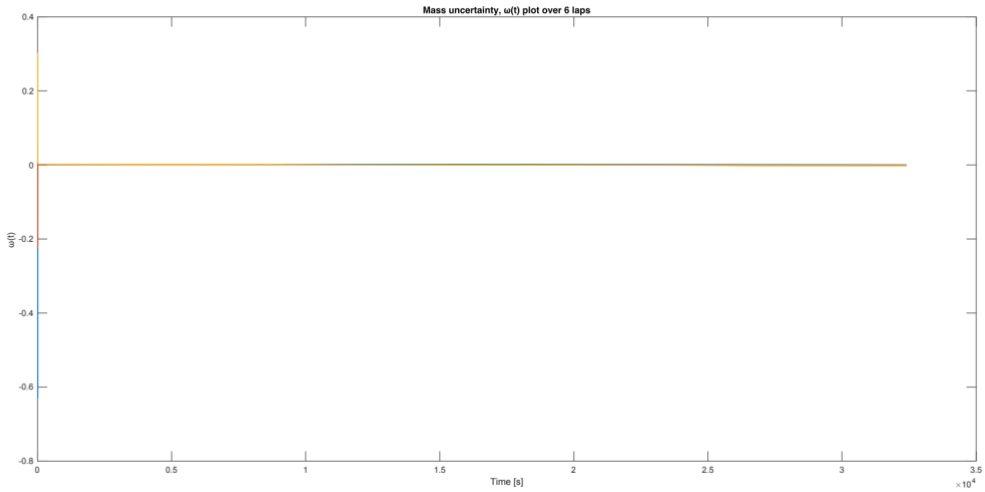


*Figure 55: Mass uncertainties simulation, angular velocity plot over 6 turns period.*

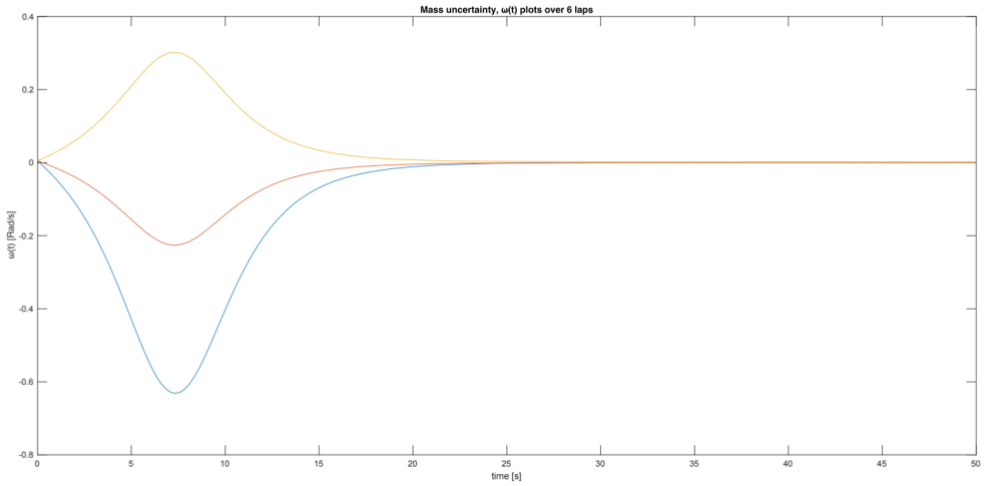


*Figure 56: Mass uncertainties simulation, angular velocity close view 6 turns plot*

Input u plot:

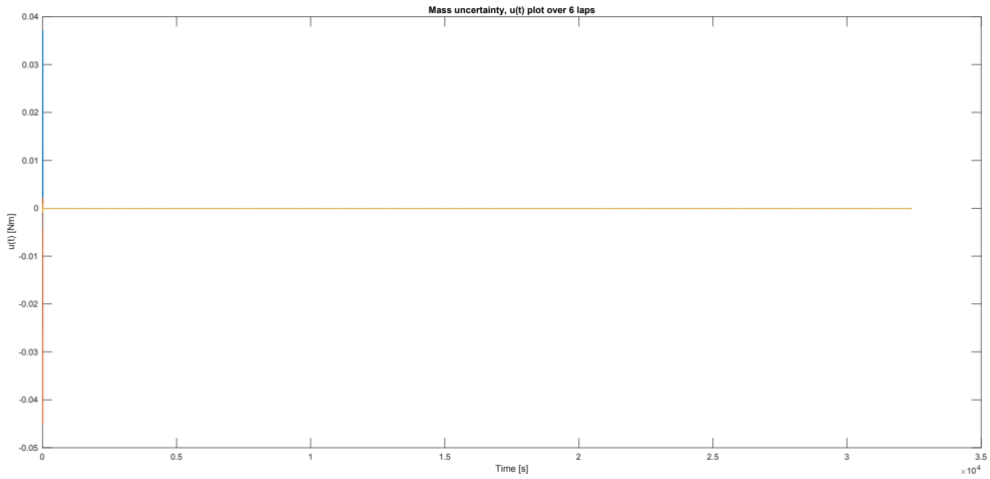


*Figure 57: Mass uncertainties simulation, input u(t) plot over 6 turns period.*

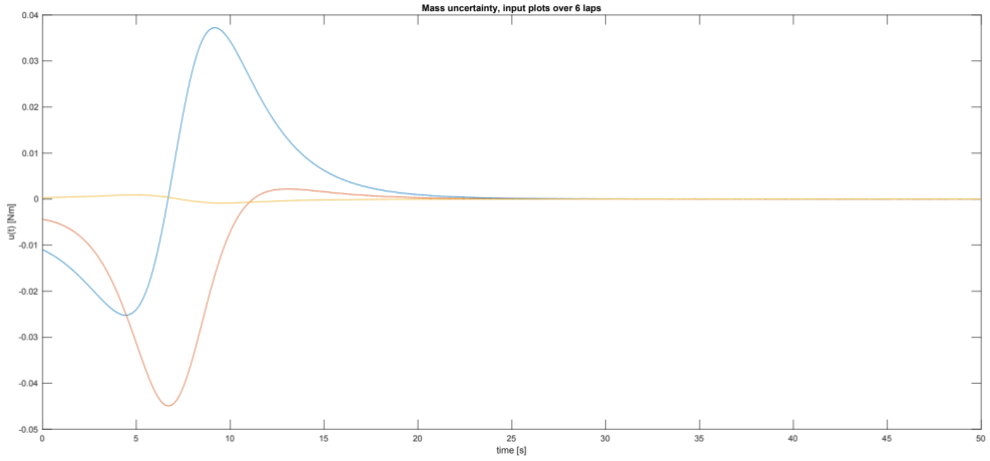


*Figure 58: Mass uncertainties simulation, input u(t) close view 6 turns plot*

In *Figure 53* the quaternions go to reference in less than 30 seconds and display an undershoot on $q_2$ and an overshoot on $q_4$. Then the quaternions follow the reference up to the end of the 6-turn simulation, as displayed in *Figure 54*.

In *Figure 56* the angular velocity starts strong, to set the system orientation on the initial operational attitude, then the values decrease to reference and stay bound until the end of the simulation, as shown in *Figure 55*. No chattering is visible.

As for the angular velocity, the control inputs start with a strong initial response to rapidly set the initial system orientation, as shown in *Figure 57*. The SMC has an excellent time response to set the system on reference and keeps it stable until the end of the simulation as is evident in *Figure 58*. The input activities do not converge to zero but stay bounded between 9e-7 Nm and -9e-7 Nm over all the steady state.

| Step1, Mass uncertenty simulations | Input Activities | | Pointing Error | |
|---|---|---|---|---|
| | u max | u min | APE | MPE |
| 2-turns simulation | 0,0428 Nm | 6.14e-11 Nm | 4.6% | 6.9% |
| 4-turns simulation | 0,0428 Nm | 1.96e-12 Nm | 7.4% | 8.1% |
| 6-turns simulation | 0,0428 Nm | 2.13e-12 Nm | 6% | 7.4% |

Since the control system can rejects the mass uncertainty. The quaternions are approximately identical to the Nominal case while the input activities and angular velocity have little higher values during the transient to deal with the uncertainty.

The simulations follow the requirements of the problem: the transient does not break the constraints impose by the actuators on the torque while the boresight error, the APE and MPE follow the requisite. As can be seen from the table above, the performance is almost unchanged from the nominal simulations even if the mass uncertainty was introduced. Since both the attitude reference and the angular velocity reference are small the APE and MPE are larger in the middle of the trajectory although the center of the trajectory is where the error on the orientation is lower. The only sections with attitude error larger the 1° are the beginning and the end of the trajectory, although for less than the 1% of the simulations time.

### 5.1.2 Initial attitude $q_0$ uncertainty

Step 2, Initial position uncertainty simulations:

- An uncertainty of 10° is introduced on the initial attitude angles, which is converted in quaternion representation and apply to the attitude quaternion

*$q_0$ uncertainties simulation over 2 turns*

Quaternions plot:

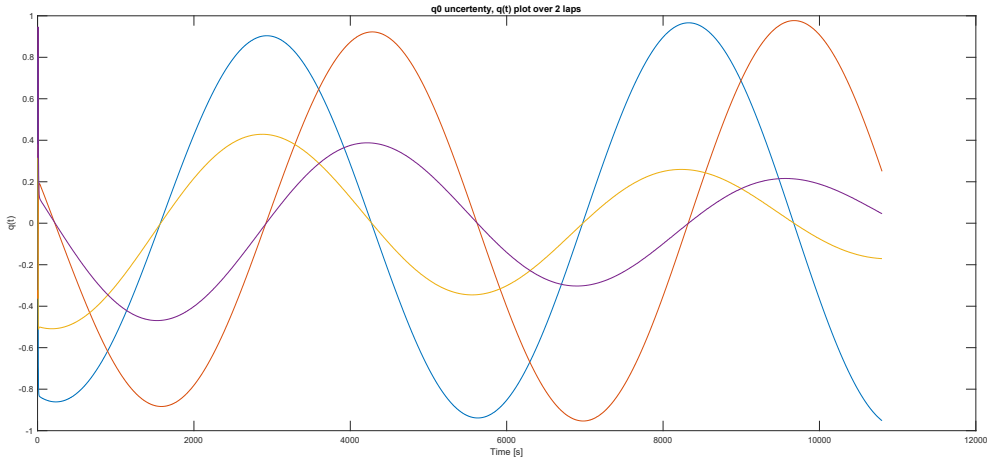


*Figure 59: $q_0$ uncertainties simulation, attitude quaternions plot over 2 turns period.*

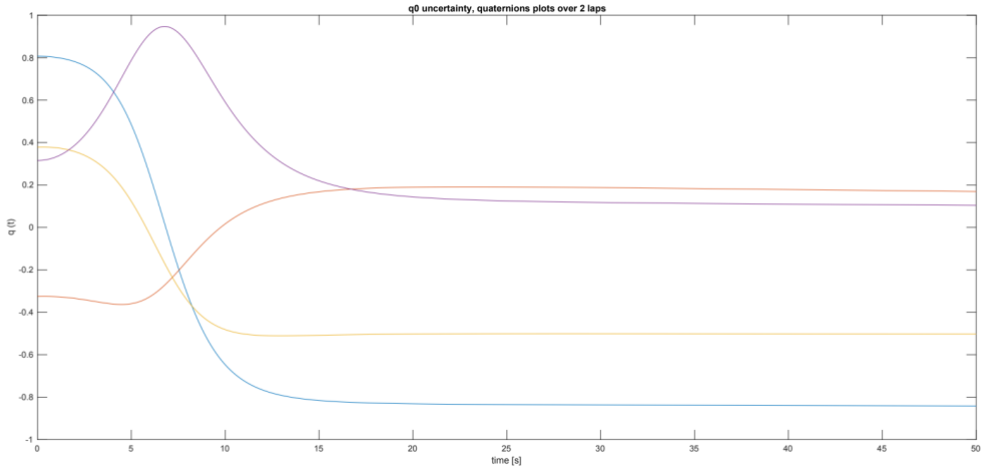


*Figure 60: $q_0$ uncertainties simulation, attitude quaternions close view 2 turns plot*

Angular velocity ω(t) plot:

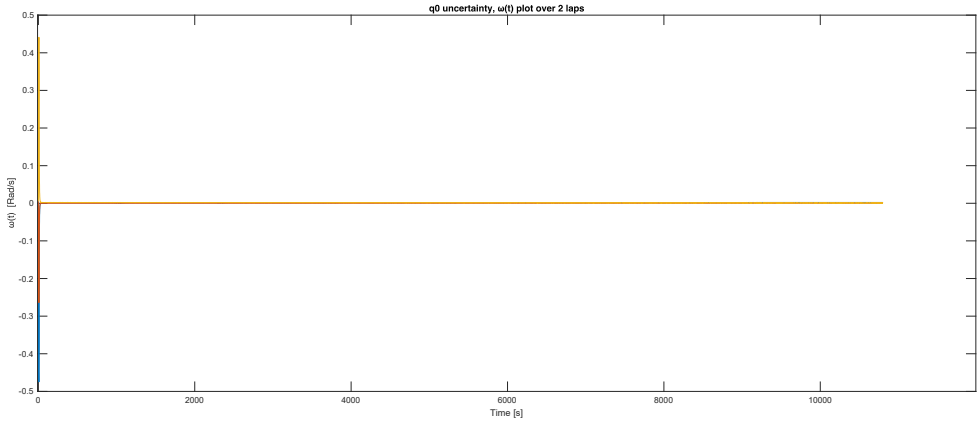


*Figure 61: $q_0$ uncertainties simulation, angular velocity plot over 2 turns period.*

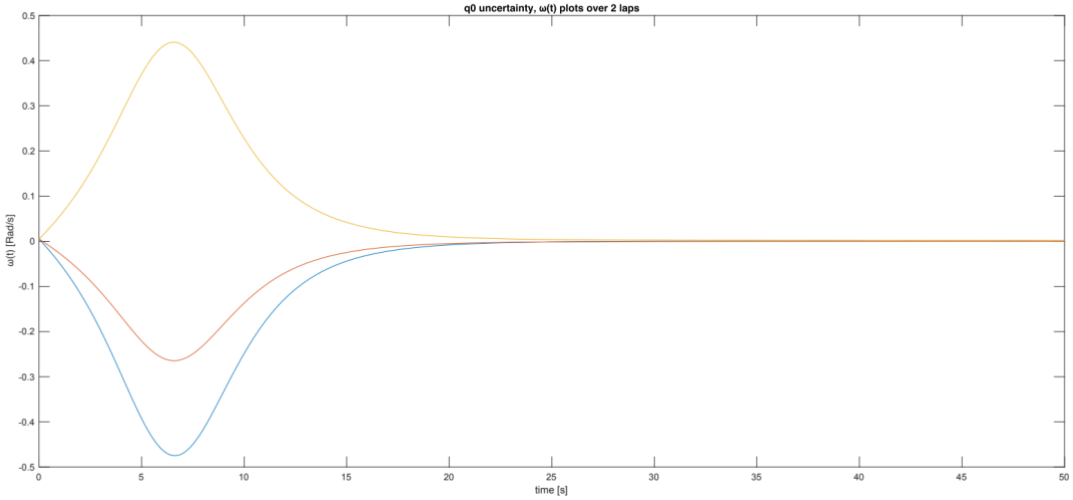


*Figure 62: $q_0$ uncertainties simulation, angular velocity close view 2 turns plot*

Input u plot:

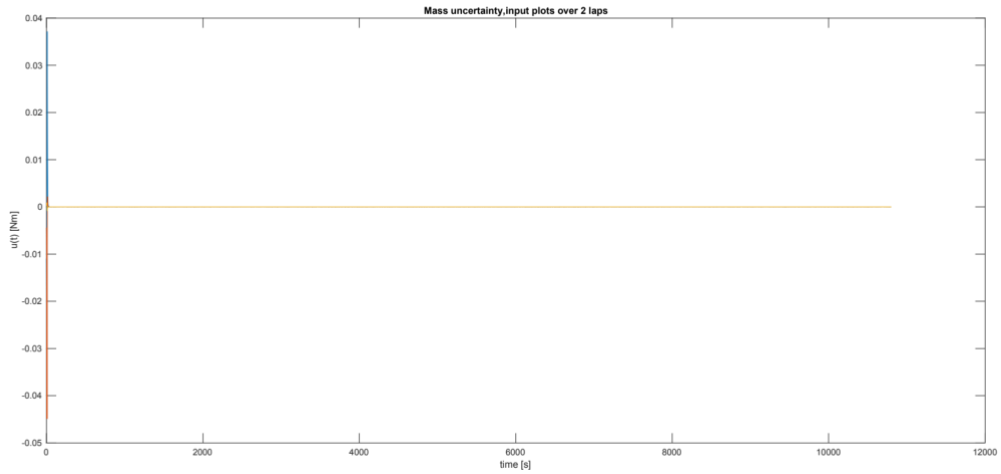


*Figure 63: $q_0$ uncertainties simulation, input u(t) plot over 2 turns period.*

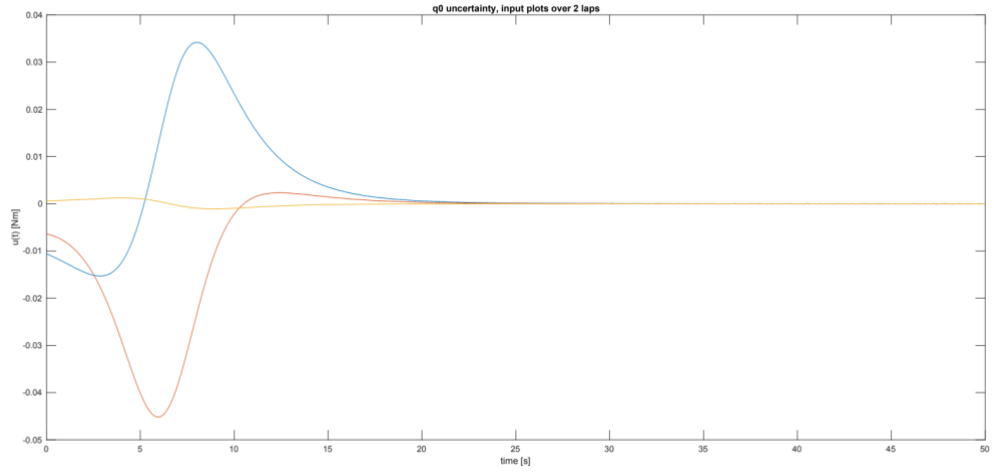


*Figure 64: $q_0$ uncertainties simulation, input u(t) close view 2 turns plot*

Also in this simulation, the quaternions go to reference in less than 30 seconds. Then the quaternions stay on reference for the rest of the 2-turn simulation, as displayed in *Figure 60*.

Due to the uncertainty on the initial position, the undershoot on $q_2$ is lower while the overshoot on $q_4$ is higher than the one in the nominal simulation.

From *Figure 64* it can be seen a strong input response within the transient, while *Figure 63* shows that in the steady state the input activities stay bounded between 9e-7 Nm and -3e-7 Nm.

The intense activity displays in of both the angular velocity and the input are used to reach the operational initial attitude in short time. Once the operational orientation is reached both input and angular velocity rapidly decrease and stabilize until the end of the simulation.

*$q_0$ uncertainty simulation over 4 turns*

Quaternions plot:

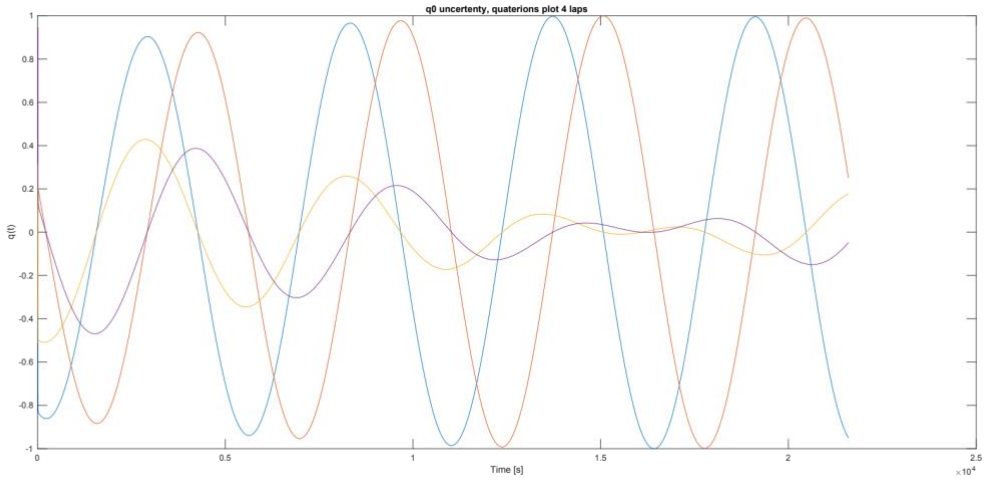


*Figure 65: $q_0$ uncertainties simulation, attitude quaternions plot over 4 turns period.*

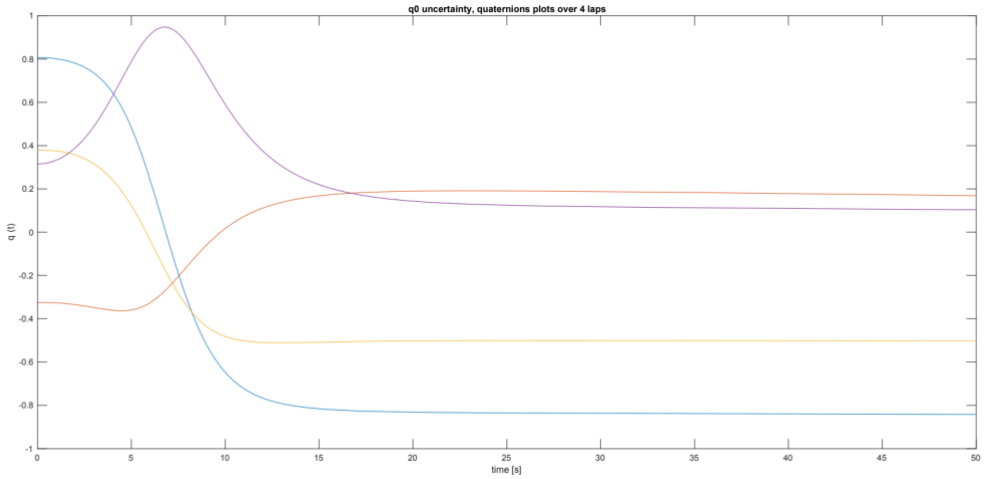


*Figure 66: $q_0$ uncertainties simulation, attitude quaternions close view 4 turns plot*

Angular velocity w(t) plot:

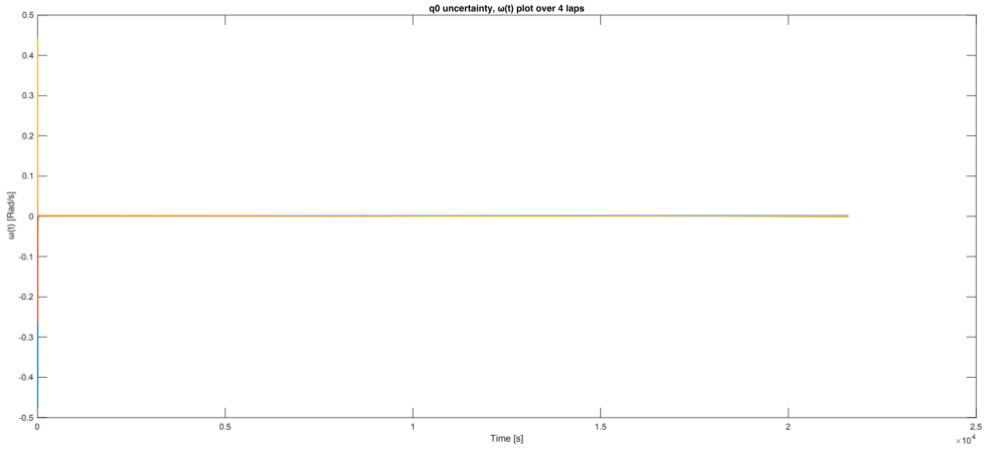


*Figure 67: $q_0$ uncertainties simulation, angular velocity plot over 4 turns period.*

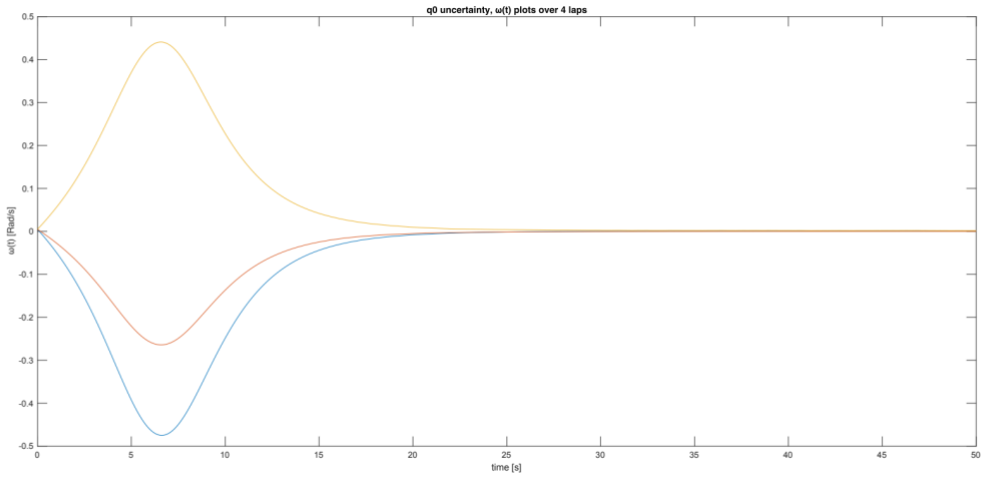


*Figure 68: $q_0$ uncertainties simulation, angular velocity close view 4 turns plot*

Input u plot:

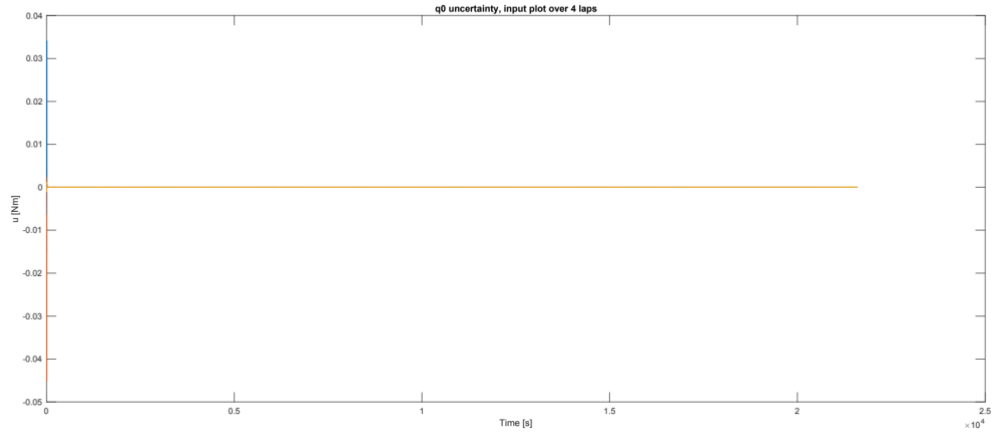


*Figure 69: $q_0$ uncertainties simulation, input u(t) plot over 4 turns period.*

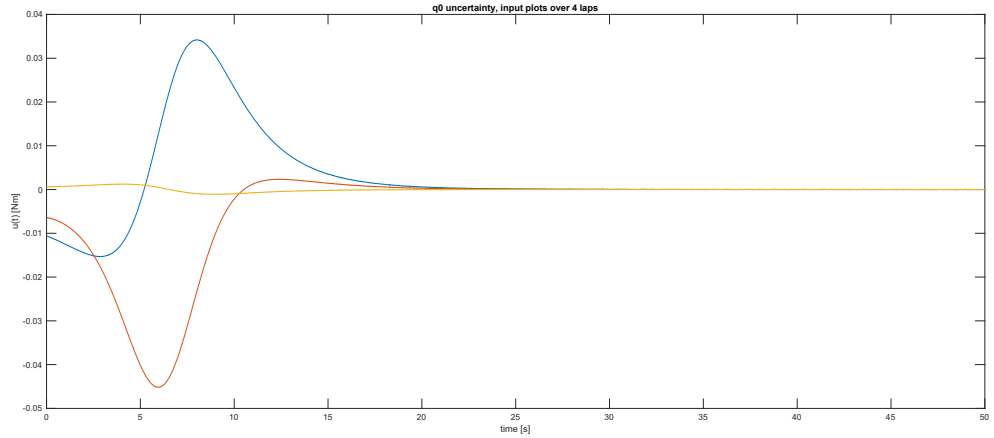


*Figure 70: $q_0$ uncertainties simulation, input u(t) close view 4 turns plot*

Due to the uncertainty on the initial position, the quaternions behavior in the transient has changed a little, the undershoot on $q_2$ is lower while the overshoot on $q_4$ is higher than the one in the nominal simulation. Once in steady state the quaternions follow the reference up to the end of the 4-turn simulation, as displayed in *Figure 66*. As is obvious in *Figure 68*, the angular velocity starts strong to set the system orientation on the initial operational attitude, then the values decrease to reference and stay bound until the end of the simulation, as shown in *Figure 67*. No chattering is visible.

As for the angular velocity, the control inputs start with a strong initial response to rapidly set the initial system orientation, as show in *Figure 70*. After setting the attitude on reference the controller keeps it stable util the end of the simulation, as it is apparent in *Figure 69*. The input activities do not converge to zero but stay bounded between 9e-7 Nm and -7e-7 Nm for all the steady state.

*$q_0$ uncertainty simulation over 6 turns*

Quaternions plot:

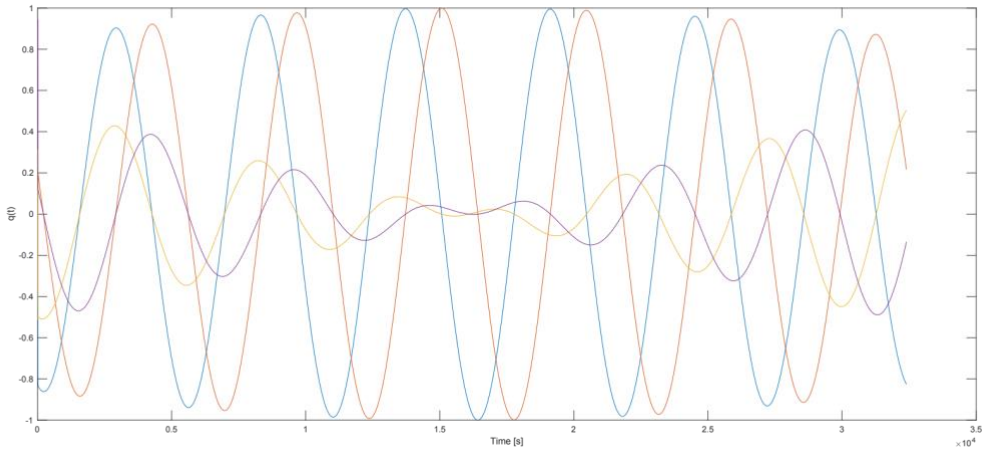


*Figure 71: $q_0$ uncertainties simulation, attitude quaternions plot over 6 turns period. done*

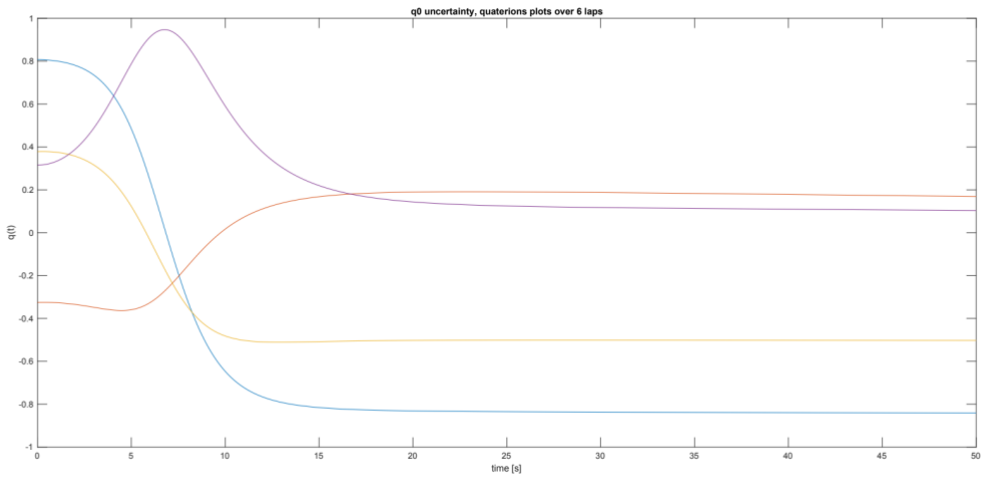


*Figure 72: $q_0$ uncertainties simulation, attitude quaternions close view 6 turns plot*

Angular velocity w(t) plot:

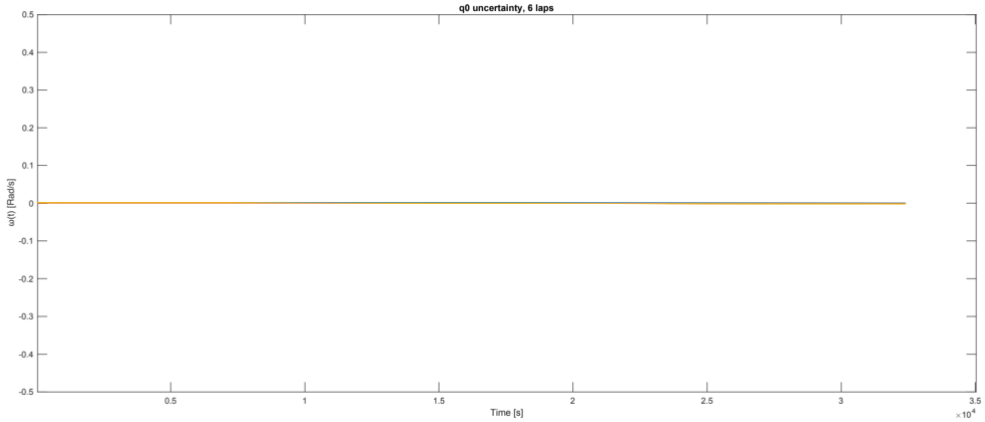


*Figure 73: $q_0$ uncertainties simulation, angular velocity plot over 6 turns period.*

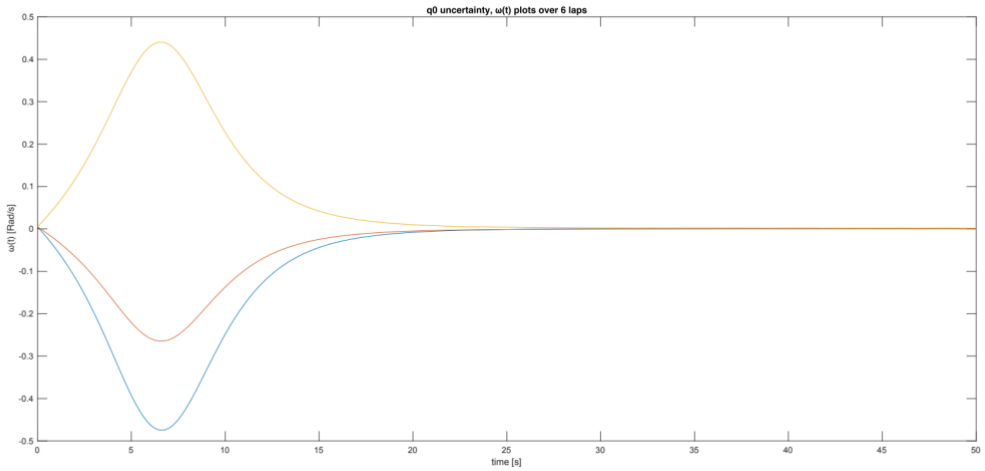


*Figure 74: $q_0$ uncertainties simulation, angular velocity close view 6 turns plot*

Input u plot:

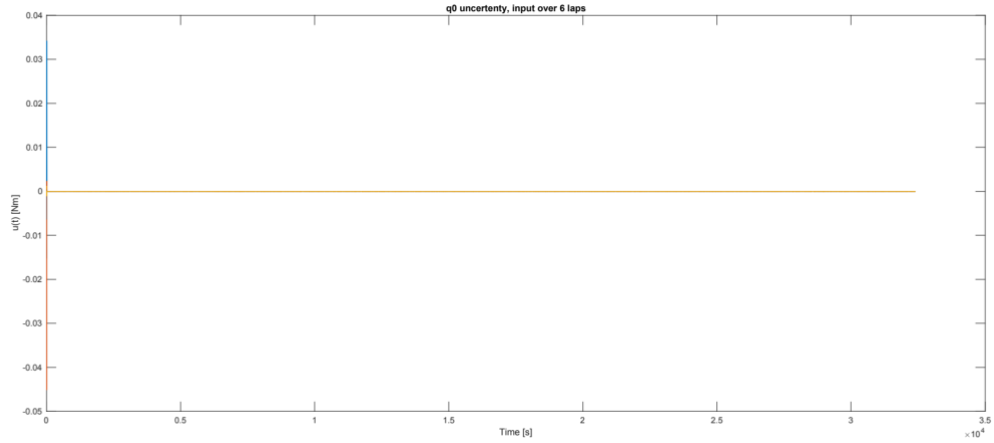


*Figure 75: $q_0$ uncertainties simulation, input u(t) plot over 6 turns.*

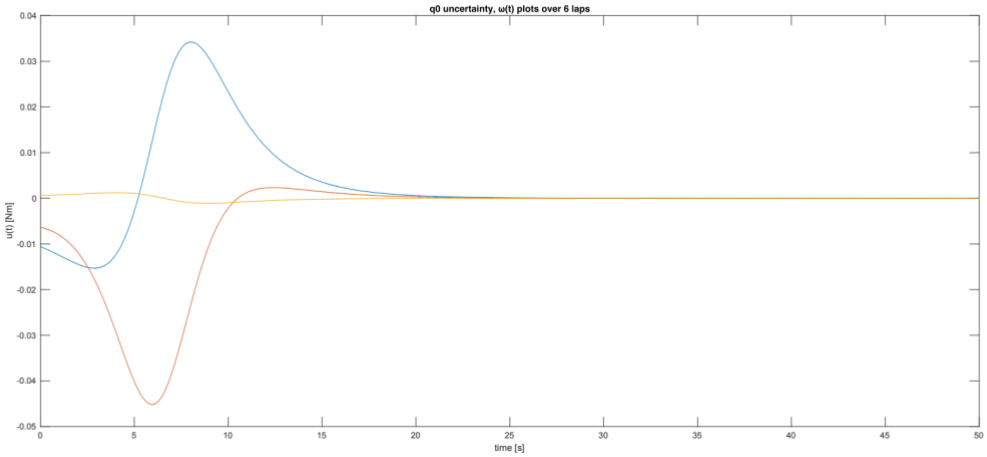


*Figure 76: $q_0$ uncertainties simulation, input u(t) close view 6 turns plot.*

Due to the uncertainty on the initial position, the quaternions behavior has changed, the undershoot on $q_2$ is lower while the overshoot on $q_4$ is higher than the one in the nominal simulation. Once in steady state the quaternions follow the reference up to the end of the 6-turn simulation, as displayed in *Figure 71*. From *Figure 76* it can be seen a strong input response within the transient, while *Figure 75* shows that in the steady state the input activities stay bounded between 9e-7 Nm and -9e-7 Nm.

*Figure 74* shows high angular velocity during the transient, since the system orientation is on track of the reference attitude, then the values decrease to reference and stay bound until the end of the simulation, as shown in *Figure 73*. No chattering is visible.

| Step 2, Initial position uncertainty simulations | Input Activities | | Pointing Error | |
|---|---|---|---|---|
| | u max | u min | APE | MPE |
| 2-turns simulation | 0,0443 Nm | 4.17e-11 Nm | 4.5% | 6.9% |
| 4-turns simulation | 0,0443 Nm | 4.8e-13 Nm | 7.4% | 8.1% |
| 6-turns simulation | 0,0443 Nm | 3.4e-13 Nm | 6% | 7.5% |

In this step, the quaternion behavior in the transient is different from the Nominal case, while during the transient the input activities and angular velocity have little higher values than in the first step with mass uncertainty. As in the previous step, all three simulations comply with the problem's requirements: the transient does not break the constraints imposed by the actuators on the torques while the attitude error in steady state respects the requirements. As for the mass uncertainty step, the performance in the steady state is almost unchanged from the nominal case.

Again, the APE and MPE are larger in the middle of the trajectory since the reference values to follow are low. The sections of the trajectory with an error larger than 1° are the beginning and the end, although they are less than 1% of the simulation time.

### 5.1.3 Initial angular velocity uncertainty

Step 3, Initial angular velocity uncertainty simulations:

- An uncertainty on the initial attitude $\omega_0$ of 0.02 rad/s is introduced.

*Angular velocity uncertainty simulation over 2 turns*

Quaternions plot:

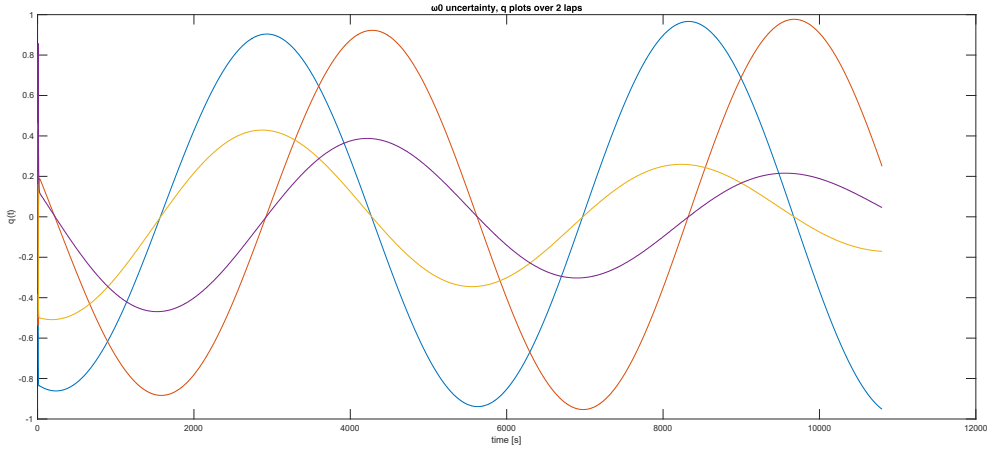


*Figure 77: $\omega_0$ uncertainties simulation, attitude quaternions plot over 2 turns period.*

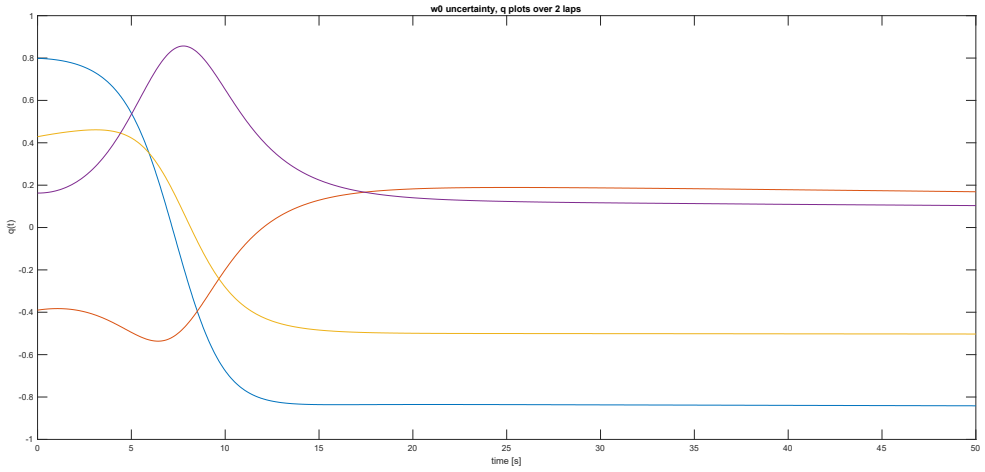


*Figure 78: $\omega_0$ uncertainties simulation, attitude quaternions close view 2 turns plot*

Angular velocity ω(t) plot:

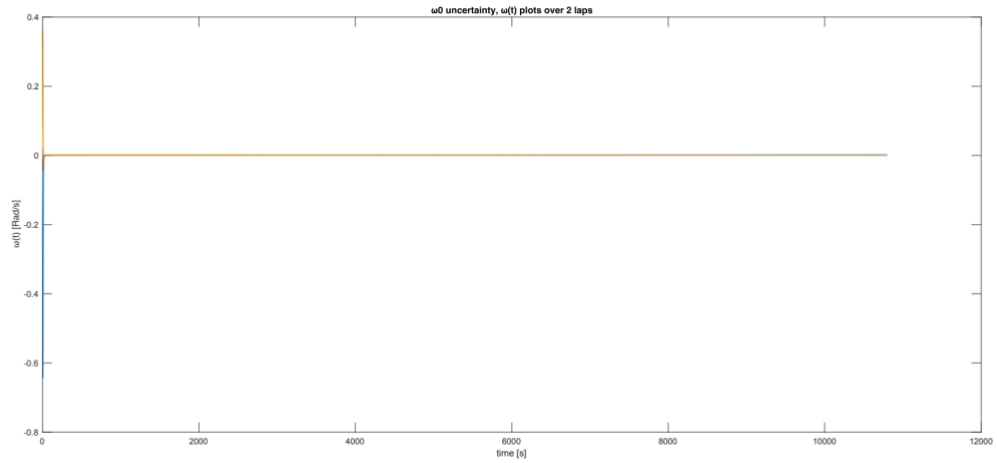


*Figure 79: $\omega_0$ uncertainties simulation, angular velocity plot over 2 turns period.*

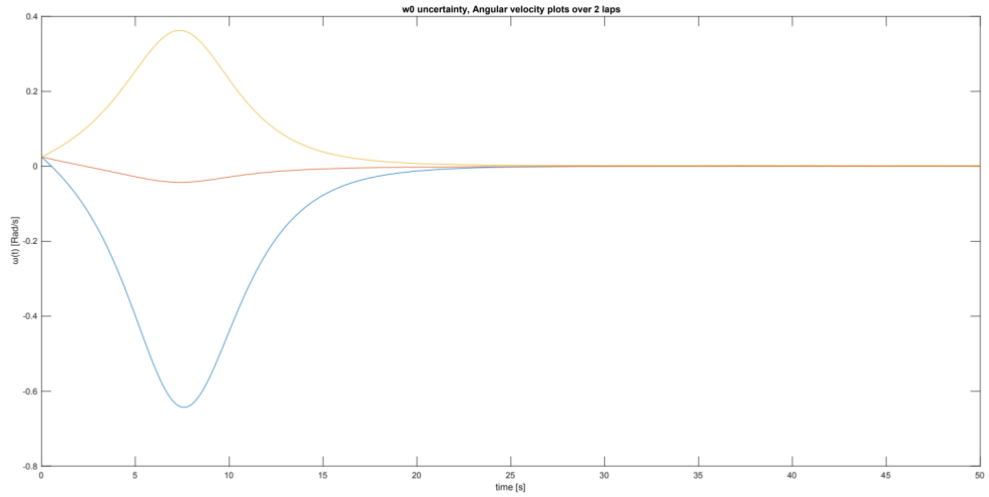


*Figure 80: $\omega_0$ uncertainties simulation, angular velocity close view 2 turns plot *

Input u plots:

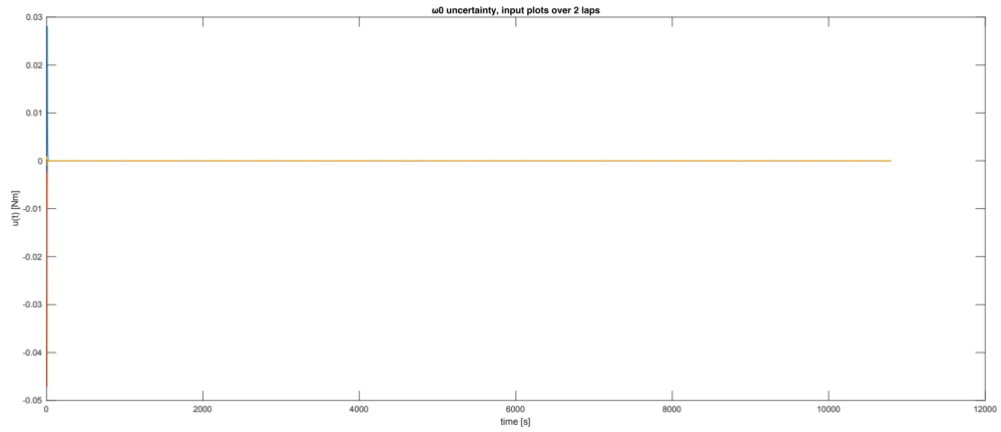


*Figure 81: $\omega_0$ uncertainties simulation, input u(t) plot over 2 turns period.*

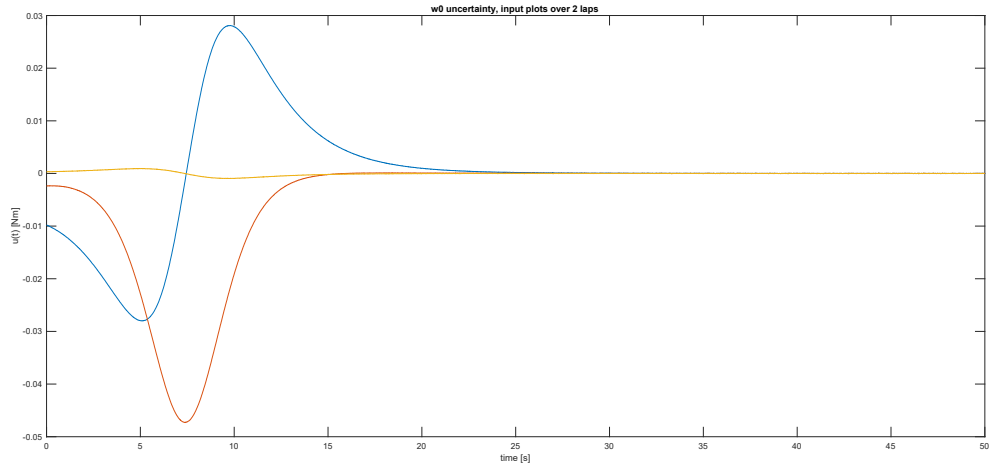


*Figure 82: $\omega_0$ uncertainties simulation, input u(t) close view 2 turns plot*

In this simulation, the quaternions behavior in the transient is again the same as the nominal case as is evident from *Figure 78.* The quaternions go to reference in less than 30 seconds with an undershoot on $q_2$ and an overshoot on $q_4$. Then the quaternions follow the reference for the rest of the 2-turn simulation, as display in *Figure 77*.

From *Figure 81* it can be seen a strong input response within the transient, while *Figure 82* shows that in the steady state the input activities stay bounded between 9e-7 Nm and -3e-7 Nm.

Due to the uncertainty introduction, the angular velocity has higher values in the transient than the nominal case, as it is shown in *Figure 80.* Then again, the values decrease to reference and stay bound until the end of the simulation, as shown in *Figure 79*. No chattering is visible.

*Angular velocity uncertainty simulation over 4 turns*

Quaternions plot:

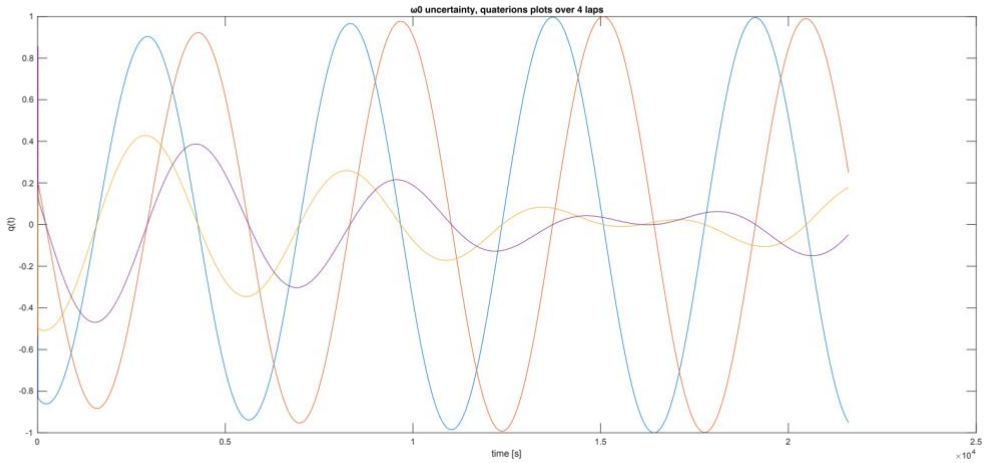


*Figure 83: $\omega_0$ uncertainties simulation, attitude quaternions plot over 4 turns period.*

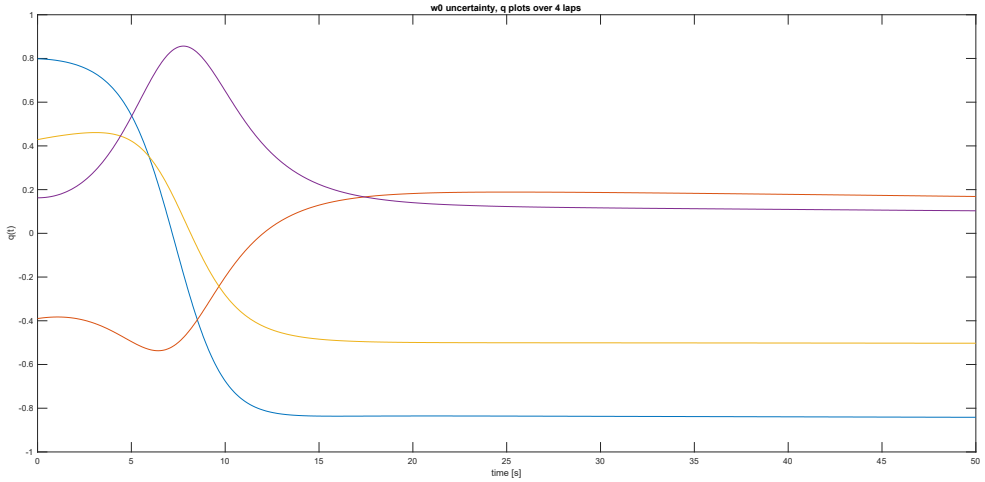


*Figure 84: $\omega_0$ uncertainties simulation, attitude quaternions close view 4 turns plot*

Angular velocity ω(t) plot:

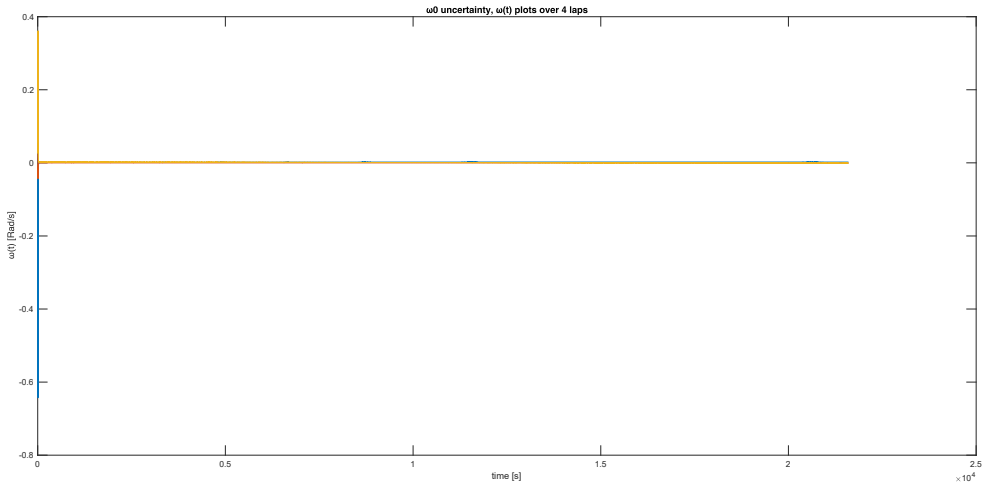


*Figure 85: $\omega_0$ uncertainties simulation, angular velocity plot over 4 turns period.*

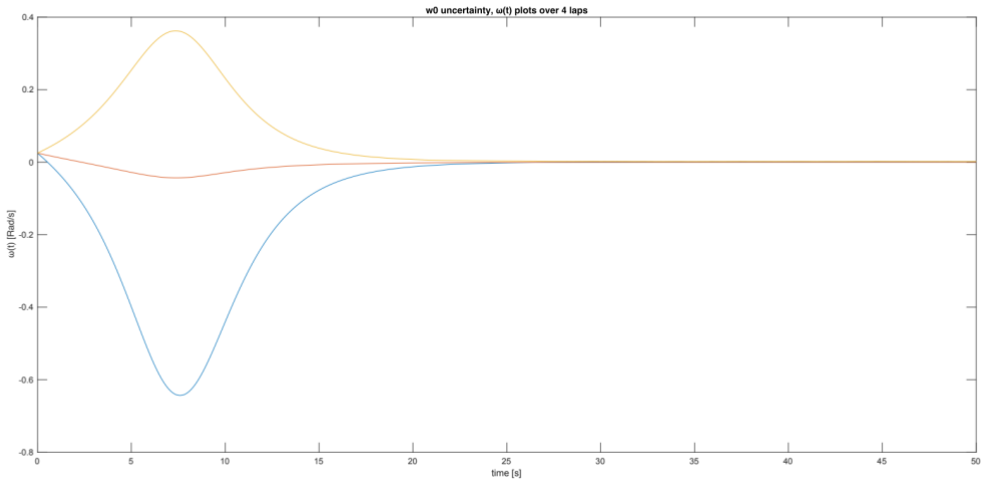


*Figure 86: $\omega_0$ uncertainties simulation, angular velocity close view 4 turns plot*

Input plots:

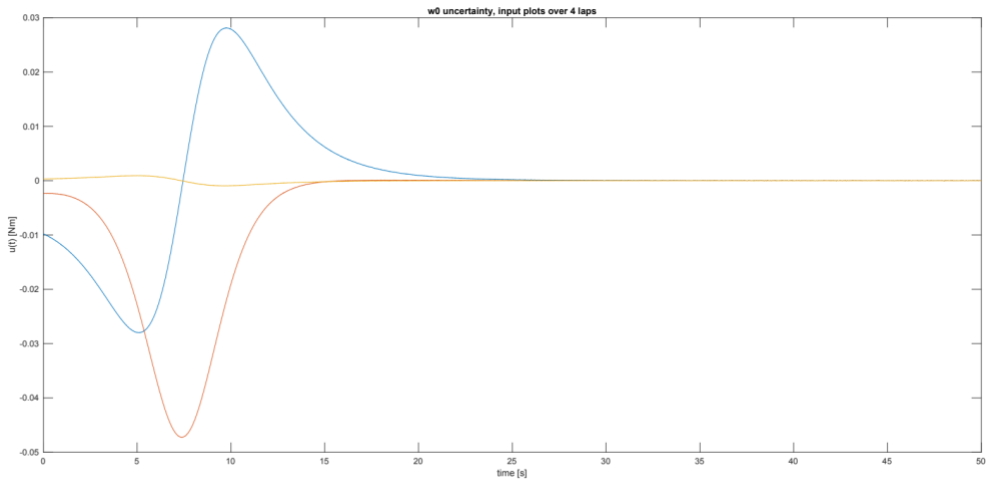


*Figure 87: All uncertainties simulation, input u(t) close view 4 turns plot*

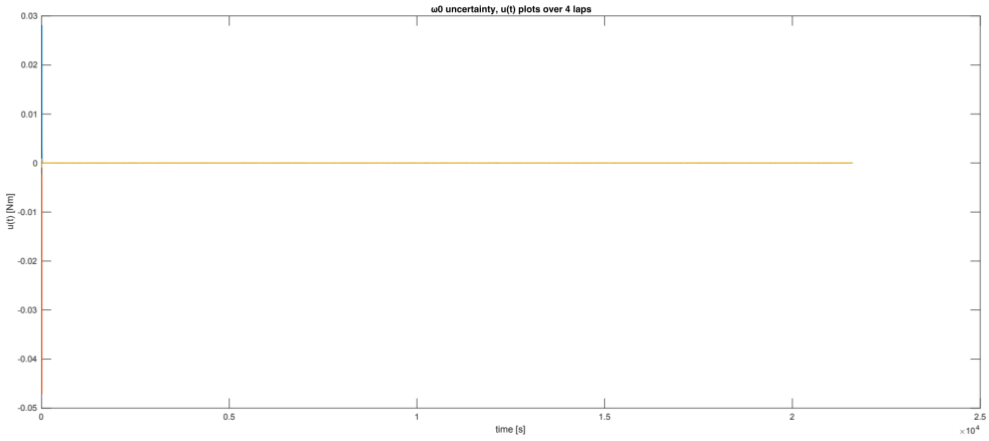


*Figure 88: $\omega_0$ uncertainties simulation, input u(t) plot over 4 turns period.*

The quaternions go to reference in less than 30 seconds and display an undershoot on $q_2$ and an overshoot on $q_4$, as is evident form *Figure 83*. Then the quaternions follow the reference for the rest of the 4-turn simulation, as display in *Figure 84*.

A strong input response within the transient can be seen in *Figure 86*, while *Figure 85* displays bounded steady state input activities with values between 9e-7 Nm and -7e-7 Nm.

As is evident in *Figure 88,* the angular velocity has large values during the transient, since the system orientation must be set on the initial reference attitude, then the values decrease to reference and stay bounded until the end of the simulation, as showed in *Figure 87*. No chattering is visible.

*Angular velocity uncertainty simulation over 6 turns*

Quaternions plot:

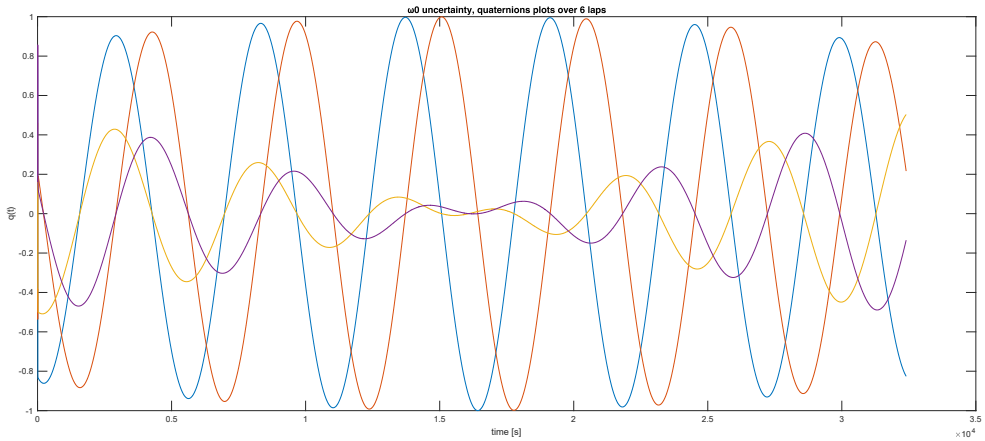


*Figure 89: $\omega_0$ uncertainties simulation, attitude quaternions plot over 6 turns period.*

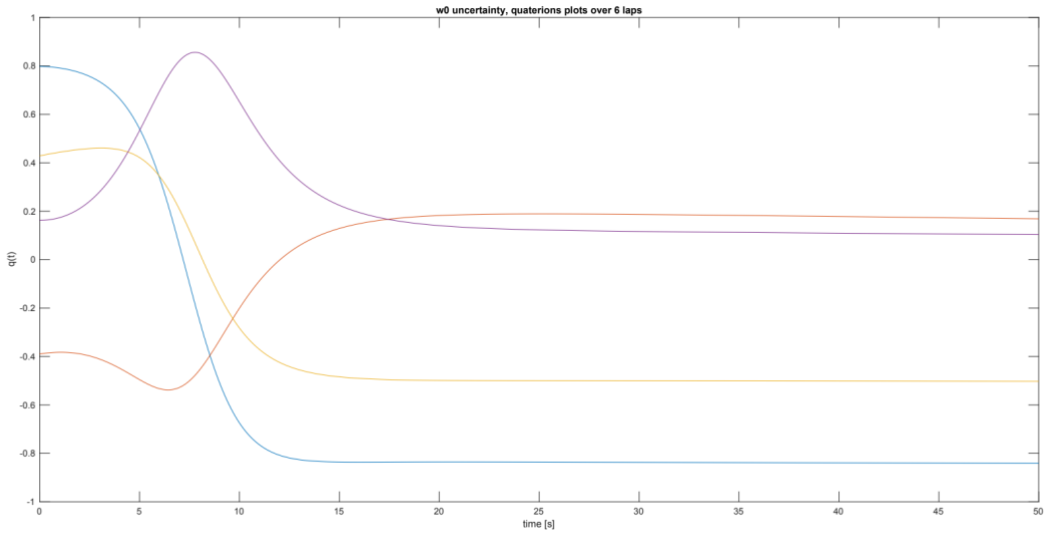


*Figure 90: $\omega_0$ uncertainties simulation, attitude quaternions close view 6 turns plot*

Angular velocity ω(t) plot:

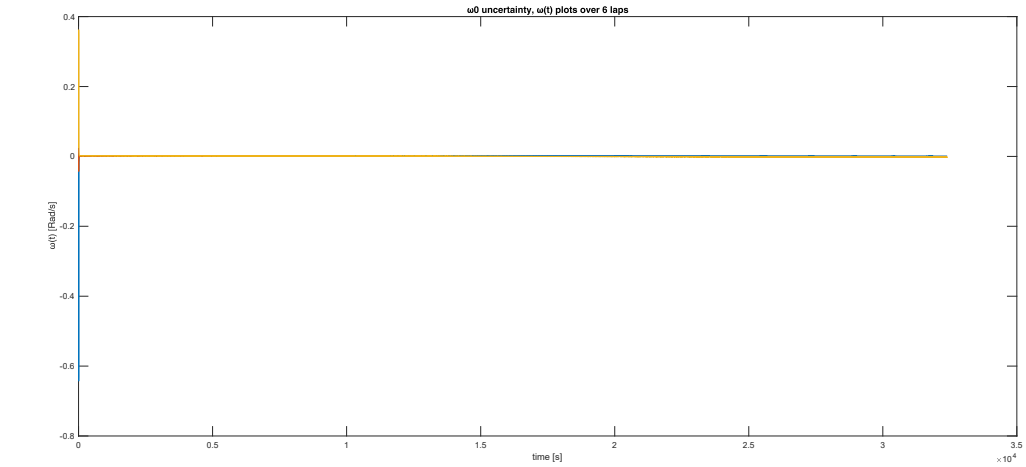


*Figure 91: $\omega_0$ uncertainties simulation, angular velocity plot over 6 turns period.*

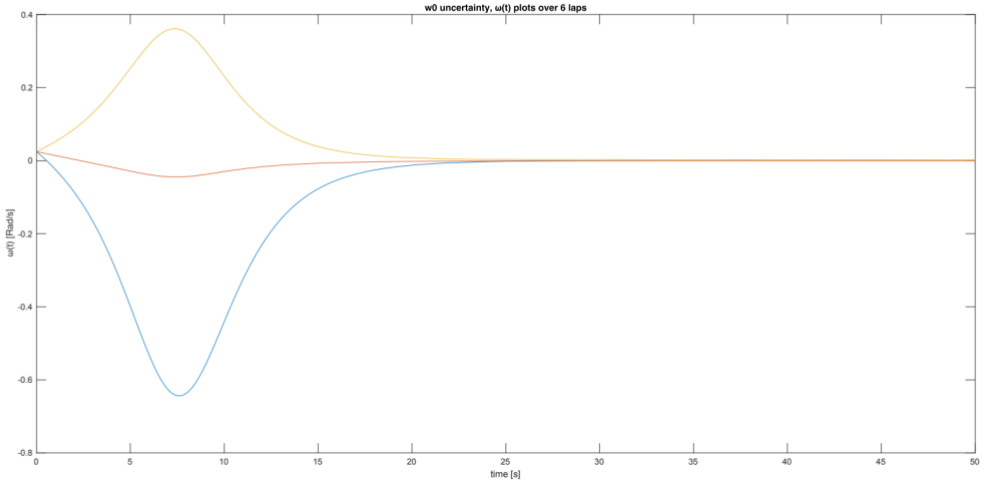


*Figure 92: $\omega_0$ uncertainties simulation, angular velocity close view 6 turns plot*

Input u plot:

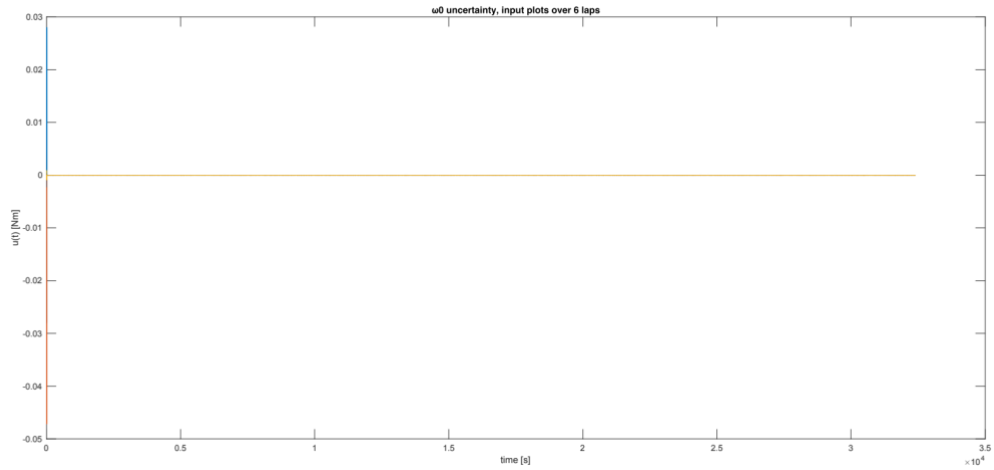


*Figure 93: $\omega_0$ uncertainties simulation, input u(t) plot over 6 turns period.*

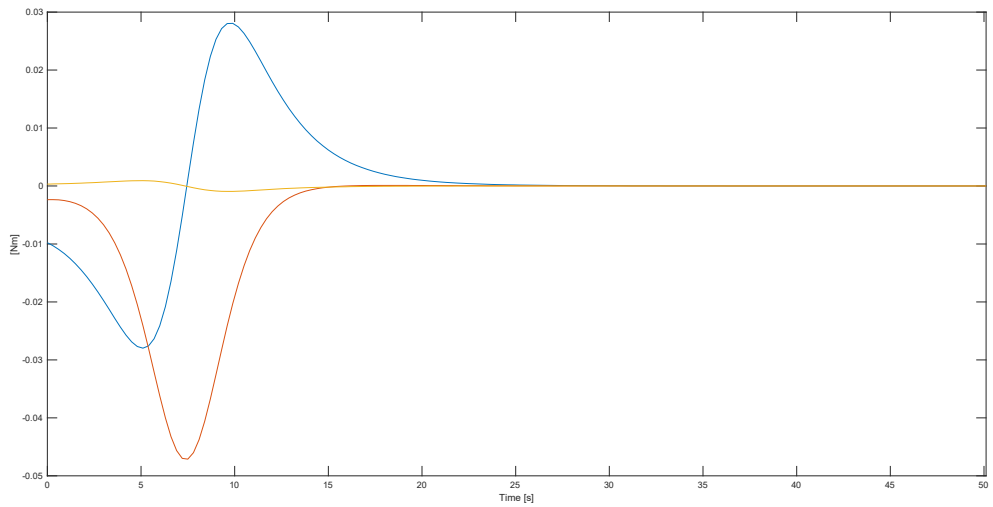


*Figure 94: $\omega_0$ uncertainties simulation, input u(t) 6-turns plot, close view.*

The quaternions go to reference in less than 30 seconds and display an undershoot on $q_2$ and an overshoot on $q_4$, as is evident form *Figure 90*. Then the quaternions follow the reference for the rest of the 6-turn simulation, as display in *Figure 89*. A strong input response within the transient can be seen

in *Figure 94*, while *Figure 93* displays bounded steady state input activities with values between 9e-7 Nm and -9e-7 Nm.

As can be seen in *Figure 92,* the angular velocity has large values during the transient, the values then decrease to reference and stay bounded until the end of the simulation, as described in *Figure 91*. No chattering is visible.

| Step 3, Initial angular velocity uncertainty simulations | Input Activities | | Pointing Error | |
|---|---|---|---|---|
| | u max | u min | APE | MPE |
| 2-turn simulation | 0.047 Nm | 4.2e-12 Nm | 4.6% | 7% |
| 4-turn simulation | 0.047 Nm | 2.52e-12 Nm | 7.3% | 8.1% |
| 6-turn simulation | 0.047 Nm | 1.82e-12 Nm | 6% | 7.5% |

In this third step the angular velocity behavior is different form the nominal case, the angular velocities on the x-axis and y-axis are higher while the z-axis is lower. Still the quaternions behavior is nearly the same of the nominal case since the controller can compensate the perturbation on the attitude slightly increasing the input activity

All three simulations comply with the problem's requirements: the transient does not break the constraints impose by the actuators while the boresight error, the APE and MPE are below the threshold values for more than 98% of the time. Like for the previous steps the performance in steady state is almost unchanged from the nominal case.

### 5.1.4 All uncertainties together:

Step 4:

- An uncertainty of **2 kg** on the mass.
- An uncertainty of **10°** is introduced on the initial attitude angles, which is converted in quaternion representation and apply to the attitude quaternion.
- An uncertainty on the initial $\omega_0$ of **0.02 rad/s** is introduced.

*All uncertainties simulation over 2 turns:*

Quaternions plots

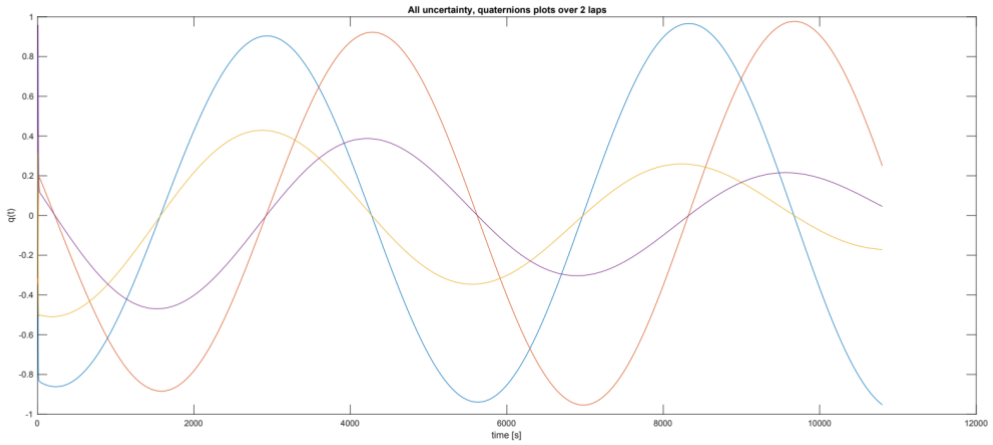


*Figure 95: All uncertainties simulation, attitude quaternions plot over 2 turns period.*

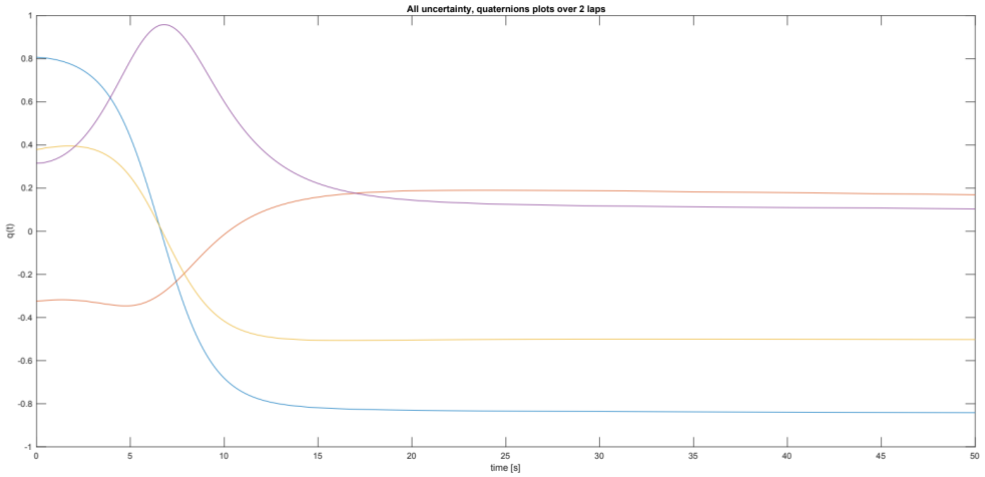


*Figure 96: All uncertainties simulation, attitude quaternions close view 2 turns plot*

Angular velocity ω(t) plot:

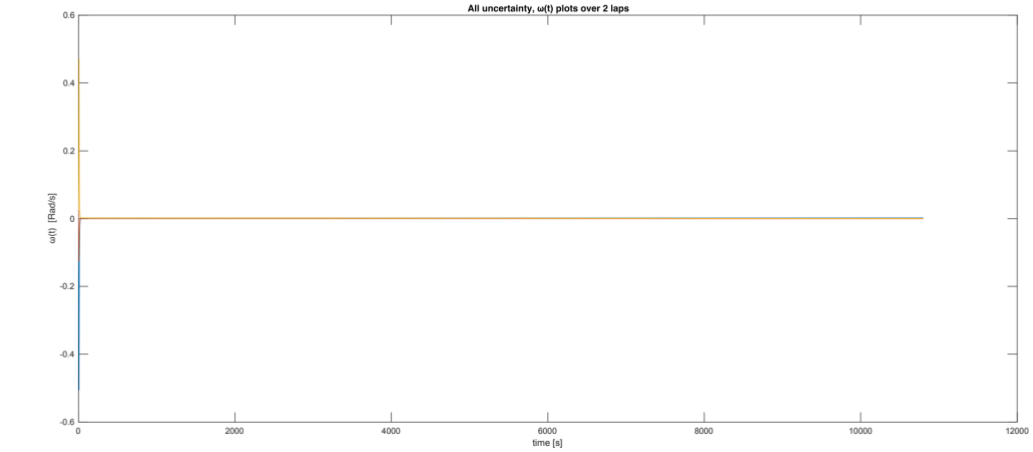


*Figure 97: All uncertainties simulation, angular velocity plot over 2 turns period.*

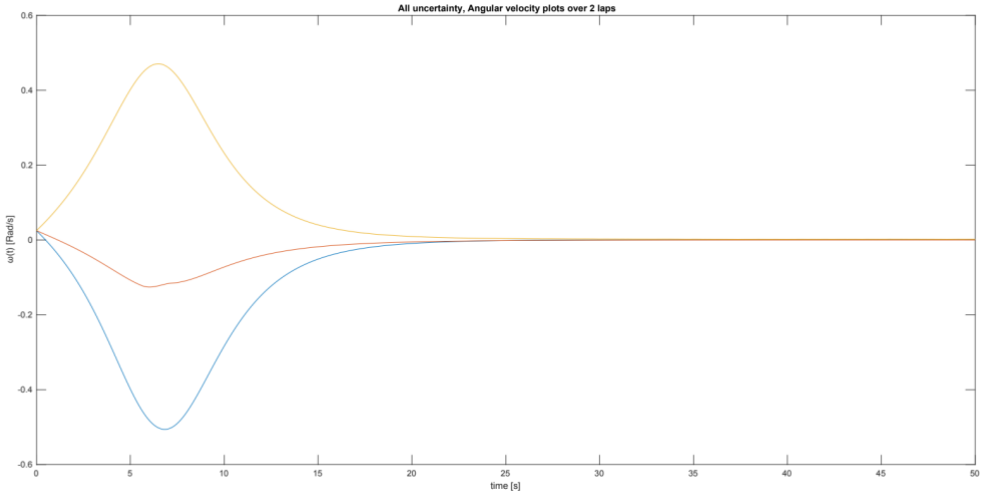


*Figure 98: All uncertainties simulation, angular velocity close view 2 turns plot*

Input u plot:

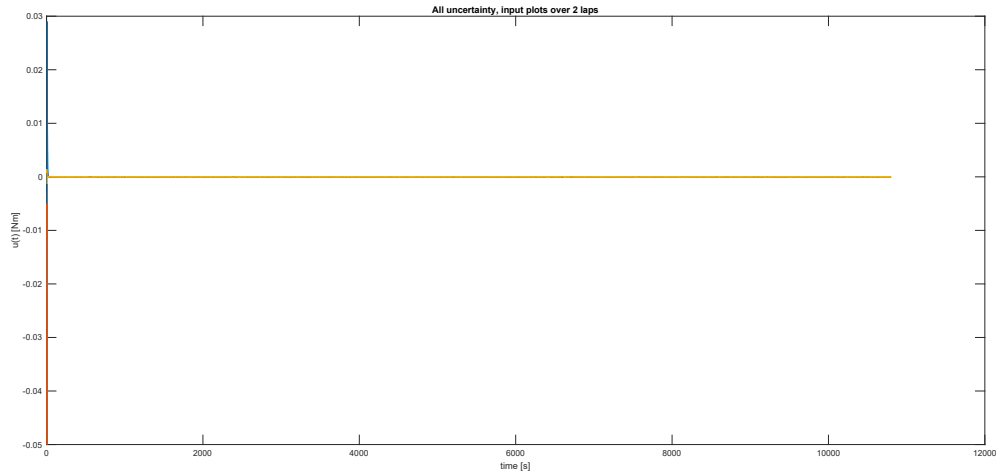


*Figure 99: All uncertainties simulation, input u(t) plot over 2 turns period.*

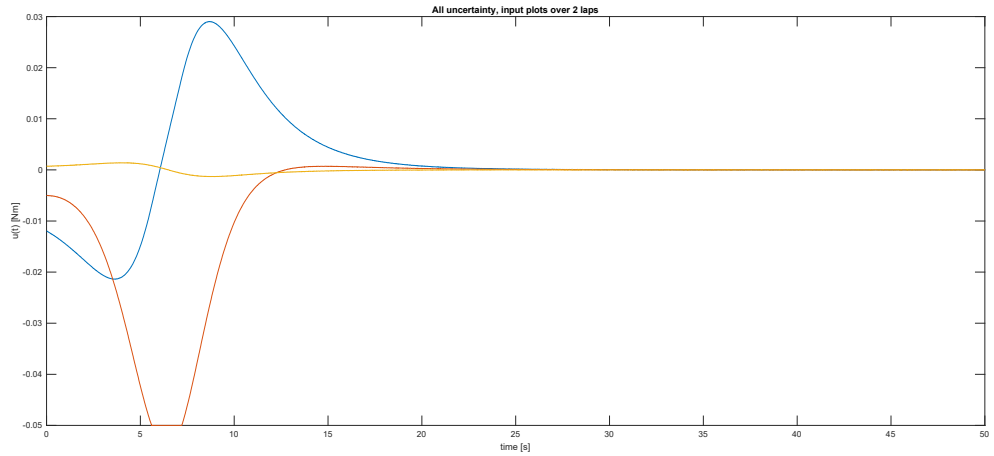


*Figure 100: All uncertainties simulation, input u(t) close view 2 turns plot*

As is obvious from *Figure 96* that the controls rapidly lead the quaternions to reference and keep them until the end of the 2-turn simulation. The quaternions an undershoot on $q_2$ and an overshoot on $q_4$ without any post-transition oscillatory effect, as display in *Figure 95*. Then the quaternions follow the reference. *Figure 100* shows a strong input response within the transient, while *Figure 99* shows that in the steady state the input activities is bounded between 9e-7 Nm and -9e-7 Nm.

The angular velocity has a peak during the transient in order to reach the reference attitude, then the values decrease to reference and stay bounded until the end of the simulation, as showed in *Figure 97* and *Figure 98*. No chattering is visible.

*All uncertainties simulation over 4 turns:*

Quaternions plot:

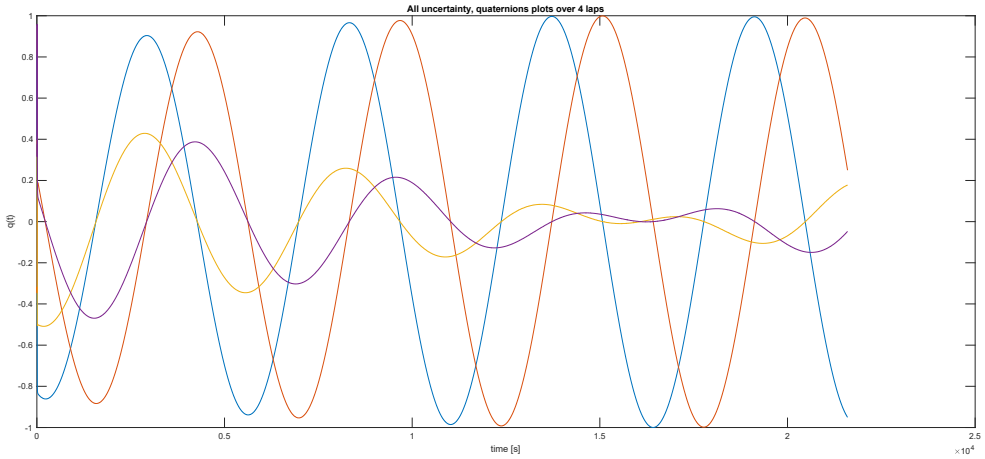


*Figure 101: All uncertainties simulation, attitude quaternions plot over 4 turns period.*

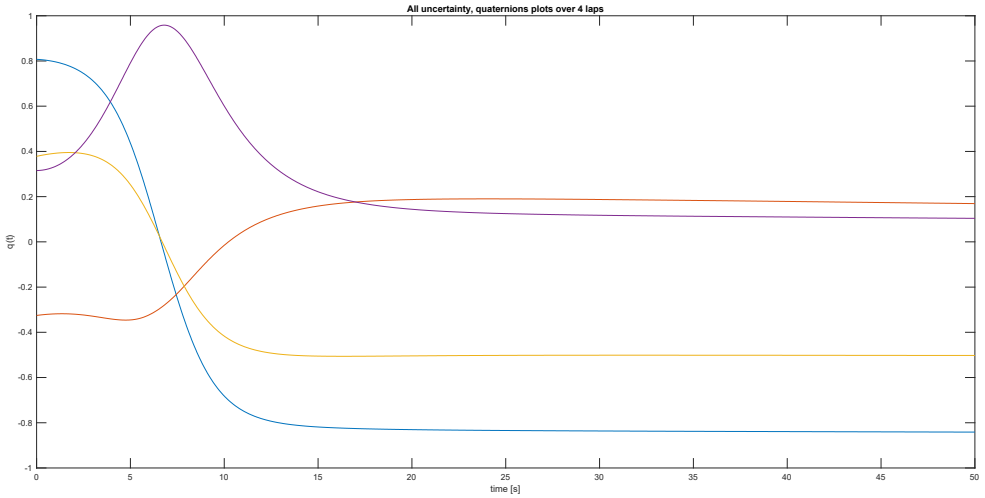


*Figure 102: All uncertainties simulation, attitude quaternions close view 4 turns plot*

Angular velocity ω(t) plot:

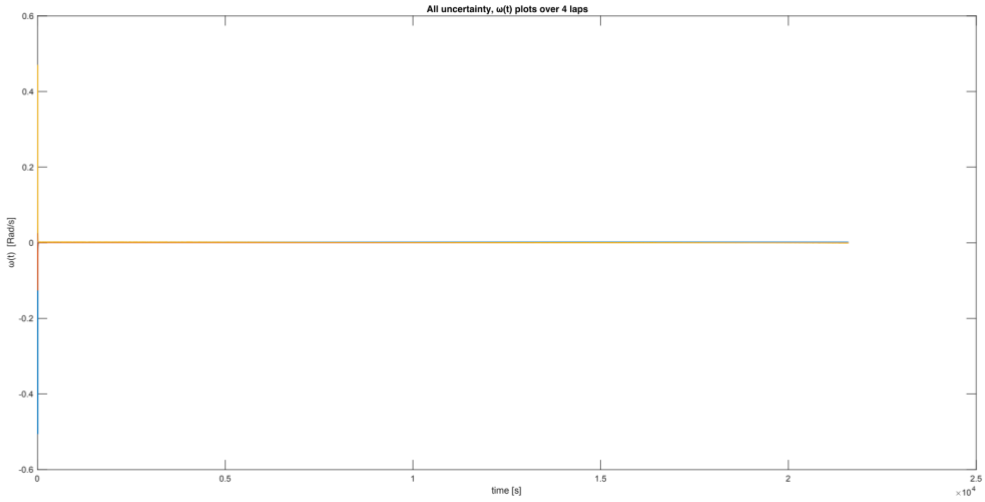


*Figure 103: All uncertainties simulation, angular velocity plot over 4 turns period.*

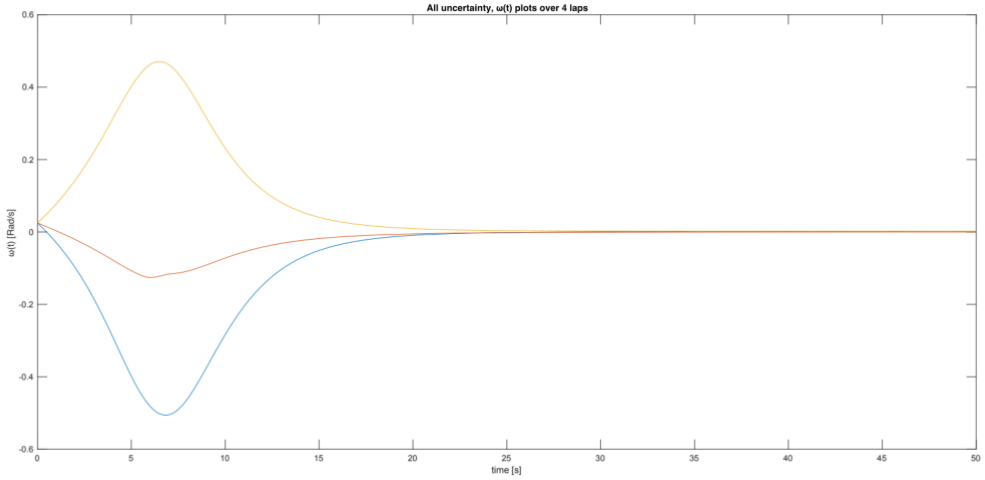


*Figure 104: All uncertainties simulation, angular velocity close view 4 turns plot*

Input u plot:

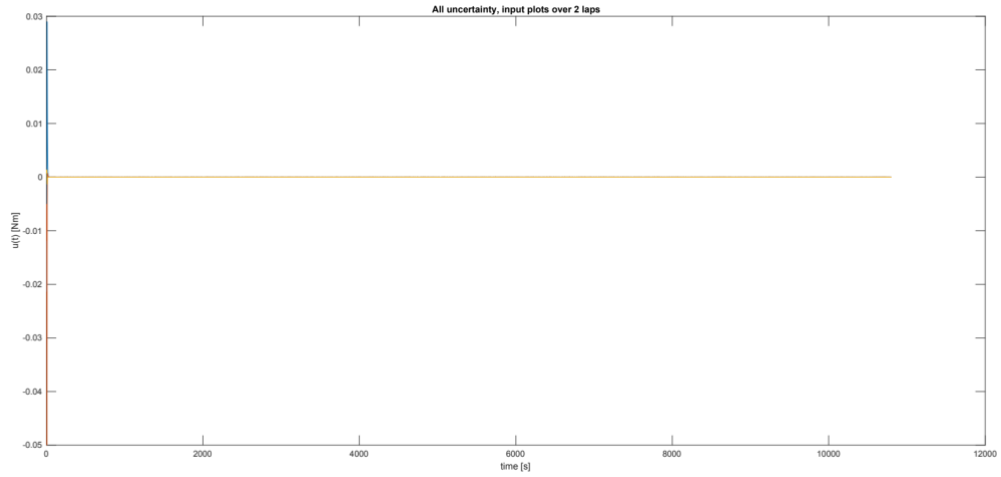


*Figure 105: All uncertainties simulation, input u(t) plot over 4 turns period.*

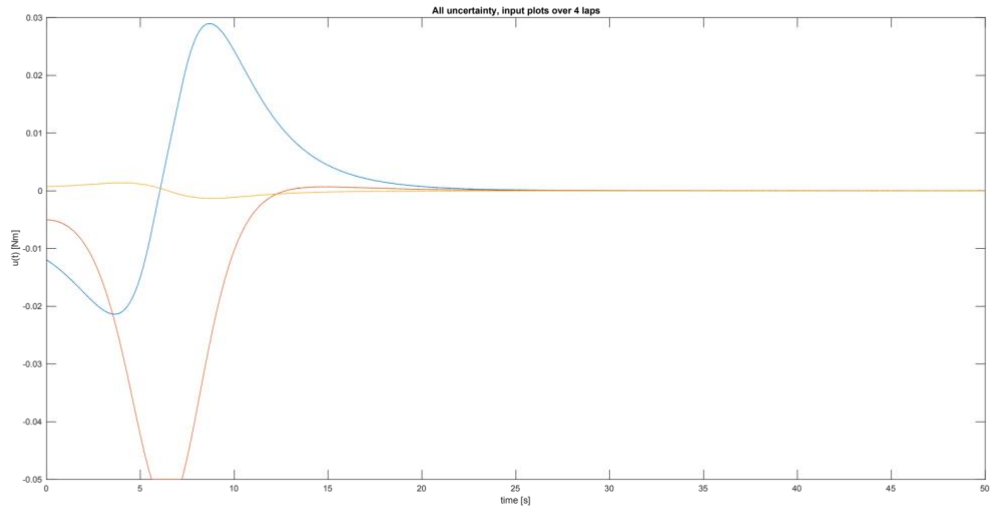


*Figure 106: All uncertainties simulation, input u(t) close view 4 turns plot*

As is obvious from *Figure 102* the controls rapidly lead the quaternions to reference and keep them until the end of the 4-turn simulation. The quaternions an undershoot on $q_2$ and an overshoot on $q_4$ without any post-transition oscillatory effect, as displayed in *Figure 101*. Then the quaternions follow the reference. *Figure 106* shows a strong input response within the transient, while *105 100* shows that in the steady state the input activities are bounded between 9e-7 Nm and -7e-7 Nm.

The angular velocity has a peak during the transient in order to reach the reference attitude, then the values decrease to reference and stay bound until the end of the simulation, as shown in *Figure 103* and *Figure 104*. No chattering is visible.

*All uncertainties simulation over 6 turns:*

Quaternions plot:

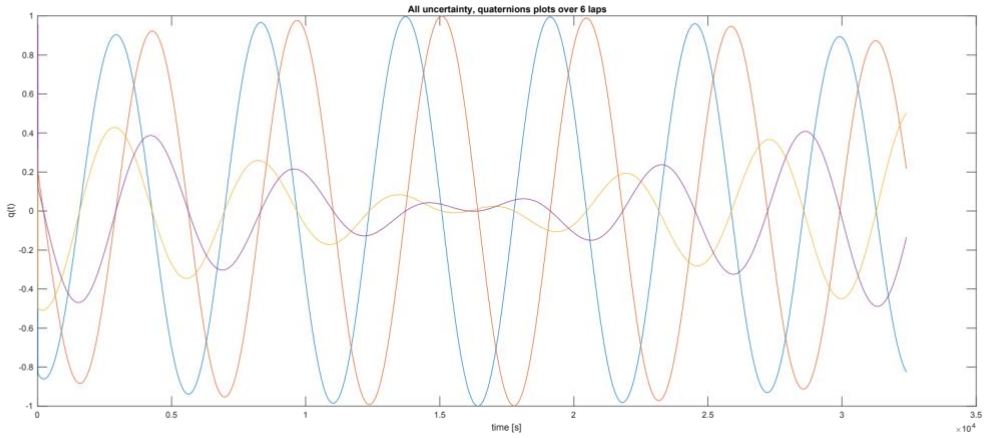


*Figure 107: All uncertainties simulation, attitude quaternions plot over 6 turns period.*

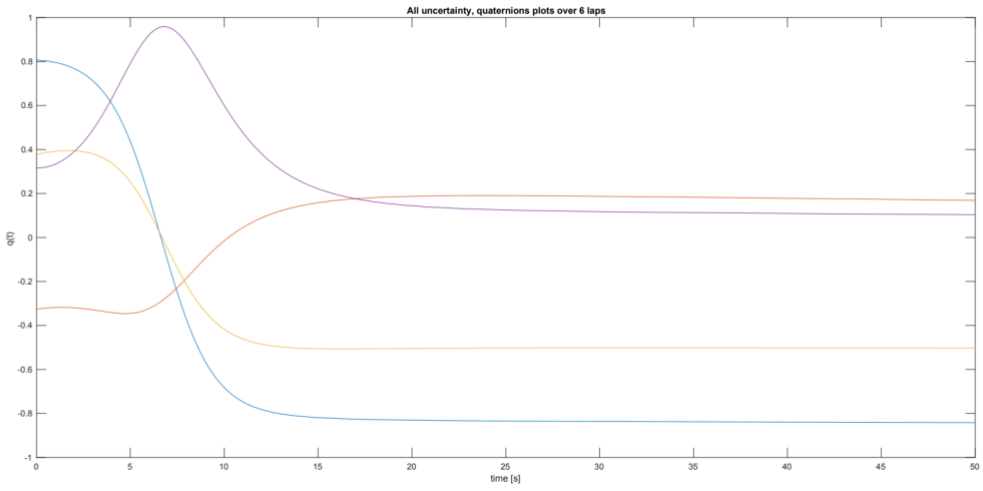


*Figure 108: All uncertainties simulation, attitude quaternions close view 6 turns plot*

Angular velocity ω(t) plot:

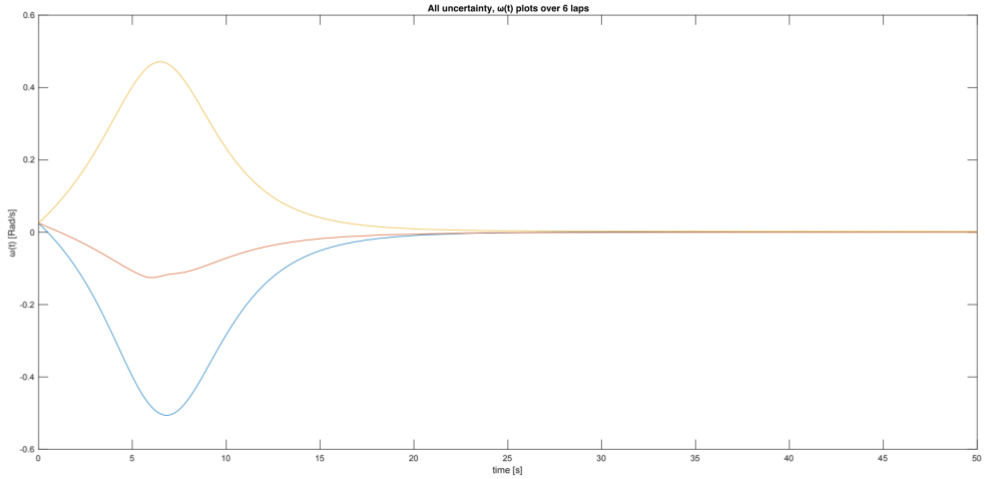


*Figure 109: All uncertainties simulation, angular velocity close view 6 turns plot*

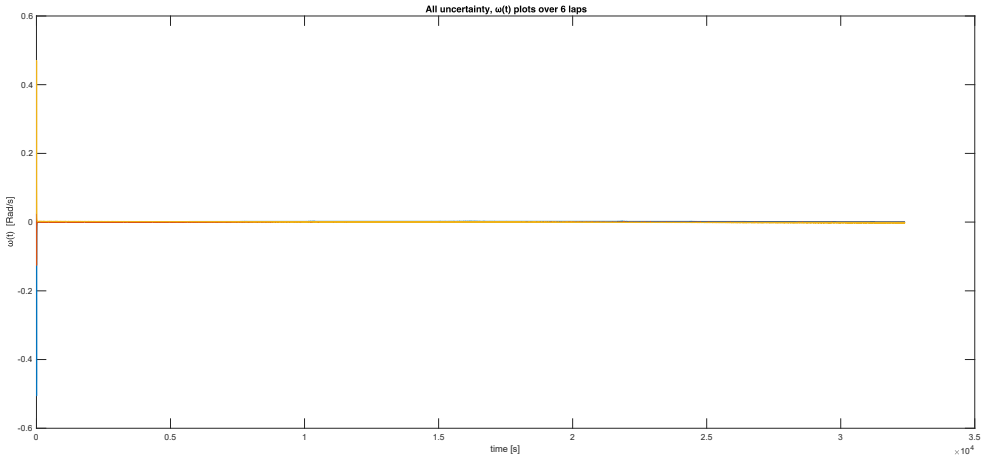


*Figure 110: All uncertainties simulation, angular velocity plot over 6 turns period.*

Input u plot:

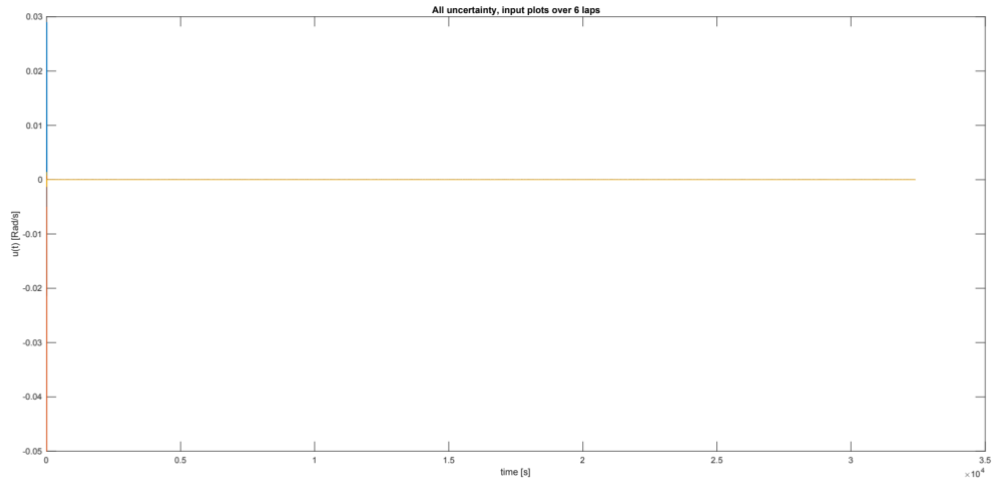


*Figure 111: All uncertainties simulation, input u(t) plot over 6 turns period.*

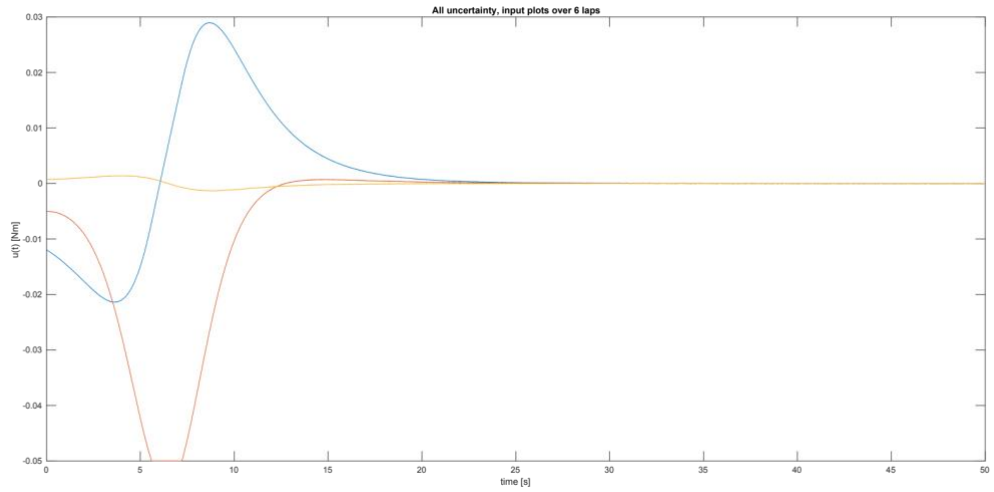


*Figure 112: All uncertainties simulation, input u(t) close view 2 turns plot*

It is easy to see from *Figure 108* that the controls rapidly lead the quaternions to reference and keep them until the end of the simulation. The quaternions an undershoot on $q_2$ and an overshoot on $q_4$ without any post-transition oscillatory effect, as displayed in *Figure 107*. Stabilization is achieved within a short time.

*Figure 112* shows a strong input response within the transient, while *Figure 111* shows that in the steady state the input activities are bounded between 9e-7 Nm and -3e-7 Nm.

The angular velocity has a peak during the transient in order to reach the reference attitude, then the values decrease to reference and stay bound until the end of the simulation, as shown in *Figure 109* and *Figure 110*.

| Step 4, All uncertainties simulations | Input Activities | | Pointing Error | |
|---|---|---|---|---|
| | u max | u min | APE | MPE |
| 2 turn simulation | 0.05 Nm | 7.1e-11 Nm | 4.6% | 7% |
| 4 turn simulation | 0.05 Nm | 3.3e-12 Nm | 7.5% | 8.2% |
| 6 turn simulation | 0.05 Nm | 2.9e-12 Nm | 6,1% | 7.5% |

In this last step, the input response to neglect the uncertainties required by the sliding mode controller leads the torque about the y-axis to saturation to the lower bound for 2 seconds. This is the only case where the control input reaches saturation, so it is also the case where the system gets more exited. Nevertheless, the controls rapidly lead the quaternions to reference without any post-transition oscillatory effect.

The simulations follow the problem requirements: the transient does not break the constraints imposed by the actuators while the boresight error, the APE and MPE are below the threshold values for more than 98% of the time.

As can be seen from the table above, the performance is almost unchanged from the nominal simulations even if mass uncertainty was introduced. Since both the attitude reference and the angular velocity reference are small the APE and MPE are larger in the middle of the trajectory although the center of the trajectory is where the error on the orientation is lower. The only sections with attitude error larger the 1° are the beginning and the end of the trajectory, although for less than 1% of the simulations time.

*Worst-case analysis conclusions*

As can be noted the sliding mode controller is able to automatically neglect the uncertainties introduced in the main system parameters of the simulations, with a small cost on the input activities. In order to see a clear effect of the uncertainties within the transient, the uncertainty magnitude must be significantly increased.

The performance of the error during the trajectory can be related to the reference values since the lower the values the higher the pointing error APE and MPE.
The pointing error instead has higher values at the beginning and the end of the trajectory mainly due to the higher values of the eternal disturbances and the reference velocity.

## 5.2 Montecarlo campaign

The Monte Carlo (MC) simulation combines the accuracy of statistical analysis with the rigor of the scientific approach. It is therefore a suitable tool for examining the control strategy of perturbed nonlinear systems. This technique makes it simpler to estimate the impact of risk and gives more insight when under uncertain initial conditions. This is achievable because the method treats the variables and their uncertainty to produce a comprehensive description of every possible outcome. So, Monte Carlo simulation is a method for evaluating how a model reacts to uncertainty by using random inputs [24]. Usually, there are three steps involved:

- Randomly generate N sets of initial conditions.
- Simulate each set of initial conditions on the model of the system being analyzed.
- Compile and evaluate the simulations' results.

In this case, the parameters used are the system's state variables **q**, **ω** and m. The total number of sets of initial conditions simulated is 56.

Again, all simulations have nominal initial conditions:

- $\omega_0$ = [0.05; 0.05; 0.05]
- $q_0$ = [ 0.7985; -0.3899; 0.4287; 0.1626].

The initial conditions for the 56 simulations are characterized by:

- a random uncertainty evenly distributed of amplitude ranging from **-2 kg** to **2 kg** on the mass;
- a random uncertainty evenly distributed of amplitude ranging from **-0.02 rad/s** to **0.02 rad/s** on the initial angular velocity;
- a random uncertainty evenly distributed of amplitude ranging from **-10°** to **10°** on the initial attitude angles, which is converted into quaternion representation and applied to the initial attitude quaternion.

The ranges of these uncertain values define an area in the parameter space over which the control behavior is investigated.

Quaternions plot:

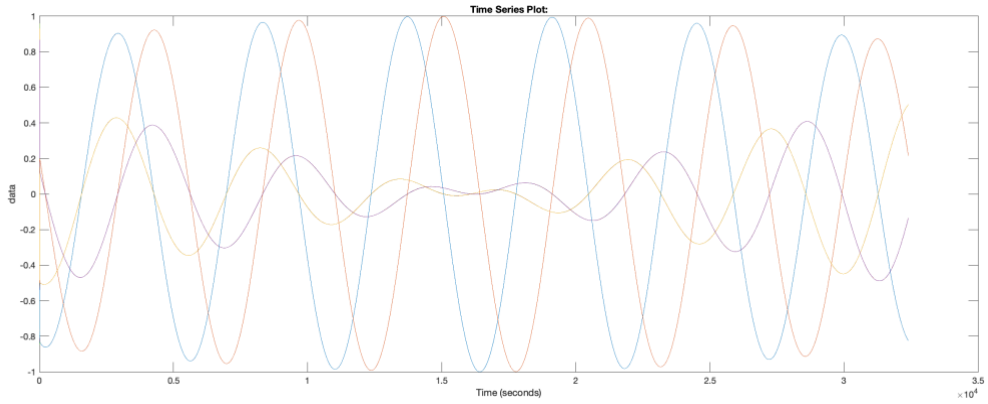


*Figure 113: Quaternions plot, Montecarlo simulation.*

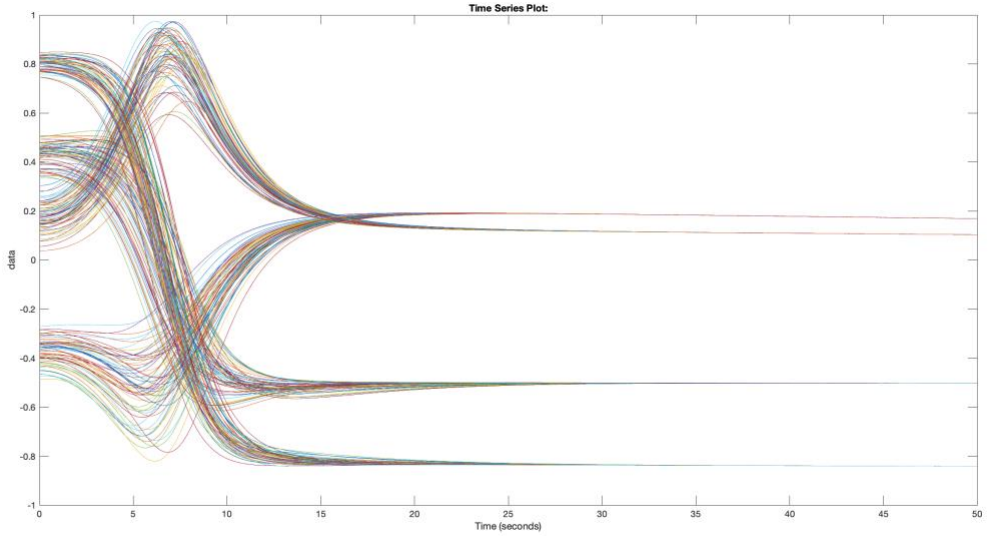


*Figure 114: Quaternions plot, Montecarlo simulation, transient.*

Angular velocity plot:

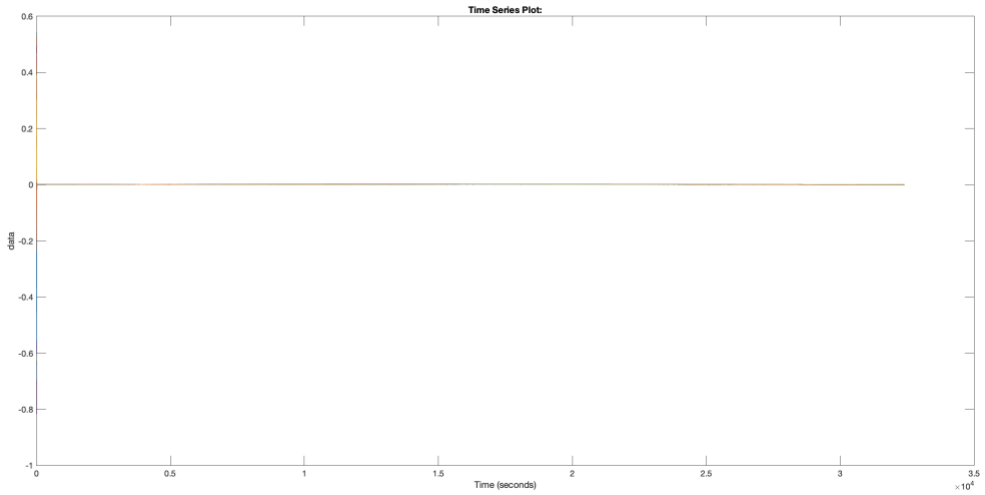


*Figure 115: Angular velocities plot, Montecarlo simulation.*

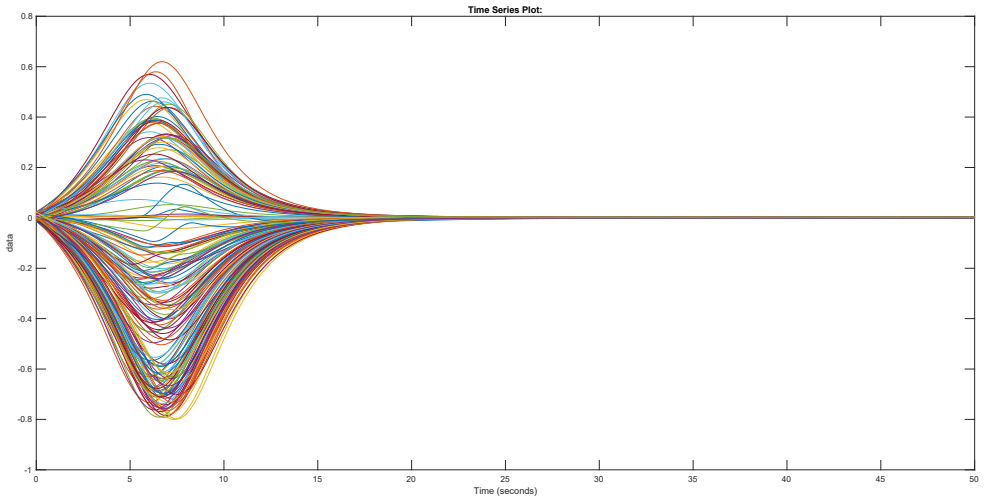


*Figure 116: Angular velocities plot, Montecarlo simulation, transient.*

As expected from the results of the worst-case analysis, the success rate of the Montecarlo campaign is 100%, every simulation respects the input activities' constraints on the transient and keeps the error bounded in a steady state, as illustrated in *Figure 114* and *Figure 116*. The transients of both quaternions and angular velocity never exceed 30 seconds, before rapidly decreasing to reference without any post-transition oscillatory effect.

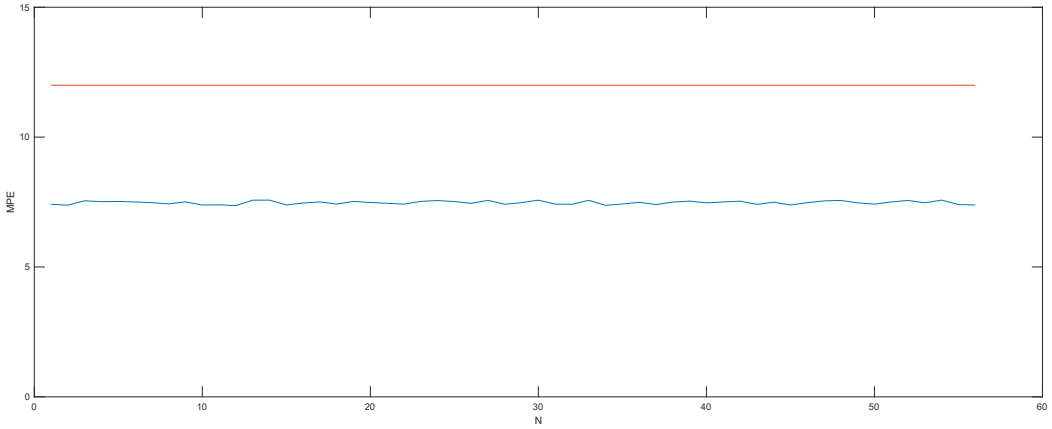


*Figure 117: MPE values of the 56 Montecarlo simulations (blue line) compared with the threshold values (red line)*

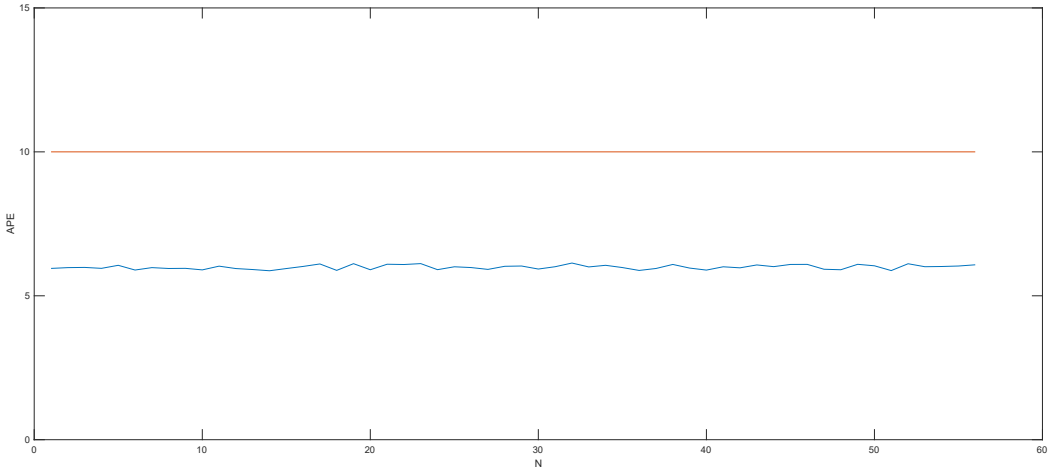


*Figure 118: APE values of the 56 Montecarlo simulations (blue line) compared with the threshold values (red line)*

As shown in *Figure 117* and *Figure 118* all the Montecarlo simulations have the APE and MPE below the given threshold and the attitude error is below 1.2° for more than 98% of the simulation time. The designed solution is therefore capable to handle the model uncertainties while performing the given task.

# 6. Conclusion

An overview of the setting for the proposed inspection task is followed by the design and illustration of a generic approach to effectively complete the inspection. The approach outlines how to create a suitable reference attitude trajectory for the observer satellite to act as a reference in a tracking control problem. After this preparatory phase, the 12U CubeSat plant is modeled using Euler's equation of rotation to account for quaternion kinematics and spacecraft dynamics.

Then, a more realistic model is devised adding the effect of the external disturbances and the limitation of the actuation system derived from commonly used reaction wheels.

After the definition of the plant, a Sliding Mode Control strategy is designed for the 12U CubeSat caring out the operation. The chosen SMC is then tuned to optimize the performance using a trial-and-error procedure using the increasingly complex model defined in Chapter 3.

Concluded the tuning, the effectiveness of the final control strategy is proven.

In the next part, worst-case assessments and Montecarlo simulations are done in various scenarios by adding uncertainty to the initial conditions of the main parameters involved in the problem formulation. This procedure is established for the purpose of robustness analysis to take into account the most frequent sources of faults, in the application under investigation. In this uncertainty-based scenario, the proposed control strategy performs very effectively, with a success rate of 100% for each simulation run and a behavior close to the one in nominal settings. The proposed objectives of this thesis have been reached, and a method to execute the inspection is derived along with a convenient attitude controller.

For future work, a suitable reaction wheels system, or another actuation system, must be modeled and added to the already existing attitude control model, to test the controller behavior in a real scenario. Moreover, the attitude controller should be combined with a position controller in a single control scheme to find out any unmodeled behaviors. The two controllers may easily interfere with each other, leading to a decrease in performance and robustness.

References:

[1] https://brycetech.com/reports

[2] First CubeSats Aboard for Artemis I Mission, https://blogs.nasa.gov/artemis/2021/07/20/first-cubesats-aboard-for-artemis-i-mission/

[3] Kar-Keung D Young. “Controller design for a manipulator using theory of variable structure systems”. In: IEEE Transactions on Systems, Man, and Cybernetics 8.2 (1978), pp. 101-109

[4] Okyay Kaynak, Fumio Harashima, and Hideki Hashimoto. “Variable structure systems theory applied to sub-time optimal position control with an invariant trajectory”. In: The transactions of the Institute of Electrical Engineers of Japan. B 104.9 (1984), pp. 610–614.

[5] Vision-Based CubeSat Closed-Loop Formation Control in Close Proximities, F. Fahimi, De Gruyter, 2019.

[6] Chutiphon Pukdeboon, Alan SI Zinober, and May-Win L Thein. “Quasi-continuous higher order sliding-mode controllers for spacecraft-attitude-tracking maneuvers”. In: IEEE Trans- actions on Industrial Electronics 57.4 (2009), pp. 1436–1444

[7] Nonlinear Control and Aerospace Application, Lecture notes, C. Novara.

[8] ECSS paper ECSS-E-ST-60-10.

[9] E. Canuto, C. Novara, L. Massotti, C. Perez Montenegro and D. Carlucci, Spacecraft dynamics and control. The embedded model control approach, Butterworth-Heinemann (Elsevier), pp. 39 to 44

[10] E. Canuto, C. Novara, L. Massotti, C. Perez Montenegro and D. Carlucci, Spacecraft dynamics and control. The embedded model control approach, Butterworth-Heinemann (Elsevier) p 31-32

[11] Spacecraft Dynamics and Control: A Practical Engineering Approach (Marcel J. Sidi) pp. 88-89

[12] Advanced Dynamics Rigid Body, Multibody, and Aerospace Applications (Reza N. Jazar)

[13] Fundamentals of Spacecraft Attitude Determination and Control (F. Landis Markley, John L. Crassidis (auth.)) chapter 2-3

[14] Spacecraft dynamics and control the embedded model control approach (Canuto, Enrico Carlucci, Donato Massotti etc.) chapter 2

[15] Applied Nonlinear Control (Jean-Jacques Slotine, Weiping Li)

[16] Robust Adaptive Dynamic Programming and Feedback Stabilization of Nonlinear Systems, Yu Jiang, Zhong-Ping Jiang, January 2014, Engineering, Mathematics, IEEE Transactions on Neural Networks and Learning Systems

[17] Sliding Mode Control for a Class of Nonlinear Multi-agent System With Time Delay and Uncertainties, Jie Zhang, Ming Lyu, Tianfeng Shen, Lei Liu, Y. Bo, 2018, Mathematics, IEEE Transactions on Industrial Electronics

[18] Sliding Mode Control Theory and Applications (Christopher Edwards, Sarah K. Spurgeon), chapter 3

[19] Monte Carlo approach to the analysis of UAVs control system, Ou Chaojie, J. Ju, Wang Hongxin, Zhen Ziyang, 2014, IEEE Chinese Guidance, Navigation and Control Conference

[20] Robustness of a nonlinear missile autopilot designed using dynamic inversion, M. McFarland, S. M. Hoque, 2000, Engineering

[21] Drag-Modulation Flight-Control System Options for Planetary Aerocapture, Z. Putnam, R. Braun, 2014, Physics, Engineering, Journal of Spacecraft and Rockets

[22] Sliding mode control for systems subjected to unmatched disturbances/unknown control direction and its application, Zongyi Guo, Jianguo Guo, 2020, Engineering, International Journal of Robust and Nonlinear Control

[23] Overview of CubeSat Technology, Richard P. Welle, 2020

[24] The Monte Carlo Simulation Method for System Reliability and Risk Analysis, Enrico Zio, chapter 1.

[25] Introduction to the Small Satellite Revolution and Its Many Implications, Joseph N. Pelton and Scott Madry

[26] Overview of CubeSat Technology, Richard P. Welle

[27] Spacecraft dynamics and control the embedded model control approach (Canuto, Enrico Carlucci, Donato Massotti etc.) chapter 6

[28] https://space.skyrocket.de/index.html

[29] Fundamentals of Spacecraft Attitude Determination and Control (F. Landis Markley, John L. Crassidis (auth.)) chapter 7

[30] https://www.nasa.gov/content/what-are-smallsats-and-cubesats

[31] https://space.skyrocket.de/doc_sdat/prox-1.htm